Sanna Haavisto

Application of Doppler Optical Coherence Tomography in Velocity Profiling Rheometry of Complex Fluids

Esitetään Jyväskylän yliopiston matemaattis-luonnontieteellisen tiedekunnan suostumuksella
julkisesti tarkastettavaksi yliopiston Ylistönrinteen salissa FYS1
elokuun 9. päivänä 2019 kello 12.

Academic dissertation to be publicly discussed, by permission of
the Faculty of Mathematics and Science of the University of Jyväskylä,
in Ylistönrinne, auditorium FYS1, on August 9, 2019 at 12 o'clock noon.

JYVÄSKYLÄN YLIOPISTO
UNIVERSITY OF JYVÄSKYLÄ

JYVÄSKYLÄ 2019

ABSTRACT

In this thesis, Doppler Optical Coherence Tomography (DOCT) was applied to velocity profiling rheometry in combination with rotational rheometer and pipe rheometer. In addition to the velocity profiling, the imaging modality of the OCT was utilized in characterizing the structural behavior of the materials under study. Furthermore, a novel hybrid multi-scale velocity profiling method, based on measuring stationary velocity profiles of fluid flow in a straight tube simultaneously by DOCT and ultrasound velocity profiling (UVP), was developed. The data from the two instruments can be combined into a comprehensive velocity profile including information on the thin boundary layer near the tube wall as measured by DOCT, and in the interior parts of the of flow as measured by UVP.

The experimental methods were used to investigate the rheology of aqueous microfibrillated cellulose (MFC) suspensions, which show complex rheological properties. It was found that flow curve measurements with rotational rheometer and smooth concentric cylinders are greatly affected by shear localization effects. In particular, conventional analysis of the bulk properties of MFC suspensions at shear stress values below their yield stress did not appear appropriate – despite the seemingly reasonable power-law flow curves thereby obtained.

Experiments with the pipe rheometer and hybrid multi-scale method showed that within the boundary layer concentration and thereby the viscosity of MFC decreases towards the wall. At high values of flow rate, sublayer of virtually pure water was observed next to the wall, giving rise to apparent wall slip. The results from the interior part of the flow showed shear-thinning behavior in qualitative agreement with results obtained by using conventional rheological methods.

Velocity profiling rheometry with DOCT and hybrid multi-scale methods appear useful in analyzing the rheological behavior of complex fluids. They can provide detailed experimental information on the rheology of MFC suspensions and their intricate boundary layer flow behavior, avoiding uncertainties inherent in many conventional rheological techniques.

Keywords: Doppler Optical Coherence Tomography, Velocity profiling, Complex fluids, Microfibrillated cellulose

Author's address   Sanna Haavisto
Spinnova Ltd.
Palokärjentie 2-4, 40320 Jyväskylä, Finland
Email: sanna.haavisto@spinnova.fi

Supervisors   Principal Investigator Antti Koponen
VTT Technical Research Centre of Finland

Professor Markku Kataja
Department of Physics
University of Jyväskylä, Finland

Reviewers   Professor Jouni Paltakari
Department of Bioproducts and Biosystems
Aalto University, Finland

Professor Fredrik Lundell
Department of Mechanics
KTH Royal Institute of Technology, Sweden

Opponent   Doctor Seppo Syrjälä
Materials Science and Environmental Engineering
University of Tampere, Finland

LIST OF PUBLICATIONS

This thesis is mainly based on the following publications, which are referred to in the text by their Roman numbers.

I   Haavisto, S., Salmela, J. & Koponen, A. 2015. Accurate velocity measurements of boundary-layer flows using Doppler optical coherence tomography. Experiments in Fluids 56 (5), 1-6.

II   Haavisto, S., Salmela, J., Jasberg, A., Saarinen, T., Karppinen, A. & Koponen, A. 2015. Rheological characterization of microfibrillated cellulose suspension using Optical Coherence Tomography. Tappi Journal 14 (5), 291-302.

III Saarinen T, Haavisto S, Sorvari A, Salmela J, Seppälä J. 2014 The effect of wall depletion on the rheology of microfibrillated cellulose water suspensions by optical coherence tomography. Cellulose. 21(3), 1261-75.

IV Kataja, M., Haavisto, S., Salmela, J., Lehto, R., & Koponen A. 2017. Characterization of micro-fibrillated cellulose fiber suspension flow using multi scale velocity profile measurements. Nordic Pulp&Paper Research Journal 32(3), 473-482.

SUPPORTING PUBLICATIONS

Haavisto, S., Cardona, M.J., Salmela, J., Powell, R.L., McCarthy, M.J., Kataja, M., & Koponen, A. 2017. Experimental Investigation of the Flow Dynamics and Rheology of Complex Fluids in Pipe Flow by Hybrid Multi-scale Velocimetry. Experiments in Fluids, 58(11), 158.

Salmela, J., Haavisto, S., Koponen, A., Jäsberg, A. & Kataja, M. 2013. Rheological characterization of micro-fibrillated cellulose fibre suspension using multi scale velocity profile measurements. Transactions of the 15th fundamental research symposium. The Pulp and Paper Fundamental Research Society, 495.

Sorvari, A., Saarinen, T., Haavisto, S., Salmela, J., Vuoriluoto, M., & Seppälä, J. (2014). Modifying the flocculation of microfibrillated cellulose suspensions by soluble polysaccharides under conditions unfavorable to adsorption. Carbohydrate polymers, 106, 283-292.

Lauri, J., Koponen, A., Haavisto, S., Czajkowski, J., & Fabritius, T. 2017. Analysis of rheology and wall depletion of microfibrillated cellulose suspension using optical coherence tomography. Cellulose, 24(11), 4715-4728.

AUTHOR'S CONTRIBUTION

Publication I: The author planned and carried out the experiments as well as the initial data analysis. The results were analyzed in co-operation with Antti Koponen. The author wrote the manuscript with the co-authors.

Publication II: The author participated in planning and implementation of the experiments with the co-authors. The author performed the OCT measurements and analyzed them together with Antti Koponen. The author wrote the manuscript with assistance of the co-authors.

Publication III: The author participated in defining the research plan, carrying out the OCT measurements, analyzing the OCT and image data, and writing the manuscript with the co-authors.

Publication IV: The author designed and built the experimental setup with co-author Juha Salmela. The author planned and carried out the measurements. The author analyzed the data in co-operation with Roope Lehto and participated in writing the manuscript with the co-authors.

ACKNOWLEDGEMENTS

First of all, I want to thank my supervisor Dr. Antti Koponen for the support and the engourament to continue with this process. I want to thank Prof. Markku Kataja for the supervision and possibility to finalize my studies in the University of Jyväskylä.

I would like to express my graditude to all my co-authors and collaborators for their valued contribution to the original articles. I have been fortunate to work with Anni Karppinen and Tapio Saarinen from Aalto University, Ari Jäsberg from VTT, and Roope Lehto from University of Jyväskylä. I give my special thanks to Juha Salmela for allowing this work to continue also at Spinnova. All my past colleagues at VTT and present colleagues at Spinnova are warmly thanked for creating an enthusiastic and encouriging working atmosphere. My grateful thanks are also extended to Emmi Berlin for intriguing conversations on English grammar and for revising the language of the manuscript.

Finally, I want to thank family and friends for supporting me along this process. If I ever was struggling with finding time or drive to write, you helped me out. Nobody has been more important to me than Noora, Martta, and Aarni. I wish to thank Minna and Varja for the priceless moments I have spent with you.

Jyväskylä 22.5.2019
Sanna Haavisto

CONTENTS

1 INTRODUCTION

Rheology is a branch of physics that studies deformation and flow of matter (Morrison 2001). The rheology of *simple fluids* is rather straightforward and well understood from a practical point of view. Their flow behavior can be characterized with either a single temperature dependent coefficient of viscosity (*Newtonian fluids*) or with relatively simple relations between the stress and the strain rate (*non-Newtonian fluids*). Furthermore, these material properties can be derived from conventional rheometric measurements relying on well-defined flow conditions. Unfortunately, in rheometry, it is impossible to establish general procedures for performing measuring and analyzing the data that would give real material characteristics, regardless of the material under study (Mewis & Moldenaers 1999). Especially, it may be very difficult to obtain valid and physically meaningful measurement results for inherently heterogeneous *complex fluids*. In fact, a large percentage of industrial as well as naturally occurring fluids are prone to exhibit phenomena inconsistent with the assumptions of, e.g., simple shear flow and no-slip boundary condition. These phenomena may result in severe misinterpretation of data from standard rheological measurements, which typically represent an average over the macroscopic behavior of the sample and are insensitive to the internal, localized dynamics of the complex fluids. The misinterpretation of the rheological response may, in turn, lead to poor predicting of e.g. the performance of the unit operations in processing or the properties of the finished product.

Microfibrillated cellulose fiber suspensions (MFC) fall into the category of complex fluids exhibiting peculiar flow behavior and rheological properties (Lasseuguette, Roux & Nishiyama 2008, Iotti et al. 2011). Being of great interest for many emerging applications, MFC materials and their rheology have been under active investigation during the last decade (Hubbe et al. 2017). The complexity of the rheological properties of MFC suspensions derives primarily from the inherent entangled heterogeneous network of fibrils with high specific surface area, aspect ratio, strength and flexibility (Lavoine et al. 2012). A specific issue that has not yet been thoroughly discussed in the literature is the role of inhomogeneous flow behavior in the observed rheological response of MFC suspensions (Karppinen et al. 2012, Martoïa et al. 2015, Mohtaschemi et al. 2014, Nazari et al. 2016, Nechyporchuk, Belgacem & Pignon 2014).

To mitigate problems in measuring rheological properties of complex fluids, an alternative approach to rheometry, namely velocity profiling rheometry, has been proposed. The crux of the velocity profiling rheometry is to combine conventional rheological techniques, such as rotational rheometers (Britton & Callaghan 1997) or tube (capillary) rheometers (Powell et al. 1994), with simultaneous measurement of spatially resolved flow velocity profile. The rheological analysis can then be based on an actually measured velocity profile instead of an assumed one. However, the measurement techniques mostly applied in velocity profiling rheometry have generally not been able to include the influence of the wall layer in the evaluation of the rheology for other than practically transparent fluids (Manneville 2008). The main reason for this has been a lack of experimental techniques suitable for opaque fluids, which could measure the velocity profile in the immediate vicinity of the wall, typically within a few tens of micrometers from the wall.

A recently adopted technique in the area of velocity profiling rheometry is Optical Coherence Tomography (OCT), or more specifically its functional extension Doppler OCT (DOCT). This method enables a direct non-invasive measurement of the velocity profile of a variety of materials, especially within turbid and opaque fluids. Due to the micrometer scale resolution and high measurement speed (tens of kHz) combined with the access to both internal structure and velocity field of the sample (Tomlins & Wang 2005), DOCT fills an apparent gap in the measurement methods available for complex fluids. Furthermore, DOCT is capable of accurate high-resolution measurement in the immediate vicinity of a channel wall, and is thus well suited in detailed study of the boundary layer behavior of complex fluids with suitable optical properties (Wang 2004, Malm et al. 2015). However, it is only in the last decade that the potential of DOCT in improving and extending the capabilities of rheological measurement techniques and methods has been realized (Harvey & Waigh 2011, Lauri, Bykov & Myllylä 2011, Jaradat, Harvey & Waigh 2012).

In this thesis, a commercial DOCT instrument was applied in velocity profiling rheometry aiming to review the spatial flow inhomogeneities encountered in viscometric flows. The DOCT was used in combination with rotational rheometer and pipe flow geometries. Furthermore, a novel hybrid multi-scale velocity profiling method, based on measuring stationary velocity profiles of fluid flow in a straight tube simultaneously by DOCT and Ultrasound Velocity Profiling (UVP), was developed. The DOCT and the hybrid method were used to study rheological properties and, in particular, boundary layer behavior of aqueous microfibrillated cellulose (MFC) suspensions. In addition to velocity profiling, the imaging modality of the OCT was utilized in characterizing the microstructural behavior of MFC suspensions near the pipe wall and in the rheometer gap aiming to further explain the rheological response of the suspensions.

The thesis is based on four publications. Publication I shows the applicability and performance characteristics of the applied DOCT system for measuring the average fluid flow properties in the near-wall region of pipe flow of water. Shear rheology and and spatial flow inhomogeneities of MFC suspensions in rotational rheometer are studied in Publications II and III.

Furthermore, in Publications III – IV, the hybrid velocity profiling is applied for studying the rheology and wall layer dynamics of MFC suspensions in tube flow. In addition, some unpublished data is presented to show the possibility of utilizing the structural information given by OCT in the analysis of the wall layer dynamics of MFC suspensions.

The thesis is organised as follows: Chapter 2 introduces general characteristics of complex fluids focusing on MFC suspensions. In Chapter 3, background of velocity profiling rheometry and the velocity profiling techniques utilized in this thesis are discussed. Chapter 4 describes the details of the MFC materials and the experimental setups used in this study. Chapter 5 presents the main results of the publications and highlights the role of DOCT in the rheological studies. Finally, in Chapter 6, a concluding summary is given.

2   RHEOLOGY OF COMPLEX FLUIDS

Simple fluids are materials that typically consist of a single substance and have purely fluid-like properties. In complex fluids, the bulk of the fluid is, instead, composed of two or more (immisicble) substances to form intrinsic structures characterized by mesoscopic length scales that are intermediate between microscopic (molecular) and macroscopic (system) length. Examples of such length scales are the diameter of oil droplets in an aqueous emulsion, the dimensions of particles in a liquid-particle suspension, and bubble size in aerogels or foams. The distinctive features of complex fluids appear expressly in their mesoscopic length scales, which lead usually to quite intricate properties and interesting physics of the material (Gelbart & BenShaul 1996, Barrat 2003). Perhaps the most astonishing features of complex fluids are their rheology and flow properties. Complex fluids may have properties in between solids and fluids, and their rheological response may show both elastic and viscous characteristics depending on the type of the imposed deformation. Furthermore, the internal mesoscopic structure of a complex fluid is easily reorganised during e.g. deformation in viscometric flow (Witten 1990). In general, reorganisation effects include alignment of polymer chains or fibers, flocculation of particles, and favorable spatial distributions of particles or droplets (Barnes 1997). The reorganisation, in turn, incites the flow field, possibly resulting in different kinds of spatial and/or temporal flow inhomogeneities. In e.g. simple shear, the flow behavior may show phenomena such as apparent wall slip, particle migration, shear banding, and thixotropy, all of which are caused by various physical mechanisms (Leighton & Acrivos 1987, Barnes 1995, Barnes 1997, Olmsted 2008).

Complex fluids under consideration in this thesis are aqueous suspensions of microfibrillated cellulose (MFC) in concentrations where the rheological and flow properties of these suspensions are dominated by the MFC component. Before discussing the features of MFC suspensions, the foundation of the rheological approach for the study of complex fluids is presented. In this context, the concept of shear viscosity and different types of non-Newtonian rheological behavior are briefly considered in section 2.1. Furthermore, in section 2.2, a summary of the rheometric methods relevant to this thesis is given, addressing especially the inhomogeneous flow behavior encountered in conventional rheometry

applied in complex fluids. Finally, in section 2.3, a brief overview of MFC suspensions and their properties relevant to the results of this thesis is presented based on selected recent review articles on MFC materials.

2.1 Non-Newtonian fluid behavior

Shear viscosity is the most widely characterized rheological property of fluids; including complex fluids. Contrary to that of a Newtonian fluid, the viscosity of non-Newtonian fluids is often dependent on the applied shear rate (and may depend even on shear rate history). The standard rheological approach is to subject a fluid to shear deformation, such as Couette flow, and find the relationship between the stress τ [Pa] and the shear rate $\dot{\gamma}$ [s^{-1}] as

$$\tau = \mu(\dot{\gamma})\dot{\gamma}. \tag{2.1}$$

The shear-rate-dependent viscosity $\mu(\dot{\gamma})$ [Pa·s] is often termed as apparent viscosity. The apparent viscosity, in turn, is typically described in terms of (more or less) suitable rheological models that include various material parameters that must be found experimentally (Morrison 2001, Irgens 2016). A schematic description of typically observed types of non-Newtonian rheological behavior is shown in Figure 1. Corresponding rheological models and examples of such fluids are summarized in Table 1.
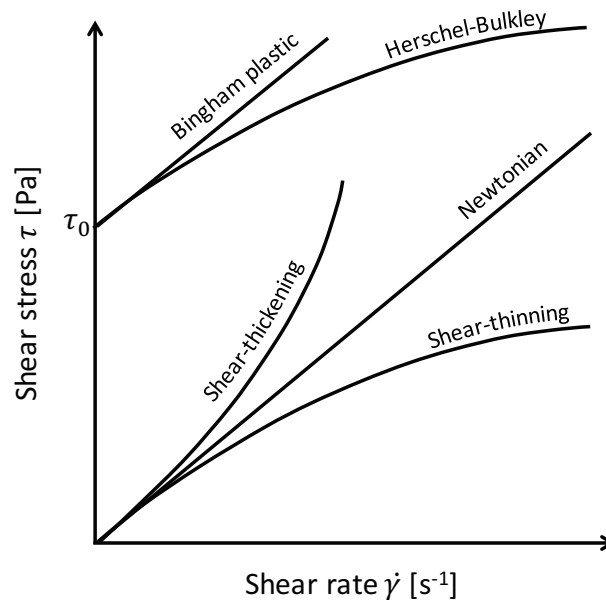

Figure 1   Schematic illustration of typical viscosity behavior (flow curves) exhibited by non-Newtonian fluids.

Rather large group of fluids may be characterized by power-law type rheological behavior, which can be divided into three different classes based on the value of the exponent (also called flow index). For a Newtonian fluid, the flow index

equals one, for a shear-thinning fluid, the index is smaller than one, and for a shear-thickening fluid, it is larger than one. Shear-thinning and shear-thickening behaviors are also referred to as pseudoplastic and dilatant behaviors, respectively. A linear or shear-thinning curve $\tau(\dot{\gamma})$ intersecting the shear stress axis at a shear stress value of τ_0 instead of origin are characteristic for a Bingham plastic or Herschel-Bulkley type of materials, respectively. These yield stress fluids appear solid for stresses below a critical limit τ_0 and start to flow when this limiting shear stress is exceeded. Although these models are relatively simple, and for example the existence of yield stress as a physical reality has been debated in the literature, they can nevertheless be useful in predicting steady-state flow in a limited range of shear rates (Barnes 1999, Bonn & Denn 2009).

Table 1   Equations and parameters of common rheological models for non-Newtonian fluids.

Model name	Equation	Parameters	Examples
Power-Law	$\tau = K\dot{\gamma}^n$	K: Consistency Index [Pa · s^n] n: Flow Index [-], with 　　$n < 1$ Shear-thinning 　　$n = 1$ Newtonian 　　$n > 1$ Shear-thickening	Latex paint Water Aqueous corn starch suspension
Herschel-Bulkley	$\tau = \tau_0 + K_1\dot{\gamma}^{n_1}$	τ_0: Yield Stress [Pa] K_1: Consistency Index [Pa · s^n] n_1: Flow Index [-]	Aqueous microfibrillated cellulose suspension
Bingham Plastic	$\tau = \tau_b + \mu_b\dot{\gamma}$	τ_b: Bingham Yield Stress [Pa] μ_b: Bingham Viscosity [Pa·s]	Clay suspensions, mayonnaise, mustard

While the above-mentioned models can characterize general flow behavior of various fluids, they cannot capture time-dependent behavior. In practice, viscosity may depend not only on the shear rate but also on the time for which the fluid has been sheared. Fluids that exhibit decreasing shear stress and apparent viscosity with the time of shearing at a fixed shear rate are called thixotropic fluids. Conversely, the viscosity of a rheopectic fluid increases with time of shearing. Such phenomena typically occur due to the breakdown (thixotropic) or build-up (rheopectic) in the structure of the material as shearing continues. Thixotropic fluid behavior is observed with many industrially important materials, such as pastes, paints, coatings, and sealants. The reviews by Barnes and Mewis & Wagner provide a comprehensive description on thixotropic behavior in rheology (Barnes 1997, Mewis & Wagner 2009). Fluids exhibiting rheopectic behavior are not very common. However, rheopectic behavior should be considered for dispersions with very high concentration of solid matter or gel-like particles (Mezger 2006).

2.2   Rheometry and viscometric flows

Shear rheometry relies on very simple (laminar) flows that provide straightforward relations between stress components and flow history. The main classes of flows in this purpose are viscometric flows and extensional flows. The

term viscometric flow embodies the uniform, simple shear flow and the non-uniform shear flows, such as tube flow and slit flow. Viscometric flows must satisfy certain conditions to be rheologically steady, which essentially means that the deformation rate of the fluid is not changing with time. Furthermore, the fluid behavior is governed by three functions: viscosity, and first and second normal stress coefficients (Coussot 2005, Irgens 2016). Extensional flows are not within the scope of this thesis but are well covered in standard textbooks on rheology, such as that by F. Irgens (Irgens 2016).

A wide range of methods exists to characterize the rheology of complex fluids. The most frequently employed rheometric methods are based on rotational geometries (shear flow) or flow through a capillary tube (pressure-driven flow), which are considered also in this thesis. Detailed discussion on the working principles of rheometers and their applications can be found in e.g. References (Morrison 2001, Irgens 2016).

2.2.1 Rotational rheometry

In rotational rheometry (drag flow) shear is generated between two surfaces, of which one is typically moving while the other is kept stationary. The main geometries of rotational rheometers, i.e., plate geometries and concentric cylinders, are illustrated in Figure 2. In addition, shown is a vane and cup geometry, which is often used for structured complex fluids (Barnes & Nguyen 2001). For example, in the concentric cylinders an approximation of uniform shear rate throughout the sample is realized by shearing the fluid in the narrow annular gap between the cylinders. In a typical setup, the inner cylinder (bob) is rotated, and the outer cylinder (cup) is stationary. A known angular velocity (or torque) is imposed on the rotor, and the torque (or angular velocity) offered to the rotor is measured. Provided that the gap is small ($\ll R_2$), the velocity profile of a Newtonian fluid is linear as long as the flow remains laminar and stationary. For an angular velocity of ω and torque M acting on the cylinder surface, the shear rate $\dot{\gamma}$ [s^{-1}] and shear stress τ [Pa] are

$$\dot{\gamma} = \frac{R_2 \omega}{(R_1 - R_2)} \tag{2.2}$$

$$\tau = \frac{M}{2\pi R_2 h}, \tag{2.3}$$

where h, R_1 and R_2 are the height and radii of the outer and inner cylinders, respectively. The coefficient of viscosity may be calculated as $\mu = kM/\omega$, where k is an instrument constant dependent the dimensions of the measurement geometry. The constant k may be calibrated to include also other factors, such as the end effect of the inner rotating cylinder (Morrison 2001).
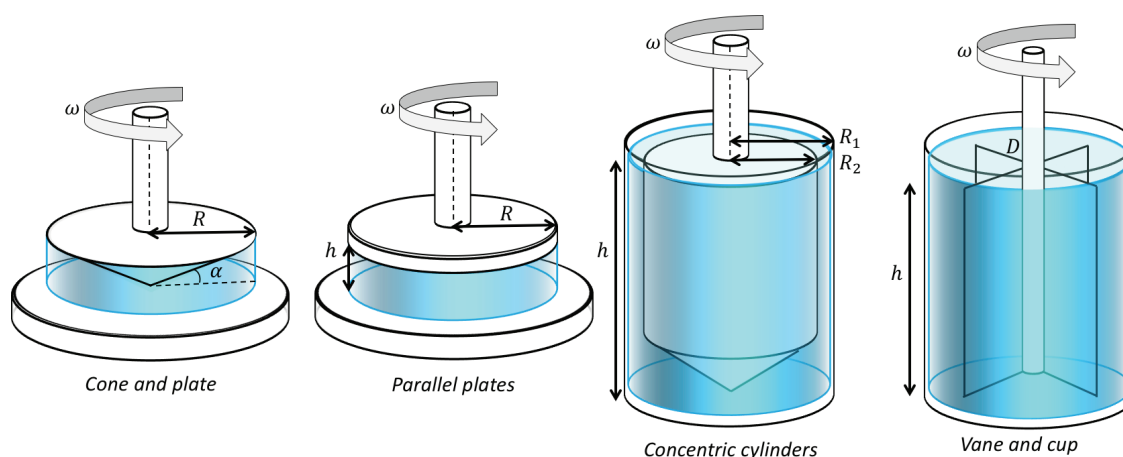
Figure 2   Schematic illustration of flow geometries commonly used in rotational rheome-
            try. Starting from left: cone and plate, parallel plates, concentric cylinders, and
            vane and cup. The gap between the cone(plate) and the plate as well as the
            concentric cylinders is typically ~ 1 mm.

The rotational rheometers are powerful, as they can be used in diverse ways to
perform rheological tests. In particular, they are considered useful for studying
flow behavior of fluids that have long time scales in e.g. relaxation or stabilization
because the applied strain (or time) is not limited. Thus, rotational rheometers
are a preferred choice for information concerning the molecular structure and its
effects on stability and processability of a fluid. On the other hand, due to flow
instabilities, rotational rheometers face limitations in the high shear rate region,
when shear rates exceed 1000 s^{-1}. Another source of limitations may be the size
of the gap being too small in terms of the mesoscopic structures of the studied
complex fluid (Mezger 2006).

    In a typical rheological experiment, the change in viscosity and stress of the
sample is measured as a function of applied steady state shear rate (see Figure 1).
This so-called flow curve can be measured for ascending and descending shear
rates, to find out whether the rheology of a sample depends on flow history. In
addition to steady shear measurements, steady extension, stress relaxation, creep,
and oscillatory shear are typically used in rheological characterization with rota-
tional rheometers. In particular, oscillatory shear is routinely used in character-
izing the viscoelastic properties of complex fluids. In an oscillatory test, both
strain and stress vary cyclically with time, allowing the measurement of relative
contributions of viscous and elastic responses of the studied material. The mate-
rial is commonly characterized by the viscoelastic moduli, storage modulus (G')
and loss modulus (G''), describing the elastic and viscous contribution to the
measured stress and strain. These tests are typically carried out in the linear vis-
coelastic regime, where the strain and the stress imposed on the material are re-
versible. Conventionally, the linear viscoelastic regime of a sample is at first
determined using an oscillatory strain sweep. The further measurements, such as
oscillatory frequency sweeps, are then performed at a strain, which lies in the
linear viscoelastic regime. More detailed discussion on the oscillatory rheometry
can be found in e.g. references (Deshpande 2010, Mezger 2006).

2.2.2 Capillary rheometry

Perhaps the simplest device for measuring a shear viscosity of a fluid is the capillary (tube) rheometer. While it is not as versatile technique as rotational rheometers, the capillary rheometer enables the viscosity measurements in relevant processing ranges. Capillary rheometers can apply very high pressures, which enables the measurements in high shear rate processes, such as extrusion and spraying.

The main components of a capillary rheometer are a reservoir that holds the studied fluid and a capillary tube through which the fluid is forced to flow by an imposed pressure (see Figure 3). The rheometer may be operated at constant pressure or constant flow rate. The viscosity is determined by measuring the total pressure drop ΔP [Pa] and flow rate Q [m^3/s] in a steady, fully developed laminar flow through a uniform circular tube of length L [m] and radius R [m], i.e. Poiseuille flow (Sutera & Skalak 1993). The length of the capillary tube is many times larger than its small diameter, so that the total pressure drop may be assumed to result from overcoming the viscous forces.

In the case of a Newtonian fluid, the velocity profile in the capillary is parabolic in shape. Consequently, the shear rate is the highest at the wall, and zero at the centerline of the tube. The shear rate and shear stress along the walls of the capillary are given by the equations

$$\dot{\gamma}_W = \frac{4Q}{\pi R^3}. \tag{2.4}$$

$$\tau_w = \frac{\Delta P R}{2L}. \tag{2.5}$$

The above equations can be used to calculate the viscosity at the wall. The result is also known as the Hagen-Poiseuille law, which gives the viscosity in terms of the flow rate, pressure drop, and the tube radius as

$$\mu = \frac{\pi R^4 \Delta P}{8QL}. \tag{2.6}$$

Equations 2.4 and 2.6 give the true shear rate and viscosity for Newtonian fluids but apparent shear rate for non-Newtonian fluids. Typical presumptions made concerning the flow are incompressibility and constant temperature of the fluid, and no-slip condition (zero velocity) at the capillary wall. However, for complex fluids, significant entrance effects, wall-slip and deviation from a parabolic profile are observed. In order to account for these effects, various special techniques and corrections to the measured data have been suggested (Morrison 2001). For instance, the non-parabolic shape of the velocity profile of shear-thinning fluids may be taken into account using the classical Weissenberg-Rabinowitsch correction (Rabinowitsch 1929).
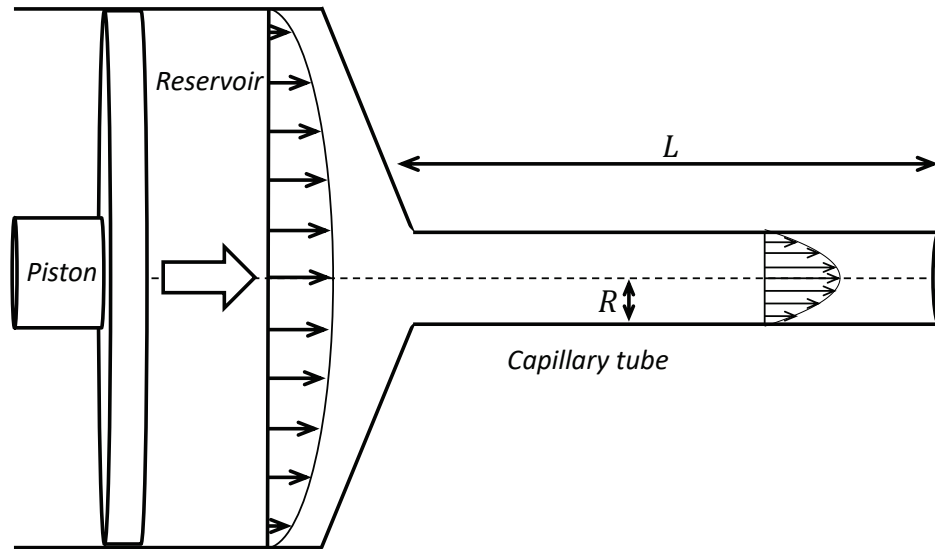
Figure 3   Schematic illustration of the basic structure of a capillary rheometer.

2.2.3   Complex behavior in rheometry

A crucial aspect in standard rheometry employing viscometric flows is that the flow kinematics resulting from shearing a complex fluid is assumed similar to that of a Newtonian fluid. While such approach is not necessarily correct, in general, it may be appropriate for many homogeneous non-Newtonian fluids, and useful in rough classification of different complex fluids in terms of basic rheological behavior (shear-thinning, shear-thickening, etc.). However, without direct observation of the nature of the flow (velocity profile) and structure of the fluid during the measurement, there are many possible sources of error and misinterpretation that may render the measured rheological information inadequate for predicting flow behavior in actual processing conditions. A detailed review on the complex phenomena encountered in rheometry as well as mechanisms causing them is presented in (Mewis & Moldenaers 1999). As background for later discussion on the rheological properties of microfibrillated cellulose suspensions, the different phenomena of shear localization are discussed here in more detail.

The concepts of shear localization and shear banding cover a range of phenomena in which the shear rate (velocity) profile in a flowing material exhibits an apparent discontinuity (Ovarlez et al. 2009). Figure 4 presents schematic examples of such velocity profiles in a simple Couette flow. The velocity profile of a homogeneous flow (Figure 4a) is linear and the local shear rate corresponds to the macroscopic shear rate. The flow in Figure 4b is, in turn, shear-banded showing two macroscopic regions with different values of shear rate for a given stress. Consequently, the apparent viscosity and state of microstructural organization in these regions is different. Shear banding has been observed with several types of complex fluids including suspensions, emulsions, polymer solutions, and granular materials (Olmsted 2008). Møller et al. even suggested that shear banding (localization) is an intrinsic property of yield stress fluids that is always encountered at low enough shear rates (Møller, Mewis & Bonn 2006). The

mechanisms of flow-structure coupling behind the transition to shear banded flows with different fluid systems exhibiting these phenomena have been discussed in references (Fielding 2007, Olmsted 2008, Ovarlez et al. 2009, Divoux et al. 2016). These mechanisms include e.g. entanglement (flocculation) effects and changes in the topology of micellar systems, such as breakage or enhanced length and liquid-crystalline effects (Olmsted 2008). In rheometry, effects of shear banding are usually observed as characteristic kinks, plateaus, and non-monotonic shape in the (spatially averaged) flow curve (Olmsted 2008, Divoux et al. 2016).
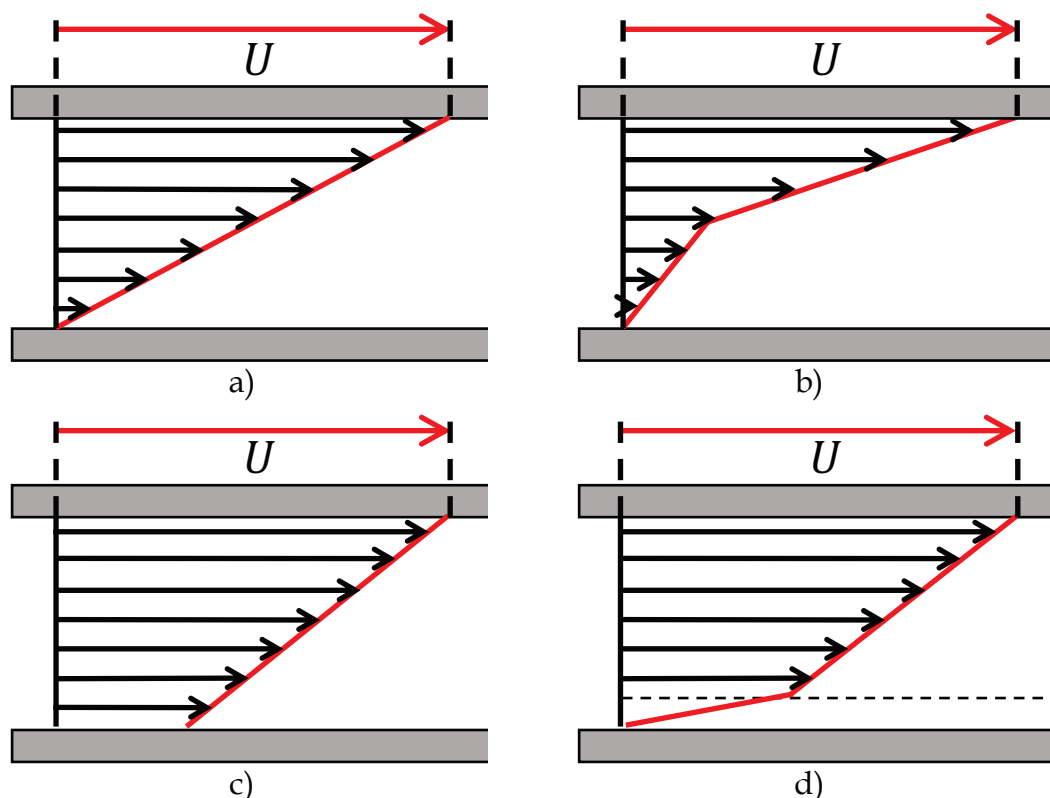

Figure 4   Schematic illustration of flow velocity profile in simple shear flow for a) homogeneous flow, b) shear-banded flow, c) flow with true wall slip, and d) flow with apparent wall slip. Notice that the wall slip can occur on both surfaces.

In Figure 4c and d, shown are flows exhibiting wall slip, which may be considered to represent an extreme case of the shear localization. When wall slip occurs, the overall deformation of the fluid is localized in a thin layer adjacent to the (moving and/or stationary) wall, resulting in a large velocity gradient at the wall. In the case of "true slip", (Figure 4c) there are no or only very small adhesive forces between the molecules of a fluid and the wall. Thus, the molecules themselves slip over the wall, and the slip layer is of molecular dimension (Barnes 1995). True slip has been observed in e.g. flows of polymer melts (Léger et al. 1997).

Apparent wall slip (Figure 4d) corresponds to a situation where the local velocity varies over a mesoscopic distance, which is typically very small compared to e.g. the gap of rotational rheometer geometry. For suspensions, slip occurs due to formation of a low-viscosity layer (also referred as slip or depletion layer) resulting from migration of solid particles away from the wall (Leighton &

Acrivos 1987, Blanc, Peters & Lemaire 2011). Generally, this effect originates from steric, hydrodynamic, viscoelastic, chemical or gravitational forces acting on the solid phase in the vicinity of solid boundaries (Barnes 1995). In addition to the shearing conditions, the width of the apparent slip layer depends on the particle size and concentration of the suspension. The apparent slip velocity, in turn, depends on temperature, concentration, particle size, and wetting properties of the wall (Sochi 2011). The phenomenon of slip is not just of academic interest; it has also significant practical relevance (Cloitre & Bonnecaze 2017). For instance, in pipe flow, the formation of a water-rich layer may lead to significant apparent wall slip resulting in considerable increase of the volumetric flow rate of e.g. pulp suspensions (Jäsberg 2007).

Slip effects can be present in all rheometers but they occur more easily at smooth boundaries. Slip may be suppressed by implementing physically textured surfaces in the rheometer geometry instead of smooth ones (Buscall 2010). Furthermore, the slip effects can be determined by using correction procedures (Mewis & Moldenaers 1999) such as the well-known Mooney method (Mooney 1931). However, the correction methods based on the macroscopic rheological behavior assume that slip is the only source of inhomogeneous behavior, which may not be the case with complex fluids. In flow curves, slip may be observed as a sudden decrease in viscosity in a narrow shear rate interval or as Newtonian plateaus (Barnes 1995).

Plug flow is yet another shear localization effect originating from the strong nonlinearity of the rheological behavior of some complex materials. This relates particularly to yield stress fluids, which can exhibit yielding (flowing) regions and unyielded (static plug) regions within the same sample (Ovarlez et al. 2009). For instance, a concentrated suspension of starch particles in silicon oil flowing in a straight tube at low velocity exhibits plug flow in the middle of the pipe (Ouriev & Windhab 2002b). Inside the plug, the fluid behaves similarly to a solid body that moves at a constant velocity with the flow. Outside the plug, the fluid is exposed to shear stresses exceeding the yield stress leading to shear-thinning behavior. The velocity profiles of yield stress fluids are further addressed in Section 3.1. It is noteworthy that shear localization effects may also coexist or behave in a counterintuitive manner with regard to changes in shear stress. For instance, coexisting plug flow and lubrication layer near the walls is a long-known phenomenon with the tube flow of papermaking fiber suspensions (Duffy et al. 1976). Furthermore, microgel pastes have been observed to exhibit different regimes of slip depending on the applied stress. At high shear stresses the slipping behavior is peculiar; the slip appears to decrease with increasing shear stress (Meeker, Bonnecaze & Cloitre 2004).

2.3 Rheology of microfibrillated cellulose suspensions

Microfibrillated cellulose (MFC) and nanofibrillated cellulose (NFC) are biomass materials of the pulp and paper industry and the agricultural sector (García et al.

2016). The unique characteristics of MFC and NFC, combined with environmental friendliness, make them an interesting target for research, which has been growing rapidly in the past decade. MFC/NFC materials have been found to have a potential in a wide spectrum of applications. It has been suggested that these materials would be applicable as e.g. components in bio-nanocomposites (Siró & Plackett 2010), barriers in cellulosic products (Lavoine et al. 2012), additives in papermaking (Osong, Norgren & Engstrand 2016, Boufi et al. 2016), and raw material for spinning filaments for textile and composite industries (Clemons 2016, Lundahl et al. 2016).

2.3.1 What is MFC?

MFC/NFC is made from wood pulp or other sources of cellulose, such as agricultural crops or other plant fibers through homogenization process, where the fibers are degraded and opened into their substructural fibrils and micro- or nanofibrils (Jonoobi et al. 2015). In its simplest form, MFC/NFC is prepared purely by mechanical disintegration of wood pulp, as was first introduced by Turbak et al. and Herrick et al. already in the early 1980s (Turbak, Snyder & Sandberg 1983, Herrick et al. 1983). Mehanical processing can be realized with e.g. grinders, homogenizers, or microfluidizers, and can be accompanied by chemical (Wågberg et al. 2008, Liimatainen et al. 2014) or enzymatic (Pääkkö et al. 2007) pretreatment in the preparation. These pretreatments lower the energy demand in the disintegration process, which has been one of the main issues preventing the industrial scale-up of the MFC/NFC production (Spence et al. 2011). Furthermore, pretreatments enable preparation of not only highly fibrillated materials, but also individual fibrils that are completely detached from each other (Saito et al. 2009).

In addition to (Jonoobi et al. 2015), recent reviews on production of micro- and nanocellulosic materials are provided in (Nechyporchuk, Belgacem & Bras 2016) and (Kargarzadeh et al. 2017). Besides presenting the preparation methods of various kinds of MFC/NFC from different sources, these reviews discuss the effects of these methods on the properties of the produced materials as well as the classification principles of the micro/nanocellulose materials. These topics are not further addressed in this thesis.

With regard to the standard terms of cellulose materials (TAPPI W13021) (Kargarzadeh et al. 2017), this thesis concentrates on cellulose microfibrils (CMF) obtained by mechanical disintegration of wood pulp fibers without any pre- or post-treatments. Due to naming policy adopted in the publications of this thesis, the acronym MFC is generally used to refer to these materials. In literature, the terms MFC and NFC rougly correspond to different size ranges of nanostructured materials. The term "nano" is used to emphasize a smaller size range, indicating that at least one external dimension of the fibrils is in the nanoscale (1-100 nm) (Hubbe et al. 2017).

2.3.2   Physical and chemical aspects of MFC suspensions

Mechanical disintegration of wood cell structure (Ioelovich 2013) results in a polydisperse suspension containing both nanoscale and microscale elements with a broad range of diameters and lengths. The nanoscale (colloidal) elements are elementary fibrils or bundles of fibrils that consist of cellulose crystals linked along the fibril axis by disordered amorphous domains. The degree of crystallinity is usually low, as a substantial part of the amorphous domains of the original cellulose structure remain essentially intact, resulting in the very high aspect ratio (length divided by diameter) and highly expanded surface area of the fibrils (Vartiainen et al. 2011, Lavoine et al. 2012). According to the standard established for MFC materials, the diameter of the fibril structures range between 10 and 100 nm, and length between 0.5 and 50 μm (TAPPI W13021). The microscale (noncolloidal) elements in MFC are usually partially fibrillated cellulose fibers, i.e. fiber fragments.
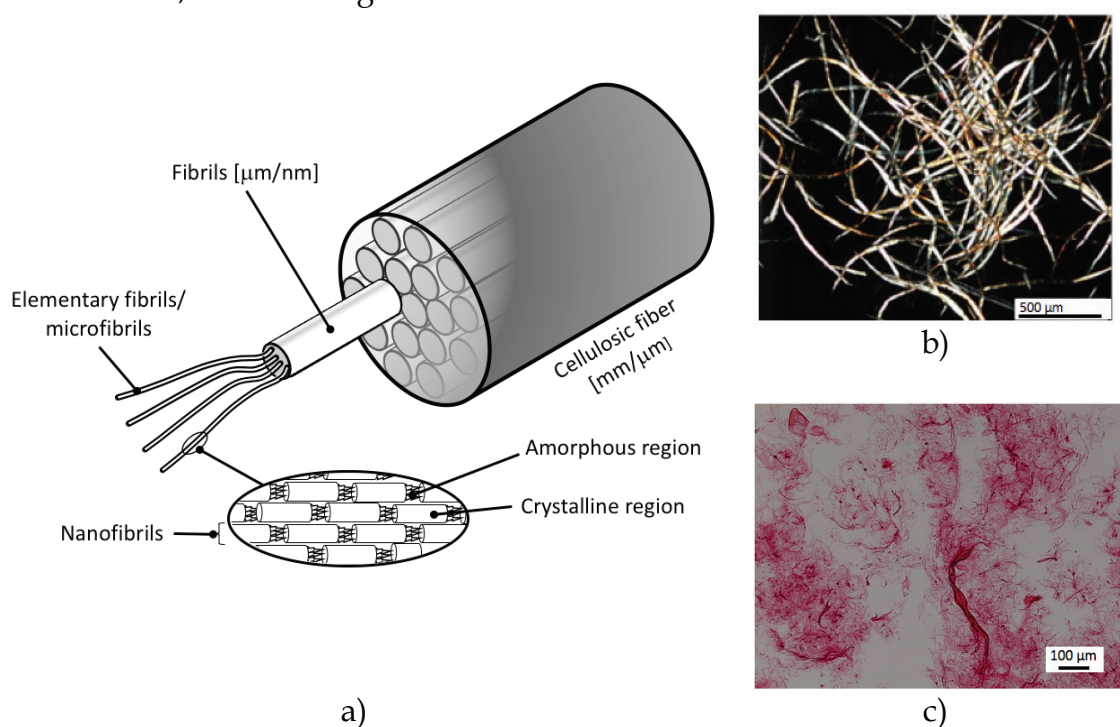

Figure 5   a) Schematic of cellulosic fiber structure adapted from (Lavoine et al. 2012, Kargarzadeh et al. 2017). The size scales of structures are shown as [length/width]. b) Microscopic image of papermaking (hardwood) fibers. c) Microscopic image of mechanically prepared microfibrillated cellulose (MFC) showing fibril bundles and fiber fragments. Image b) was taken by Martina Lille, and image c) by Ulla Salonen.

To sum up, aqueous MFC suspensions consist of strongly entangled and disordered networks of fibrils, also called primary flocs, rather than individual fibrils. Such structure leads to gel-like properties of MFC systems already at very low (~0.1%) mass concentrations. Furthermore, the gels formed by these inherent networks may be much stronger when compared to those formed by low aspect ratio fibrils (Pääkkö et al. 2007). The connectivity and rigidity of the network

formed by the primary flocs have been described in terms of crowding factor N [−] originally derived from consideration of suspensions of papermaking fibers as

$$N = \frac{2}{3} C_v A^2. \tag{2.7}$$

Here, C_v is the volume concentration of the fibrous material in the suspension, and A is the aspect ratio of the fibers or MFC fibrils (Kerekes & Schell 1992). In practice, Equation 2.7 means that longer fibers and higher concentration increase the tendency of fibers to entangle and flocculate as they develop more contacts between each other. The rigidity (flocculation) threshold, where the floc structure is coherent and able to bear mechanical strength, occurs at $N \cong 60$. The connectivity threshold or gel point, in turn, occurs at $N \cong 16$ and describes the lowest concentration at which the fibers or primary flocs are interconnected and form a self-supporting network (Martinez et al. 2001, Celzard, Fierro & Kerekes 2009). An aspect ratio of 100, for instance, yields a gel point in solids concentration of ~0.3%, and concentrated (flocculated) state in concentration of ~1.2%. Here, the solids concentration has been calculated using $C = (\rho_{\text{MFC}}/\rho_{\text{water}})C_v$, where ρ_{MFC} is assumed to be 1330 kg/m³ (Varanasi, He & Batchelor 2013). Although derived from the viewpoint of papermaking fibers (assumed as cylinder-shaped), experimentally determined gel points and aspect ratios have been useful in e.g. evaluating the production of MFC (Raj et al. 2016) and predicting the sheet forming ability of MFC based on its size distribution (Zhang et al. 2012).

Due to the high aspect ratio and low surface charge of the fibrils, the MFC suspensions are also prone to flocculation (aggregation). An imaging-based approach adopted from research of macroscopic fiber suspensions has shown that MFC in sheared suspensions consist of flocculated structures the size of which depends on the shearing conditions. In spite of the large difference in dimensions and aspect ratio, the MFC floc structure is to some extent similar to pulp suspensions (Saarikoski et al. 2012). However, possessing structures of also colloidal (nano) scale, MFC suspensions are more susceptible to changes in surface charge, surface structure, and ionic strength of the suspending fluid compared to macroscopic fibers (Hubbe & Rojas 2008). Suspensions of chemically modified MFC/NFCs are colloidally more stable and usually not flocculated, but some physical entanglements may still be present (Nechyporchuk, Belgacem & Bras 2016).

2.3.3 Rheological characterization of MFC suspensions

Rheological properties of MFC suspensions are important not only in characterizing the properties of MFC fibrils but also during their preparation, processing, storage, and mixing with other materials. Therefore, the rheology of different MFC materials has been under active investigation during the past decade (Hubbe et al. 2017). A frequently noted issue when dealing with aqueous MFC/NFC suspensions is their complex rheological behavior (Nechyporchuk, Belgacem & Pignon 2016, Naderi 2017). However, the reported rheological

characteristics of MFC suspensions have a broad variability, which causes concern from the viewpoint of industrial scale-up (Hubbe et al. 2017).

The rheological response of MFC suspensions primarily derives from their inherent entangled heterogeneous network. The dimensions and flexibility of the fibrils as well as the degree of fibrillation directly affect the colloidal and noncolloidal behavior of the MFC suspension both at macroscopic (volume fraction and rotation of the fibers) and microscopic (dispersion, electrostatic, and steric forces) scale, and thereby contribute to the flocculation and rheology of the suspensions (Taheri & Samyn 2015). As a result, the rheological response of MFC suspensions depends not only on the cellulose raw material (Zimmermann, Bordeanu & Strub 2010, Colson et al. 2016) or preparation method (Taheri & Samyn 2016, Moberg et al. 2017), but also on suspension concentration (Pääkkö et al. 2007, Iotti et al. 2011, Karppinen et al. 2012), ionic strength (Lowys, Desbrieres & Rinaudo 2001, Saarikoski et al. 2012, Naderi, Lindström & Sundström 2014), pH (Pääkkö et al. 2007, Agoda-Tandjawa et al. 2010), temperature (Iotti et al. 2011, Naderi & Lindström 2016, Shafiei-Sabet, Martinez & Olson 2016), and presence of additives (Karppinen et al. 2011, Sorvari et al. 2014, Naderi, Lindström & Sundström 2014).

Regardless of the vast amount of factors affecting their rheology, aqueous MFC suspensions generally exhibit shear-thinning characteristics (Lavoine et al. 2012, Nechyporchuk, Belgacem & Pignon 2016). The shear thinning of mechanically disintegrated MFC suspensions has been attributed to breaking of flocculated structures and consequent alignment of the fibrils with the flow. Changes in the MFC floc (fibril aggregate) structure correlate with a change in the shear stress in a following manner: At low shear stress, flocs are attached to each other. When shear stress is increased, the floc structure starts to yield via flocs separating from each other. At high shear stresses, fibrils flow in individual, detached flocs, the size of which is inversely proportional to the shear stress (Karppinen et al. 2011, Karppinen et al. 2012, Saarikoski et al. 2012).

On the context of shear thinning, many authors have observed a three-region behavior of MFC suspensions in shear viscosity measurements (Figure 6). In both low ($\dot{\gamma} \lesssim 1\,\mathrm{s}^{-1}$) and high shear rates ($10\,\mathrm{s}^{-1} \lesssim \dot{\gamma} \lesssim 1000\,\mathrm{s}^{-1}$), these suspensions show shear-thinning behavior that may be characterized by a power-law or Herschel-Bulkley models (Karppinen et al. 2011). Between the shear thinning regions, at intermediate shear rates of ($1\,\mathrm{s}^{-1} \lesssim \dot{\gamma} \lesssim 10\,\mathrm{s}^{-1}$) the shear viscosity measurements are characterized by a kink or (Newtonian) plateauing region both in mechanically disintegrated MFCs (Iotti et al. 2011, Karppinen et al. 2012, Saarikoski et al. 2012) and MFCs prepared using chemical treatments (Pääkkö et al. 2007, Lasseuguette, Roux & Nishiyama 2008, Martoïa et al. 2015, Naderi, Lindström & Sundström 2014). Such plateauing region has been observed with different measurement geometries, including plate-and-plate (Agoda-Tandjawa et al. 2010, Iotti et al. 2011) and concentric cylinders (Lavoine et al. 2012). A recent study reports kinks also with concentric cylinders with roughened surfaces and vane geometry (Schenker et al. 2018). Furthermore, the positioning of the kinks in the flow curves has been attributed to the degree of fibrillation of the MFC material. The kinks are shifted towards lower shear rates due to formation of larger aggregates with highly entangled MFC systems (Naderi 2017).
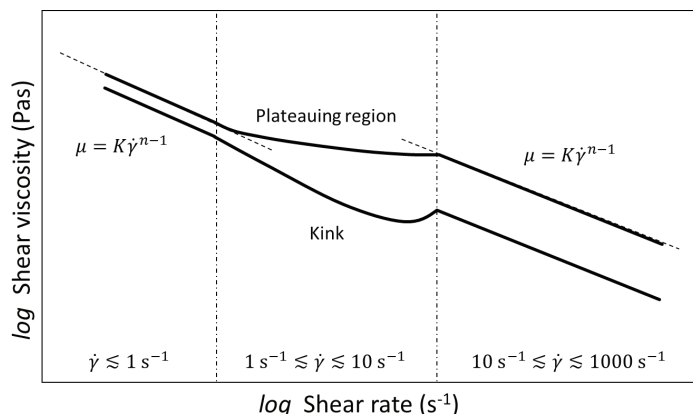
The figure shows a schematic plot with axes labeled *log* Shear viscosity (Pas) on the y-axis and *log* Shear rate (s^{-1}) on the x-axis. Labels include "Plateauing region", "Kink", $\mu = K\dot{\gamma}^{n-1}$ (two locations), and shear rate regions $\dot{\gamma} \lesssim 1\,\mathrm{s}^{-1}$, $1\,\mathrm{s}^{-1} \lesssim \dot{\gamma} \lesssim 10\,\mathrm{s}^{-1}$, $10\,\mathrm{s}^{-1} \lesssim \dot{\gamma} \lesssim 1000\,\mathrm{s}^{-1}$.

Figure 6 Schematic of typical flow curves of MFC suspensions showing three distinct regions. Both high shear rate ($10\,\mathrm{s}^{-1} \lesssim \dot{\gamma} \lesssim 1000\,\mathrm{s}^{-1}$) and low shear rate ($\dot{\gamma} \lesssim 1\,\mathrm{s}^{-1}$) regions follow a power law behavior. At intermediate shear rates of ($1\,\mathrm{s}^{-1} \lesssim \dot{\gamma} \lesssim 10\,\mathrm{s}^{-1}$) the shear viscosity measurements are characterized by a kink or (Newtonian) plateauing region.

The entanglement of the fibrillated network (of also chemically treated MFCs) widely influences rheological properties other than shear-thinning characteristics, such as zero-shear viscosity (Lasseuguette, Roux & Nishiyama 2008, Zimmermann, Bordeanu & Strub 2010, Jowkarderis & van de Ven, Theo GM 2014), yield stress (Tatsumi, Ishioka & Matsumoto 2002, Agoda-Tandjawa et al. 2010, Haavisto et al. 2011), and shear thickening at very high shear rates (Iotti et al. 2011), which are affected by, e.g., the degree of fibrillation and suspension concentration. MFC suspensions have also shown significant thixotropic behavior and hysteresis effects (Martoïa et al. 2015, Iotti et al. 2011).

Oscillatory shear measurements (see Chapter 2.2.1) have indicated that MFC suspensions exhibit rigid solid-like viscoelastic (G'>G'') properties that are pronounced when the solids concentration is increased. Furthermore, MFC suspensions have been reported to possess yield stress and show power-law correlation between storage modulus (G') and concentration, similar to pulp suspensions (Tatsumi, Ishioka & Matsumoto 2002, Lasseuguette, Roux & Nishiyama 2008, Agoda-Tandjawa et al. 2010, Shafiei-Sabet, Martinez & Olson 2016) However, according to review by Hubbe, the exponent of the power-law equation varies between 0.2 and 3.7 depending on the type of MFC/NFC (Hubbe et al. 2017). Otherwise, attributes such as the level of fibrillation (Saarinen, Lille & Seppälä 2009, Taheri & Samyn 2016) and the effect of chemical conditions (Saarikoski et al. 2012, Korhonen et al. 2014) on the viscoelastic response of MFC suspensions have been studied. Literature discussing the linear viscoelastic properties of different MFC suspensions have been reviewed recently in (Nechyporchuk, Belgacem & Pignon 2016).

Rheological properties of MFC suspensions have been measured utilizing mainly rotational rheometry (Iotti et al. 2011, Taheri & Samyn 2015), but also capillary or tube rheometers, and slit flow (Haavisto et al. 2011, Iotti et al. 2011, Kumar et al. 2016) have been applied. It has been reported that flocculation, orientation, flow instabilities, migration from solid boundaries, as well as high

time dependency of MFC suspensions complicates the rheological measurements (Dimic-Misic et al. 2014, Nechyporchuk, Belgacem & Pignon 2016). Furthermore, factors arising from improper sample preparation or inappropriate measurement geometry can cause discrepancy and poor reproducibility of the results, or in the worst case rough misinterpretation of the rheological behavior. It has been observed that, in general, intensive mixing and resting period (pre-shearing) are needed for MFC suspensions in order to regain their initial viscosity and to achieve repeatable results. Furthermore, recommendations on suitable measurement geometries (Saarinen, Lille & Seppälä 2009, Schenker et al. 2018), preferably with serrated surfaces instead of smooth ones (Nechyporchuk, Belgacem & Pignon 2014) have been discussed. However, commonly accepted protocols for sample preparation and characterization of MFC-based systems are still lacking (Naderi & Lindström 2015, Naderi 2017).

A point that has not yet been thoroughly discussed in the literature is the role of inhomogeneous flow behavior in the observed rheological response of MFC suspensions. Similarly to pulp fibers or particle suspensions in general, MFC suspensions are also prone to wall depletion. Especially low shear rates are prone to slip flow that can introduce a significant error in the rheological measurements (Nechyporchuk, Belgacem & Pignon 2014). In addition, other shear localization effects as well as thixotropic behavior have to be considered when interpreting rheological measurement data (Iotti et al. 2011, Martoïa et al. 2015, Nechyporchuk, Belgacem & Pignon 2015). To overcome these difficulties hindering the precise assessment of the rheology of MFC suspensions (or other complex fluids), advanced rheometric techniques are needed.

3 VELOCITY PROFILING RHEOMETRY

Interpretation of experimental results from conventional rheological measurement of complex fluids may be hampered by incomplete knowledge of the actual flow conditions that prevailed during the measurement. This may be related to e.g. complicated boundary layer phenomena or multiphase effects, such as flow induced structural inhomogeneity of the flow (Fielding 2007, Olmsted 2008, Divoux et al. 2016). This limitation has triggered development of experimental methods to probe structural and flow heterogeneities during rheological measurements. For instance, rheometer setups with optical access in the sample coupled with structural probing techniques, such as digital imaging, birefringence methods, light scattering (SALS) and neutron (SANS) scattering enable experimental investigation of the link between peculiar macroscale rheology and mesoscale phenomena (Manneville 2008). Despite being informative, mere visualization or structural probing cannot provide measurement of the local velocity nor accurate estimation of the rheology of the material. To better understand the behavior of complex fluids in rheometry, velocity profiling rheometry has been proposed. The crux of the velocity profiling rheometry is to combine conventional rheological techniques with simultaneous measurement of spatially resolved flow velocity profile. The rheological analysis can then be based on an actually measured velocity profile instead of an assumed one. Various velocity profiling techniques, including ultrasound velocity profiling (UVP) (Derakhshandeh, Hatzikiriakos & Bennington 2010, Shiratori et al. 2015), ultrasound imaging velocimetry (UIV) (Poelma et al. 2012, Gurung et al. 2016), ultrasound speckle velocimetry (USV) (Manneville, Bécu & Colin 2004a), nuclear magnetic resonance imaging velocimetry (NMRI) (Gibbs et al. 1996, Hanlon et al. 1998), and particle imaging velocimetry (PIV) (Dimitriou et al. 2012) have been used for this purpose. One of the newest techniques in the field of velocity profiling rheometry is Doppler Optical Coherence Tomography (DOCT). Unlike any other technique, DOCT is capable of accessing both velocity field and structural information of non-transparent flows in the immediate vicinity of a channel wall (Tomlins & Wang 2005).

Another reason for the interest in the velocity profiling rheometry has been the potential of especially UVP and NMRI, to be used as in-line viscometers in

process monitoring and quality control (Arola et al. 1997, Wiklund 2007, Birkhofer et al. 2008, Ricci et al. 2012, Rahman, Håkansson & Wiklund 2015). For example, rheological data obtained by UVP in real processing conditions have been shown to be in good agreement with the macroscopic behavior deduced from conventional rheometry for a wide range of fluids (Wiklund & Stading 2008).

In this chapter, the foundation of the velocity profiling rheometry, including aspects of practical application, is presented. The chapter is continued by discussing the measurement techniques, i.e. ultrasound velocity profiling and optical coherence tomography, adopted in the experimental part of this thesis. In addition to summarizing the basic principles of the two measurement techniques, key factors affecting the performance of them are discussed. References to more detailed background information are also given.

3.1 Background

Here, a steady, fully developed, pressure driven laminar flow in a tube with circular cross section is considered. The theory of the velocity profiling rheometry is based on two independent observations illustrated in

Figure 7. Firstly, the shear rate $\dot{\gamma}$ [s^{-1}] as a function of radial position y [m] of the tube is calculated by differentiating the measured velocity profile $u(y)$ [m/s]:

$$\dot{\gamma}(y) = \frac{du(y)}{dy} \qquad (3.1)$$

Secondly, the conservation of linear momentum prescribes that the shear stress τ [Pa] at position y is

$$\tau(y) = \tau_w \left(1 - \frac{y}{R}\right); 0 \leq y \leq R. \qquad (3.2)$$

Shear stress thus vanishes at the centerline of the tube and increases linearly to its maximum value at the tube wall. Here, τ_w [Pa] corresponds to the wall shear stress and R [m] to the pipe radius. The wall shear stress can be obtained from pressure drop measurement ΔP [Pa] over distance L [m] as

$$\tau_w = \frac{\Delta P R}{2L}. \qquad (3.3)$$

The radial distribution of shear viscosity $\mu(y)$ [Pa $\cdot$ s] is thus given by

$$\mu(y) = \frac{\tau(y)}{\dot{\gamma}(y)}. \qquad (3.4)$$

Each velocity profile measured at a specific value of $\Delta P/L$ thus gives viscosity values in a range of shear rates present in the profile. Theoretically, the values range from zero to the maximum shear rate, usually found at the tube wall. The studied shear rate range may be extended by taking measurements at several flow rates. Furthermore, since the $\dot{\gamma}(y)$ is known (Equation 3.1), the viscosity can also be expressed as a function of $\dot{\gamma}$, i.e. $\mu(\dot{\gamma})$, which is a typical representation of the viscometric function or rheogram.
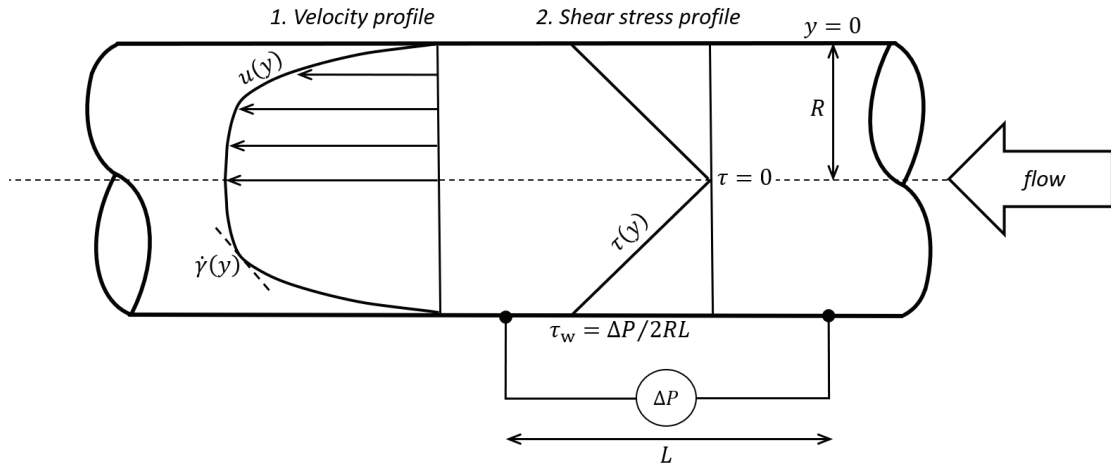
Figure 7   Principle of the velocity profiling rheometry in a straight tube (radius R). Each flow rate gives a velocity profile – pressure drop pair $(u(y), \tau(y))$, from which the viscosity data is obtained over the range of shear rates $\dot{\gamma}(y)$ present in the velocity profile. The shear stress profile $\tau(y)$ is calculated using the pressure drop ΔP over the distance L.

The shape of the velocity profile depends on the rheological properties of the fluid. While Newtonian fluids have a simple parabolic profile, complex fluids develop different profile shapes, as shown in Figure 8. For materials with a yield stress (τ_0), the velocity profile may exhibit plug flow in the center of the pipe, where the shear stress is less than the yield stress. Actual shearing occurs only in the region $(0 < y < y_0)$ where the shear stress exceeds the yield stress. Using Equation 3.2, the yield stress value is related to the plug radius y_0 by:

$$\tau_0 = \tau_w \left(1 - \frac{y_0}{R}\right). \tag{3.5}$$

Equations 3.1 – 3.5 provide the foundation for measuring the shear viscosity and the yield stress by using the gradient method, i.e. local calculation of the shear rate from the measured velocity profile. It is noteworthy that these equations are valid only if the flow is fully developed. Although the equations were presented for tube flow, similar methodology is applicable for other flow geometries as well (Manneville, Bécu & Colin 2004b, Wassenius & Callaghan 2005).

The advantage of the gradient method is that it does not require a priori assumptions concerning the type of the constitutive relation or the velocity profile of the fluid. On the other hand, quite a high resolution for the velocity data is needed in order to extract quantitative rheological results across the whole tube radius (Brunn, Müller & Wunderlich 1997). Calculation of the low shear rates towards the center of the tube is strongly affected by the velocity resolution and noise level of the velocity profiling system. The maximum measurable shear rate, present close to the tube walls, is limited by the spatial resolution of the velocity data. This, in turn, is influenced by the wall effects and by the finite size of the measuring volume characteristic to the particular velocimetric techniques used. A typical approach to gradient method is to approximate the measured velocity

data by a continuous curve, often a polynomial, and use that for calculating the shear rate (Dogan, McCarthy & Powell 2002, Pfund et al. 2006).
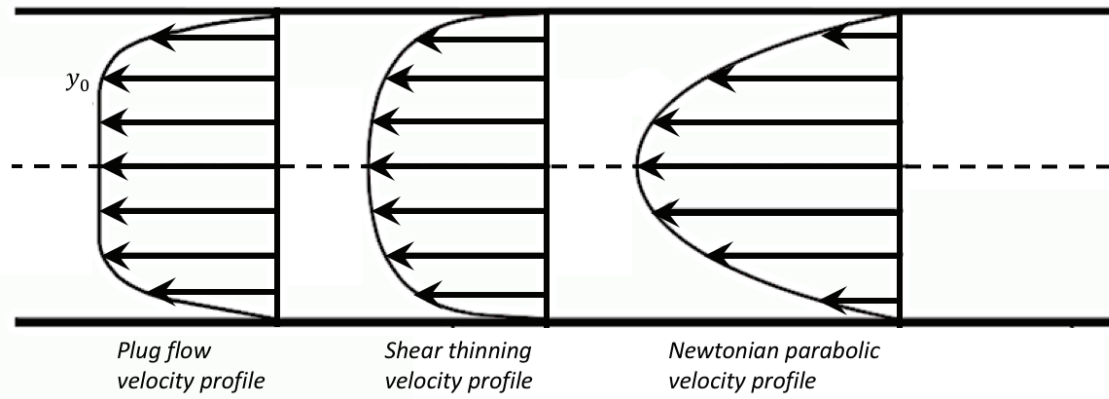

Figure 8   Velocity profiles for fluids with different rheological behaviors: Plug flow (left), shear-thinning (middle), and Newtonian (right). The edge of the plug is marked with y_0 in the plug flow profile.

Given the measured velocity data and the pressure drop, it is also possible to fit the velocity profiles to integrated forms of the different rheological models, such as power-law or Herschel-Bulkley. The model parameters are thus obtained directly from the fit (Dogan, McCarthy & Powell 2002, Ouriev & Windhab 2002a, Wiklund & Stading 2008, Derakhshandeh, Hatzikiriakos & Bennington 2010). However, introducing a priori rheological models requires special attention in interpretation of the near-wall phenomena encountered with complex fluids, as was discussed in Chapter 2.2.3.

3.2   Ultrasound velocity profiling

The use of pulsed ultrasonic Doppler method for velocity measurements outside the biomedical field was started in the mid-1980s by (Takeda 1986). Takeda was also the first to apply this technique in the engineering field, where it is referred to as ultrasound velocity profiling (UVP), ultrasound Doppler velocimetry, ultrasonic Doppler method, and ultrasound pulse Doppler. The main advantages of the UVP method are its non-invasivity, applicability to optically opaque fluids, relatively low cost, portability, and ease of implementation for online or inline measurements in various processes. UVP has been utilized in many fields of fluid dynamics and engineering such as flow rate measurements (Wada et al. 2004, Tezuka et al. 2008), flow mapping (Ouriev & Windhab 2002a, Kantoush et al. 2008, Kotzé et al. 2011), turbulence (Nowak 2002, Jaafar, Fischer & Bekkour 2009), and multiphase flows (Wang et al. 2003). Fundamentals and description of various applications of UVP may be found in (Takeda 2012).

In the field of complex fluids, one of the most common applications of UVP is the velocity profiling rheometry in pipe flow geometry. As the wall shear stress in pipe flow is obtained from pressure difference (PD) measurement, this method

is often referred to as UVP-PD in the literature. In fact, methodologies (Wiklund, Shahram & Stading 2007) and patents (Han et al. 2001, Ouriev & Windhab 2005) utilizing the UVP-PD method for rheological measurements have been established. Conventional rheometry coupled with local velocimetry measurements by UVP have been used to study the rheology of complex fluids as well. For example, Derakshandeh et al. have implemented UVP in rotational rheometer equipped with vane-in-a-large-cup geometry (Derakhshandeh, Hatzikiriakos & Bennington 2010).

3.2.1 Principle of UVP

The UVP is based on using an emitter-receiver transducer to send a series of short ultrasound (US) pulses into the flow, and detecting the echoes issuing from the target particles that move along with the flow. A typical schematic of the implementation of an UVP system is shown in Figure 9. A single transducer (probe) is mounted at a specific inclination angle with respect to the main flow direction. The probe emits a pulse train of ultrasonic waves, typically in a frequency range of $1 - 10$ MHz, through acoustic coupling and wall material in to the sample fluid. Immediately after emitting a pulse, the UVP system is switched to receiving mode and the reflected Doppler-shifted echoes are sampled at specific time windows Δt_i ($i = 0, ..., n$), also called gates or channels. The distance y_i [m] of each gate from the probe surface along the its measurement line is determined by the time of flight of the ultrasonic wave as

$$y_i = \frac{c \Delta t_i}{2},$$ (3.5)

where c [m/s] is the speed of sound in the flowing medium and Δt_i [s] is the time interval between transmitting and receiving the ultrasound signal.

In principle, the local velocity values at each gate along the transducer axis can be calculated using the Doppler equation. For the geometry in Figure 9, the equation is

$$u_i = \frac{c f_{D,i}}{2 f_0 \cos(\alpha)},$$ (3.6)

where u_i [m/s] is the velocity component in the flow direction, c [m/s] is the speed of sound in the flowing medium, $f_{D,i}$ [Hz] is the Doppler frequency shift for gate i, f_0 [Hz] is the ultrasound emitter frequency, and α ($\lesssim 90°$) is the Doppler angle. Here, the angle is defined as the angle between the probe measurement axis and the main flow vector.

In reality, the particles scattering ultrasound are randomly distributed inside the ultrasonic beam. Hence, also the received echo signal issuing from the particles is random. In practice, Doppler frequency, and thus the velocity of the scattering objects, is carried out by performing a series of emissions with a fixed pulse repetition frequency and analyzing the demodulated signal using either time domain or frequency domain-based signal processing. More detailed discussion on this is presented in Chapter 3.3.3 dealing with velocity profiling by Doppler optical coherence tomography.
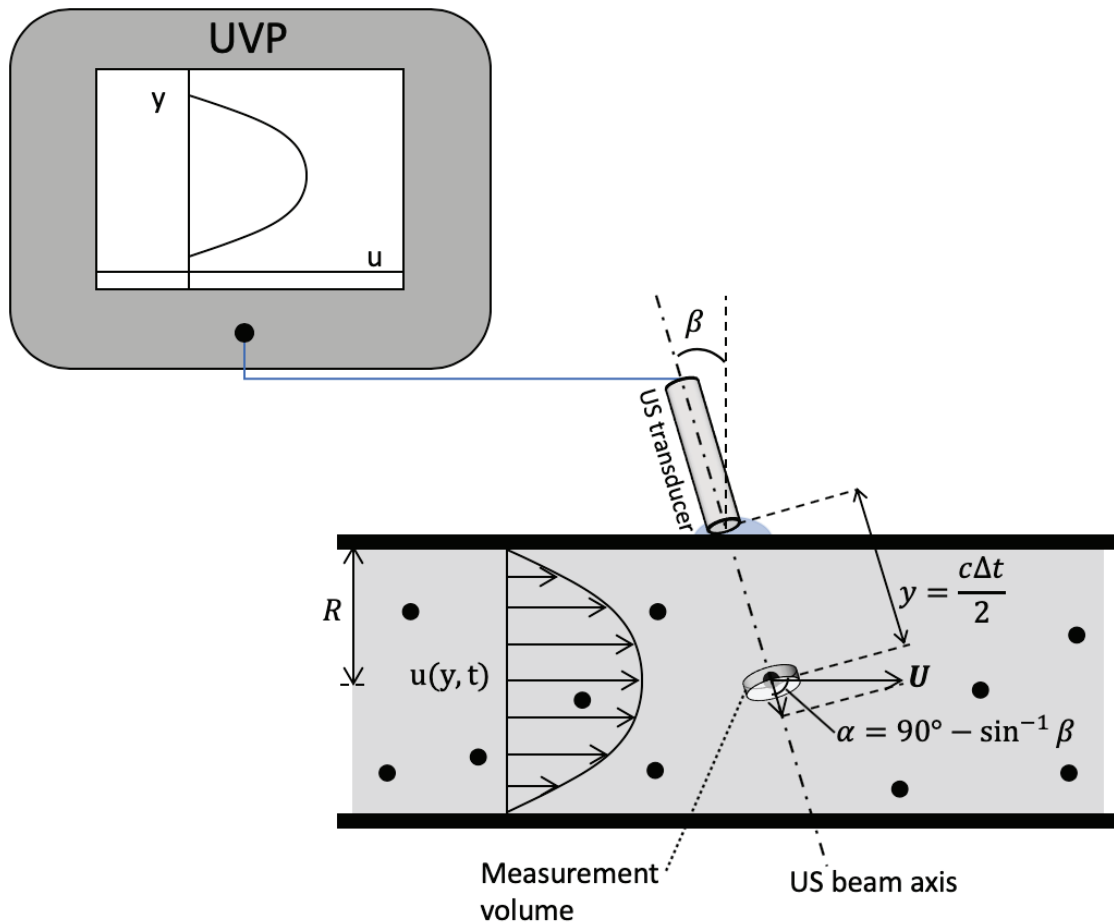
Figure 9   Typical experimental setup for a UVP measurement in a pipe flow. The UVP
gives the component u of the velocity vector U in the direction y of the US
transducer beam. The angle β is the angle between the transducer axis and the
pipe surface normal. The angle α is the Doppler angle. Here, the US velocity in
the coupling medium and in the flowing fluid is assumed similar.

3.2.2   Factors affecting performance of UVP

The factors affecting the performance of the UVP technique come from many
sources. In this section, the most important of them are discussed. More detailed
reviews on these factors can be found in (Murakawa, Mori & Takeda 2012) and
(Messer & Aidun 2009).

The first two factors considered here appear explicitly in the Equation 3.2,
namely the Doppler angle α and the speed of sound c. As the UVP measures a
single velocity component in the direction of the ultrasound beam, the flow ve-
locity u is susceptible to systematic error related to uncertainty in the Doppler
angle α. While increasing the measurement angle close to 90° enables the meas-
urement of higher velocities in the mainstream direction, already a very small
angle error $\Delta\beta$ amplifies error in the velocity measurement. The relative error in
velocity due to setting angle of the transducer $\Delta\beta$ may be estimated as $\frac{\Delta\beta}{\tan\beta}$ (Mu-
rai et al. 2012).

The speed of sound varies depending on the medium propagating the sound waves. In water, the speed of sound depends on pressure, temperature, and salinity of the water. The propagation of uncertainty to velocity measurement due speed of sound has been discussed in (Kotzé et al. 2011). Furthermore, special equipment for monitoring the speed of sound continuously during the UVP measurement has been designed to help in minimizing the uncertainties related to the sound velocity (Wiklund, Shahram & Stading 2007).

The second category of factors affecting the performance of the UVP arises from the measurement parameters. The time resolution of the measurement is determined by the number of emissions N_e and the pulse repetition frequency f_{PRF} as $N_e \times \frac{1}{2\pi f_{PRF}}$ [Hz]. Furthermore, the time resolution has to be selected so that enough time is allowed for the signal from the most distant measurement location to be collected by the probe before the next pulse is sent. In other words, the maximum measurable depth for the given pulse repetition frequency and Doppler angle is

$$y_{max} = \frac{c \cos \alpha}{2 f_{PRF}}. \tag{3.7}$$

Another limitation to the maximum measurable velocity (frequency) is given the Nyquist theorem according to which frequencies exceeding half of the sampling frequency f_{PRF} are aliased among the measured low-frequency data. Thus, the maximum quantifiable velocity in the direction of the US beam axis is $u_{max} = \frac{c f_{PRF}}{4 f_0}$. The trade-off between the maximum depth and the maximum velocity can be expressed as (Powell 2008)

$$u_{max} y_{max} = \frac{c^2}{8 f_0}. \tag{3.8}$$

As the UVP data is obtained at discrete points in time, the velocity data points represent an average velocity over the volume element corresponding to shape of the US beam. The shape of the volume element is approximately cylindrical (see Figure 9) with effective radius determined by the probe's piezoelectric element generating the ultrasonic pulse train. The diameter (D) and shape of the volume element changes along the measurement axis as the US beam slightly diverges. Most of the beam acoustic energy is contained in a cone with the half angle of

$$\delta = \text{asin} \frac{1.22 c}{D f_0}. \tag{3.9}$$

The axial length h [m] of the measurement volume equals one half of the spatial width of the ultrasonic pulse:

$$h = \frac{c N}{2 f_0}, \tag{3.10}$$

where N [−] is the cycles within a single pulse (Pfund et al. 2006). For example, an ultrasound transducer with a 5-mm piezoelectric element emitting pulses of 4 MHz and 4 cycles generates measurement volumes with a divergence angle of 5.2° and an axial length of 0.75 mm in water. Notice that the longitudinal dimension of the actual sampling volume may be also affected by the bandwidth of the

electronic receiving unit. If the duration of the emitted pulse is longer than the value associated to the bandwidth, the sampling volumes are overlapping.

If the ultrasound travels through e.g. an acoustic coupling material and a pipe wall, as is the case in Figure 9, the initial angle of the US signal changes according to the Snell's law. If the US velocity in the coupling material and in the measured fluid are close to each other, the difference between the transducer setting angle (β) and the Doppler angle (α) is often ignored (Wang et al. 2003). However, the physical changes in the US beam introduce errors in the velocity profile through Doppler angle, particularly in the near-wall region. This, together with the finite sampling volume mentioned earlier, makes it difficult to accurately measure the velocity profile close to the wall. Correction procedures for the measured near-wall velocity profiles based on deconvolution (Flaud, Bensalah & Peronneau 1997, Kotze, Wiklund & Haldenwang 2013), Snell's law (Wang et al. 2003), and geometrical formulae (Wunderlich & Brunn 2000, Kikura, Yamanaka & Aritomi 2004) have been proposed.

3.3   Optical Coherence Tomography

Optical Coherence Tomography (OCT) is a rather new member in the family of optical sensors (Fercher et al. 2003, Drexler & Fujimoto 2008). It was introduced in the early 1990s for biomedical purposes (Huang et al. 1991, Hitzenberger 1991). OCT is analogous to ultrasound imaging but uses light instead of sound. Because of the extremely high velocity of light, direct measurement of optical echoes cannot be realized electronically, but is instead based on low coherence interferometry of light (LCI). The OCT technique enables noninvasive cross-sectional imaging with a micron-scale resolution in a highly scattering medium. Unlike ultrasound, OCT does not require direct contact with the target nor a transmitting medium, but the imaging can be performed through air over a distance of a few centimeters (Drexler 2004). Historical development, theoretical fundamentals, as well as technological applications and extensions of OCT can be found in (Fercher et al. 2003, Drexler & Fujimoto 2008). In particular, applications outside the biomedical field have been reviewed in (Stifter 2007).

One of the most important functional extensions of OCT is the Doppler OCT (DOCT) where the velocity information is retrieved simultaneously with structural imaging. Despite the studies on blood flow, velocity profiling with DOCT has not to date been extensively applied in industrially motivated problems. Applications utilizing both the velocity profiling and imaging modalities of OCT have mainly been in the field of microfluidics (Proskurin, Sokolova & Wang 2003, Xi et al. 2004, Ahn, Jung & Chen 2008, Cito et al. 2012), and fouling of surfaces (Wagner & Horn 2017). Velocity profiling rheometry with DOCT has been successfully carried out in a rotational rheometer (Harvey & Waigh 2011), a capillary type viscometer (Lauri, Bykov & Myllylä 2011), and an elongational rheometer (Dufour et al. 2005). In addition to providing accurate determination of viscosity, OCT has been capable of capturing various perturbative phenomena encountered in rheological experiments of complex fluids, such as wall depletion, slip

flow, and shear banding (Harvey & Waigh 2011, Jaradat, Harvey & Waigh 2012, Malm, Harrison & Waigh 2014, Sorvari et al. 2014).

3.3.1 Principle of OCT

The physical foundation of OCT is in light interference. Interferometry is a common technique for detecting echo time delay and amplitude of back-scattered light with a high sensitivity. There are several different methods for performing OCT, such as time domain OCT (TD-OCT), spectral (frequency) domain OCT (SD-OCT), swept source OCT (SS-OCT), and their modifications (Drexler & Fujimoto 2008). Here, a spectral domain-based Michelson interferometer setup shown in Figure 10 is used to illustrate the OCT imaging principle.

In a typical SD-OCT setup, a broadband, low-coherence light source, e.g. a super luminescent led (SLD) is used. The light beam emitted by the SLD is split into the reference arm (L_{REF}) and sample arm (L_S) of a Michelson interferometer. The properties of the light beam exiting the arms are controlled by various optical components, such as mirrors and lenses. In the reference arm, the light is reflected back by a reference mirror, whereas the light in the sample arm is backscattered by the sample. When the returning light signals from the both arms are recombined, an interference pattern is generated (Fujimoto 2003). The interference pattern contains simultaneous information of the location, scattering index, and the travelling speed of the light-scattering structures within the sample. In SD-OCT, a spectral interrogation utilizing fast Fourier transform (FFT) is carried out at the interferometer output to extract a depth profile, without movement of the reference arm (Wojtkowski 2010).

A single axial depth profile acquired by OCT is typically referred to as A-scan. Two-dimensional slice images (B-scans) can be constructed by employing scanners to acquire multiple A-scans at different lateral locations. The resulting data set is a spatial distribution back-scattering index of light within the cross-sectional slice of the sample. The scattering index may be correlated with e.g. density or solids content. Furthermore, three-dimensional sets can be generated by acquiring sequential B-scans. The 3D-OCT data contain volumetric structural information and can be manipulated similarly to other three-dimensional tomographic images.
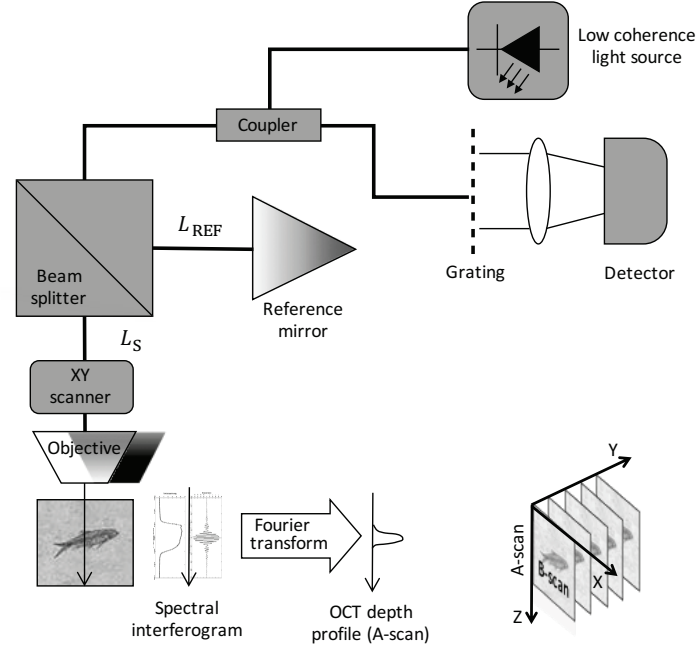
Figure 10   Principle of the Spectral Domain OCT measurement. L_{REF} and L_S are the reference and sample arm of the Michelson interferometer, respectively. Cross-sectional images are constructed by performing axial A-scans at different lateral positions resulting in 2D cross-sectional maps (B-scans) of the scattering indices inside the sample.

3.3.2   Key factors affecting the performance of OCT

The general performance of an OCT system is determined by the broadband light source. The central wavelength and optical bandwidth of the light source determine the axial resolution, which equals the half of the source coherence length

$$\Delta y \approx 0.44 \frac{\lambda^2}{\Delta \lambda}, \tag{3.11}$$

where λ [m] and $\Delta\lambda$ [m] are the central wavelength and the spectral FWHM (Full Width at Half Maximum) of the light source, respectively (Tomlins & Wang 2005). Typical axial resolutions in the OCT devices lie in the region of 1 – 15 µm. The axial resolution at infrared and optical wavelengths, which are commonly used, is limited to about 1 μm, even if the bandwidth of the light covers a wide spectral range (Drexler 2004, Fujimoto & Drexler 2008). The achievable penetration depth of OCT depends strongly on the sample properties but also on the source wavelength. With near-infrared light sources up to several millimeters of penetration depth can be achieved with semi-transparent materials. If the imaged medium scatters too much, the light beam weakens quickly, and the intensity of the backscattered light is low. Optically too dense particles or regions in the imaged material block the penetration of the OCT signal deeper in the medium producing shadowing that typically occurs as straight dark lines in the OCT images. Also, if the scattering level is too low, the amount of observed backscattered light drops quickly with increasing distance from the probe. Thus, for acquiring velocity information within transparent materials, such as pure water, addition of light

scattering tracer particles is necessary. The tracer amount has to be optimized with respect to the intensity and penetration depth of the OCT signal (Lauri, Bykov & Myllylä 2011).

The lateral resolution of an OCT system is decoupled from the axial resolution. Instead, it is determined by the probe optics, similar to the case of imaging optics. The higher numerical aperture gives a better lateral resolution. In practice, the lateral resolution and the depth of focus are governed by the focused beam size. The intensity profile across the beam has 2D Gaussian shape.

Other major factors determining the performance of an OCT instrument are its dynamic range, sensitivity and data acquisition rate. Comparing to some tomographic techniques, OCT can perform cross-sectional imaging at a relatively fast rate, i.e., tens of Hz. The axial scanning speeds used to produce the cross-sectional images can be hundreds of kilohertz. For more detailed physical fundamentals as well as comparison of different OCT methods and their essential parameters can be found in e.g. (Schmitt 1999, Fercher et al. 2003, Brezinski 2006, Drexler & Fujimoto 2008).

3.3.3 Doppler OCT

Doppler OCT (DOCT) combines the Doppler principle with OCT to obtain velocity information simultaneously with high-resolution structural imaging (Chen & Zhang 2015). In analogy to UVP, the measurement of the Doppler frequency is carried out utilizing two or more sequential A-scans and analyzing the demodulated signal using either time domain or frequency-domain based signal processing. Any change between the A-scans can be attributed to a Doppler frequency shift induced by moving objects as

$$f_D = \frac{\Delta\varphi(y)}{2\pi} f_A \, , \tag{3.12}$$

where $\Delta\varphi$ is the phase shift at position y [m], and f_A [Hz] is the A-scan rate of the OCT system. Several Doppler OCT algorithms and technical implementations have been proposed to detect the Doppler frequency shift (Liu et al. 2012). Assuming an angle α between the flow and the OCT beam (see Figure 11a), one component v of the flow velocity vector is obtained along the beam direction

$$v(y) = \frac{\lambda f_D}{2\cos\alpha} = \frac{\lambda \Delta\varphi(y) f_A}{4\pi n \cos\alpha}. \tag{3.13}$$

Here, λ [m] is central wavelength of the light source and n is the refractive index of the medium (for air $n = 1$). Similar to the Doppler ultrasound methods, the uncertainty imposed by the angle α applies also to DOCT. The advantage of DOCT is, however, that the Doppler angle can be found more directly using 2D or 3D structural images (Michaely et al. 2007, You et al. 2014, You et al. 2017).
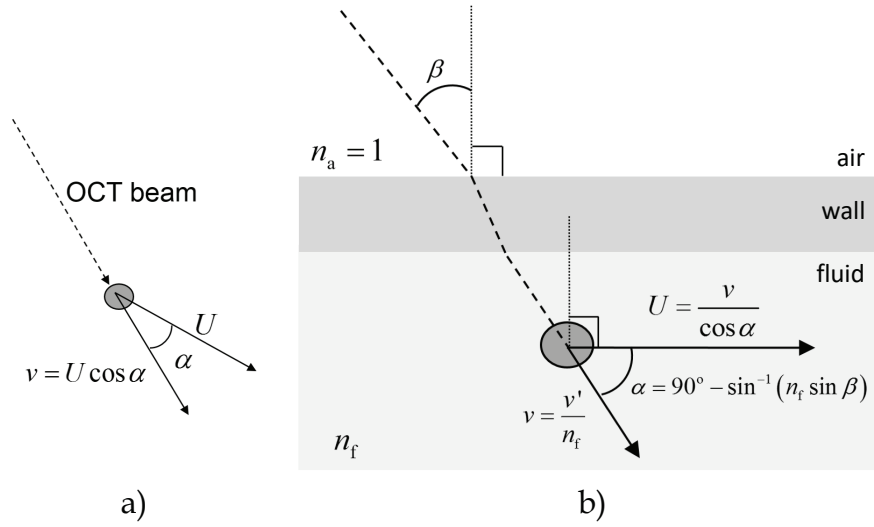
Figure 11   a) The DOCT measurement gives a single velocity component v of the velocity vector U in the direction of the OCT beam. b) Refraction of the OCT beam at e.g. pipe wall. Here, U is the real velocity, v is the component of velocity in the direction of the measurement beam, v' is the velocity value given by the DOCT device and is the refractive index of the medium. The angle α is obtained by applying the Snell's law of refraction on the two interfaces.

For unambiguous velocity determination, the phase shift has to be confined to $[-\pi, \pi]$. The Nyquist theorem dictates that the theoretical maximum quantifiable velocity in the direction of the OCT light beam is thus

$$v_{\text{max}} = \frac{\lambda f_A}{4n \cos \alpha}. \tag{3.14}$$

The maximum measurable velocity can be increased by decreasing the measurement angle between the OCT light beam and the velocity vector (Leitgeb et al. 2014).

In a DOCT measurement, the phase shift $\Delta\varphi$ in Equation 3.12 is usually a temporal average of instantaneous phase shifts acquired for better signal-to-noise ratio and thus higher sensitivity of velocity. Due to the inherent noise and possible velocity fluctuations, several observations of the phase shift, in fact result in a distribution of phase shifts (Figure 12a and b). The average can be calculated either by averaging directly over the phase shift histogram or preferably by fitting a Gaussian distribution to it. If the average velocity is, however, close to the maximum detectable velocity value, the distribution values close to π become wrapped by -2π and appear partly as negative phase shifts resulting in incorrect velocity values. In such case (see Figure 12c), unwrapping procedures can be applied to correct for the histogram aliasing at large phase shifts (Ghiglia & Pritt 1998, Werkmeister et al. 2012). Detailed analysis of the wrapping of the phase shift histograms can be found in (Szkulmowska et al. 2008). Phase unwrapping enables the measurement of velocities exceeding the theoretical maximum velocity given by Equation 3.20. It is an essential process in the accurate reconstruction of the phase shift (velocity) profiles. Various methods for improving the accuracy of the DOCT phase unwrapping have been discussed in (Xia et al. 2017).
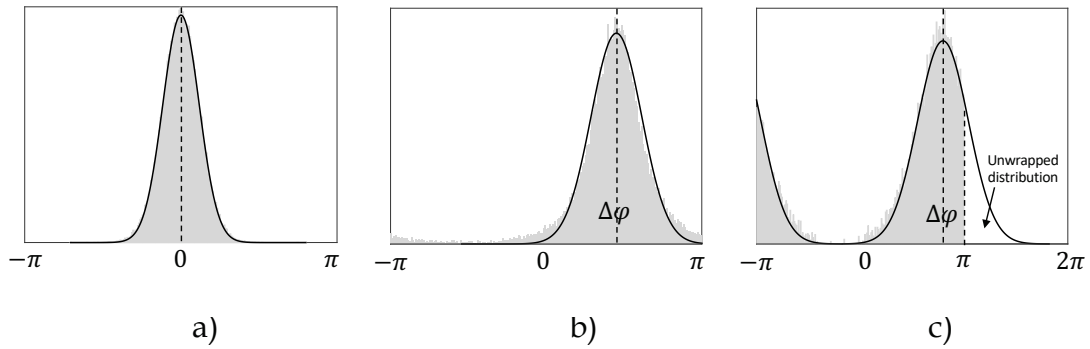
Figure 12   Histogram of phase shifts for a) stationary objects, b) moving objects inducing Doppler shift, and c) moving objects inducing Doppler shifts greater than π. In c), the distribution has to be unwrapped to enable correct phase difference averaging. The solid lines in a)-c) represent Gaussian fits to the distributions.

If the OCT light beam is perpendicular to the moving object, a Doppler shift is not induced. In addition to using multiple OCT beams (Pedersen et al. 2007, Werkmeister et al. 2012, Kumar et al. 2014, Trasischker et al. 2013), methods for measuring flow velocities perpendicular to the light beam have been proposed. Often, these methods utilize the Doppler variance and the broadening of the power spectrum (Ren et al. 2002, Proskurin, He & Wang 2003, Piao & Zhu 2003, Wu 2004).

In many industrially relevant flow geometries, such as pipes or rheometer geometries, the average flow direction is known a priori. In such cases, the absolute values of the velocity vectors can be obtained quantitatively. The schematic in Figure 11b applies for pipe flow the darker part corresponding to an optically transparent pipe wall. The real axial velocity in the pipe is

$$U = \frac{v'}{n_f^2 \sin \beta},$$

(3.15)

where β is the DOCT measurement angle (the angle between the OCT beam axis and pipe surface normal), v' is the velocity value given by the DOCT device, and n_f is the refractive index of the monitored medium. Notice that similar reasoning also applies e.g. for plate-plate and concentric cylinder rheometer geometries. In this case, the local shear stress is obtained from the torque measurement of the rheometer. In the cases where one velocity component of the flow is enough for meaningful flow analysis, velocity profiling with DOCT is often carried out in M-mode. In the M-mode, sequential axial A-scans are recorded over a certain time period in a single physical position instead of 2D scanning, which enables observation of faster transients and better signal-to-noise ratio upon data averaging (Drexler & Fujimoto 2008).

4   MATERIALS AND EXPERIMENTAL TECHNIQUES

4.1 Materials

The microfibrillated celluloses used in this work were prepared from wood pulps by mechanical disintegration. The microfibrillated cellulose mainly used for the experiments with the rotational rheometer was prepared from never-dried, bleached kraft birch pulp (obtained from UPM-Kymmene Corporation) by grinding with a supermasscolloider (Masuko Sangyo; Kawaguchi, Japan) for three passes. Before grinding, the pulp was changed to its sodium form and washed with deionized water until the electrical conductivity was less than 20 μS/cm, according to a procedure introduced by Swerin et al. (Swerin, Ödberg & Lindström 1990). The properties of the raw material of similar MFC have been reported in the literature (Eronen et al. 2011). Corresponding MFC grades have been reported to have a very wide size distribution. The values of diameter range from 10 nm to a few micrometers (Vartiainen et al. 2011). The suspensions for the rheological experiments were obtained by diluting the ground MFC with MilliQ water. After adding the water, the suspension was mixed with an overhead stirrer equipped with a propeller (Heidolph Instruments, Germany) using a speed of 1400 rpm for 10 minutes. This MFC will be referred to as fine grade MFC.

The microfibrillated cellulose used in the experiments with the pipe rheometer was obtained from Daicel Chemical Industries, Japan. The product type was Celish KY-100G, which is manufactured from purified wood pulp. The basic properties of this commercial MFC have been reported in the literature (Tatsumi, Ishioka & Matsumoto 2002). The average length and diameter of the fibers are 350 μm and 15 μm, respectively. The size distribution of the fibers, however, ranges from microscale to nanoscale. In another words, this rather coarse grade of MFC consists of cellulosic fibers that are nearly their original size but have a very high level of fibrillation.

The final MFC suspensions used in the experiments were obtained by diluting the original MFC by water. The prepared suspensions were firstly soaked for several hours and then mixed with an overhead stirrer equipped with a propeller (Setup A: Heidolph Instruments, Germany; Setup B: Precision Stirrer, Glas-

Col, LLC) for 30 minutes. The mass concentrations of the prepared suspensions were measured with a Halogen Mettler-Toledo Moisture Analyzer. This MFC will be referred to as coarse grade MFC.

4.2 Velocity profiling techniques

4.2.1 Optical coherence tomography

The OCT device adopted in this thesis was a Telesto I Spectral Domain OCT (Thorlabs, Inc.) with a central wavelength of $\lambda = 1325$ nm and a broad bandwidth in excess of 100 nm. This light source provides an axial resolution of approximately 5 μm in air and ca. 3.7 μm in water. The maximum pixel amount of 512 per A-scan provides an imaging depth of up to 1.9 mm in water. The lateral resolution of the system optics is 15 μm.

The A-scan rate in the device can have three discrete values, 5.5, 28 or 91 kHz. Thus, in the DOCT mode, the theoretical maximum for the detectable velocity in the beam direction ($\alpha = 0°$) is 3.1 cm/s. As the Doppler angle in the experiments presented in this thesis varied between $2° - 5°$, the maximum measurable velocities were between 0.2 – 0.5 m/s in water ($n = 1.33$). The Doppler angle was determined from B-scan images composed of 4096 A-scans in a lateral range of 2.00 – 5.00 mm. The uncertainty of the angle in the image was evaluated to be $0.2° - 0.5°$ depending on the image quality. Thus, the error in various velocity measurements was estimated to vary between 0.8% and 4.5%.

For velocity profiling in the DOCT mode, a small amount of low-fat milk or powdered coffee creamer was added as light scattering tracer in the suspension to ensure appropriate level of signal also from the regions of fluid between MFC aggregates. Due to their size and good dispersibility, the fat droplets in the milk and the creamer are expected to follow the flow faithfully (Kirk & Othmer 2008). The added amounts of the tracer varied between 0.5 – 1.2% by volume. The amount was adjusted to find an optimal balance between the DOCT signal intensity and its penetration depth.

The OCT was connected to a master PC for control and data acquisition with system software version 3.2 (Thorlabs). In this software version, the Doppler frequency shifts are calculated based on spatially averaging phase shifts, using a sliding 2D window together with a Kasai autocorrelation function (Kasai et al. 1985). The conversion of the phase shift information to velocity had to be carried out offline. Thus, a Matlab routine was developed to extract the velocity information from the recorded phase shift data. In this routine, the mean phase shift at each depth is determined by a Gaussian fit to the histogram. Furthermore, a histogram unwrapping procedure was implemented in the code. Examples of the phase shift histograms and Gaussian fits are, in fact, presented in Figure 12.

4.2.2   Ultrasound velocity profiling

Within this study, a commercial ultrasound velocity profiler DOP2000 manufactured by Signal-Processing S.A, Switzerland, was used. The software version installed in the instrument was 4.06.1. In DOP2000, the velocity measurement algorithm is based on computing the auto-correlation of the Doppler echoes followed by calculation of the velocity using Equation 3.6.

An ultrasound probe with 8 MHz frequency and 5 mm active piezo element with a beam divergence of 1.20° was installed in a water bath surrounding the pipe in both pipe rheometer setups (see section 4.4). A photograph showing the probe setup can be found in Figure 14. The approximate value of the Doppler angle for the UVP measurement was determined manually by measuring the setting angle between the tube upper surface and the body of the US probe. The probe setting angle was in the range of $11.5° - 16.0°$. The actual Doppler angle and the spatial coordinate of the profiles were evaluated by taking into account the ultrasound refraction and the ultrasound speed difference in different medias according to theoretical correction reported in (Wang et al. 2003). Sound speed values of 1500 m/s and 3962 m/s were used for the water and the pipe glass material, respectively. The relative error of the velocity measurements due to the error in the angle was approximated to be ~10 – 15%.

The ultrasound pulse repetition frequency was varied between 500 Hz and 2000 Hz in order to exploit the full velocity resolution range, given the 8-bit dynamics of the used instrument. The number of consecutive pulse emissions used to calculate a single velocity value in each sampled depth locations was either 8 or 32. The time for recording a single velocity profile varied approximately between 15 ms and 100 ms based on the pulse repetition frequency and the time needed to transfer the measured data from the ultrasonic processor to the internal memory. The length of a single ultrasound pulse N was set to 2 cycles, corresponding to a pulse length of approximately 0.38 mm ($h = 0.19$ mm, see Equation 3.10) in water at temperature of 22 °C. Such short pulses were observed to give the best results in the near-wall region with high velocity gradients.

4.3   Rotational rheometer

4.3.1   Flow curve measurements

In this study, a dynamic rotational rheometer (AR-G2, TA Instruments; New Castle, DE, USA) was used with concentric cylinder geometry. A standard hard-anodized aluminum cylinder with radius of 14.00 mm and height of 42.00 mm was used, but the standard outer geometry was replaced by a custom-made transparent polymethyl methacrylate (PMMA) cup, which enabled optical access in the rheometer gap. The radius of the cup was 14.9 mm, and it was placed into a transparent water container. The temperature in the container was not controlled, but it was assumed to be at room temperature, i.e. 23°C – 25°C.

Flow curves were measured as strain controlled stepped flow shear measurements with descending apparent shear rates in the range of 600 s^{-1} to 0.1 s^{-1}. In the stepped flow case, the duration of each applied apparent shear rate was 15 s. The reported values were calculated as the average of the last 5 s. Prior to the measurements, the suspension structure was first homogenized with a pre-shear interval of 20 minutes at an apparent shear rate ($\dot{\gamma}$) of 500 s^{-1}, and then left to recover for 10 minutes under small amplitude oscillatory shear (angular frequency 6.28 rad/s, strain 0.5%, i.e. well within the linear viscoelastic region). The intensive pre-shear period was implemented to break down the flocculated MFC network structure and to ensure similar shearing history for all samples. Stopping the flow after the pre-shear interval allows the MFC network to relax after straining in the shear.

4.3.2 Image analysis and velocity profiling

Two different approaches were used to characterize the MFC suspension structure and flow during the rheometer measurements. In the first case, the OCT device (see section 4.2.1) was set to acquire B-scans including 500 radial scans across a lateral width of 1 mm. Results acquired using this approach are denoted with the acronym OCT.

A schematic of the measurement setup with rheometer is shown in Figure 13. The A-scan rate (either 5.5, 28 or 91 kHz) was selected based on the shear rate. The aim was to minimize the motion of the MFC structures between two sequential slice images while keeping the image quality as good as possible. At the highest A-scan rate, a mean frame rate of 12 ms was achieved, but the intensity of the light signal was clearly reduced near the rotating cylinder.

A sequence of B-scans was recorded at each shear rate (or oscillation strain). In addition to structural characterization, the images were utilized to determine the radial mean velocity profile by tracking the horizontal displacement of the MFC flocs between sequential images. The tracking was realized with an image correlation algorithm developed for fiber flocculation studies (Salmela & Kataja 2005). The maximum A-scan rate and the imaging parameters allowed structure motion to be tracked over shear rates from 0.1 to ca. 50 s^{-1} in the vicinity of the outer cylinder wall. However, the velocity profiles could be extracted from the OCT data in the shear rate range of 0.1 - 15 s^{-1}, and the maximum depth of the profiles was limited by the reduced intensity of the light signal. Notice that in this approach, additional light scattering tracer was not used and hence the data given by the image correlation algorithm represents the velocity of the MFC phase.

In the second approach, the Doppler extension of the OCT device was utilized in M-mode where sequential axial A-scans were recorded in a single physical position instead of 2D scanning. Light scattering tracer was added in the suspension to ensure appropriate level of signal also from the regions of fluid between MFC aggregates. Thus, the velocity data obtained in the DOCT mode represents both MFC and fluid phase. By using the M-mode the velocity profiles could be determined across the whole gap with all the studied shear rates. The Doppler angle for calculating the streamwise velocity component was determined from B-scan images composed of 1000 A-scans in a lateral range of 2.00 mm.
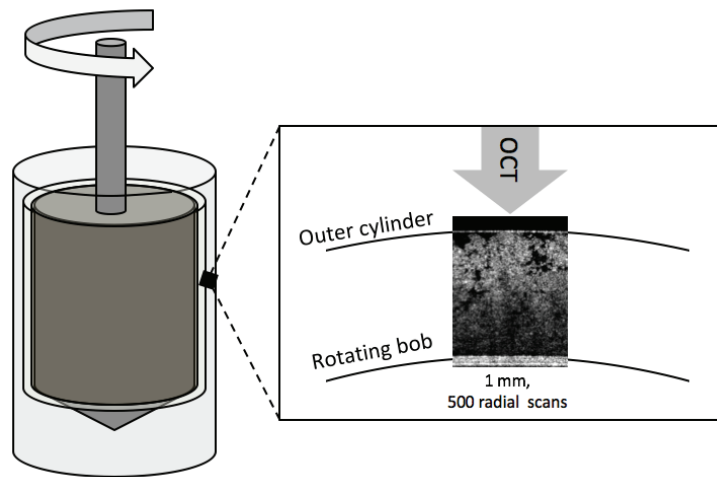
Figure 13   Schematic illustration of the experimental setup with concentric cylinder geometry equipped with the OCT device (Papers II-III).

4.4   Pipe rheometer

4.4.1   Experimental setups

In this study, two different pipe rheometer setups, denoted here as setup A and setup B were used. The measurement unit in the setup A, shown in Figure 14, consisted of a 1500 mm long and 8.6 mm inner diameter optical grade glass tube. The flow was driven either by gravity or pressurized air to allow for a steady, pulsation-free flow. The suspension flow was controlled by the overpressure in the container, and by a manual valve installed after the glass tube. The highest applied overpressure was 1 bar. The total mass flow rate was recorded with a computer-controlled laboratory scale (Sartorius TE3102S). The wall shear stress at each mass flow rate was determined based on pressure difference measurement between two 1.5 mm diameter taps drilled through the pipe wall 1000 mm apart, the first measurement location being 52 pipe diameters from the inlet. The pressure difference measurement was done using calibrated sensors (Rosemount, sensor types 3051 and 2051, Emerson Electric Company, St. Louis, MO). The experiments were performed at the room temperature of 22 degrees Celsius.

The measurement unit in the setup B consisted of a 2.5 m long optical grade glass pipe with an inner diameter of 19 mm. A schematic illustration of the setup is shown in Figure 15. The flow in the pipe was driven using a low-pulsation progressive cavity pump (Seepex MD series). Total volume of the sample in the flow loop and in the tank was 13.5 liters. The fluid temperature in the loop was set to 22 °C with a digital temperature controller (PolyScience, model 9610). The fluid temperature in the tank was additionally measured manually with type K thermocouple. The flow rate in the setup B was measured with a magnetic flow meter (Siemens, Sitrans F M MAGFLO). The wall shear stress at each flow rate

was measured with the same pressure sensors than in the setup A. The pressure measurement taps were located at 74 and 126 diameters downstream from the pipe inlet.
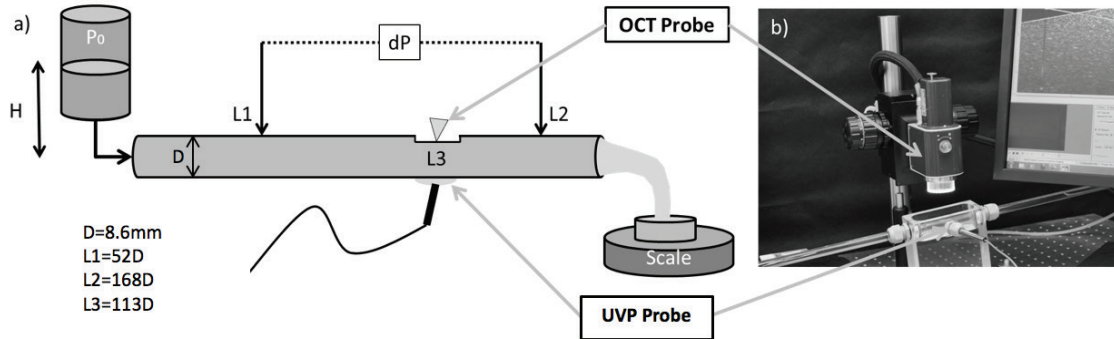

Figure 14   a) Schematic illustration of the experimental setup A with simultaneous DOCT and UVP measurement of velocity profiles in a straight glass tube of inner diameter 8.6 mm and length 1.5 m. b) Photograph of the OCT probe and the UVP probe installed in the water bath surrounding the glass tube. This setup was utilized in Paper I and Paper III.

For the DOCT measurements, a flat region was machined on the outer surface of the both pipes, to minimize the glass thickness and to prevent undesired refraction of light at the measurement point. The DOCT measurement locations in the setup A and B were 113 and 116 diameters from the pipe inlet, respectively. With DOCT, stationary state velocity profiles at each constant value of flow rate were obtained based on the phase shift data. Slightly different procedures were used in the experiments reported in different papers. In papers I and III (setup A), the velocity data was acquired from B-scans consisting of 1000 A-scans equaling a physical width of 1.00 mm. For each flow rate 200 B-scans were recorded. In paper IV (setup B), a series of 15 x 4096 A-scans were recorded in a single physical location for each flow rate. In the both cases, the A-scan rate was selected depending on the flow rate.

The UVP measurements in the setup A and B were performed 113 and 105 diameters from the pipe inlet, respectively. Stationary state velocity profiles at each constant value of flow rate were obtained based on a series of recorded velocity profiles. Due to limited available measurement time in the setup A, 150 – 500 individual velocity profiles could be recorded for the same flow rate before the container was emptied. In the case of the setup B, a series of 5000 velocity profiles was recorded for each flow rate.
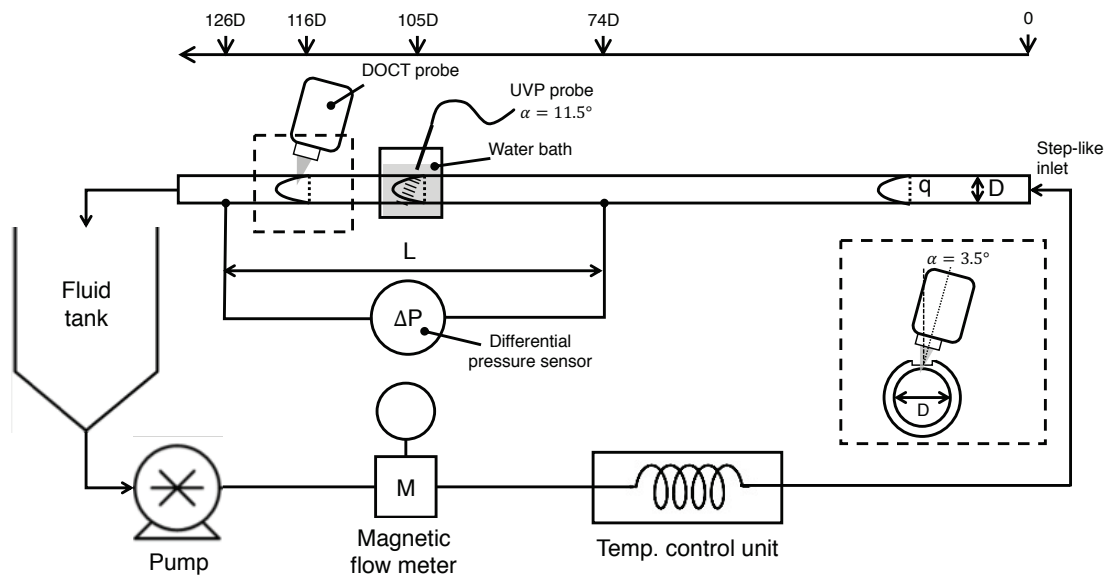
Figure 15   Schematic illustration of the experimental setup B with simultaneous DOCT, and UVP measurement of velocity profiles in a straight glass tube of inner diameter 19 mm and length 2.5 mm. This setup was utilized in Paper IV.

4.4.2   Hybrid multi-scale velocimetry

In this work, hybrid multi-scale velocimetry was used to study flows of complex fluids in a straight tube. The data from the OCT and UVP was combined into a comprehensive velocity profile including information on both the boundary layer near the wall and the interior parts of the flow, as shown schematically in Figure 16. The spatial resolution of DOCT is generally an order of magnitude better than that of UVP. On the other hand, the expected penetration depth of the OCT signal is less than a millimeter for MFC suspensions. The attenuation of the OCT amplitude signal (local scattering indices) is demonstrated in Figure 17a for three different concentrations of MFC suspension. While the increasing concentration decreases the accurate measurement range of DOCT, the deterioration of the velocity measurement is not quite as dramatic compared to the amplitude signal. Notice that the amplification of the signal has been tuned separately for each concentration, in order to optimize the quality of the velocity signal. Thus, the signals for the different concentrations are not directly comparable.
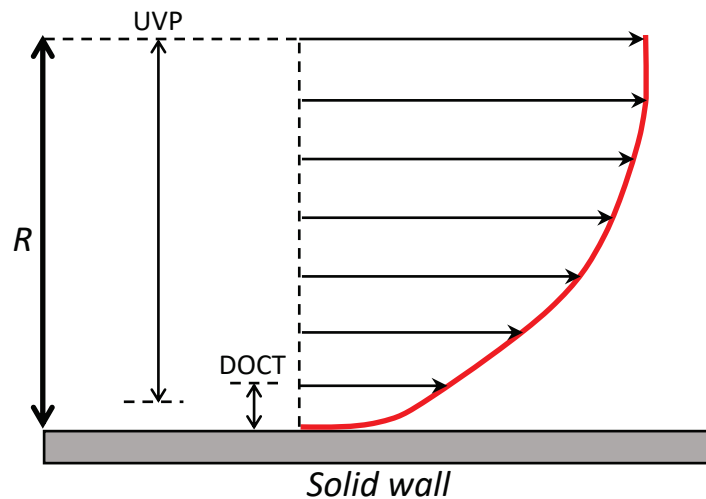
Figure 16   Schematic of the range of applicability of DOCT and UVP for measuring veloc-
ity profile in the tube flow. UVP is capable of measuring the velocity profile
across the whole tube radius excluding the immediate vicinity ($\lesssim$ 0.5 mm) of
the wall. The high resolution DOCT provides velocity profiles near the trans-
parent tube wall, typically up to 1 mm from the wall.

Although measured simultaneously, the compatibility of the mean velocity pro-
files acquired by the different measurement techniques, within their overlapping
portion of valid measurement range, is not necessarily complete. Firstly, simul-
taneous measurements cannot be performed at exactly the same physical location
due to physical size and installation requirements of the different instruments.
Secondly, systematic uncertainties related to the absolute velocity values inher-
ent in the different measurement methods have to be taken into account. System-
atic deviation may occur e.g. due to the uncertainty of the used values of the
Doppler angle.

        A procedure of normalization and matching was applied to help in elimi-
nating the systematic uncertainties related to the absolute velocity values and the
different measurement locations. Appropriate matching in the overlap region
was achieved by fine-tuning the Doppler angle of the measured UVP profile (see
Equation 3.6). Such correction retains the shape of the velocity profiles. If needed,
the UVP profile was further corrected for the spatial coordinate based on the
DOCT measurement. The combined velocity profile was normalized to match
with the flow rate measured independently by the magnetic flow rate sensor.
Typically, the corrections to the measured UVP Doppler angle required for pro-
file matching and to the overall flow rate normalization, were below 0.3° and 10%,
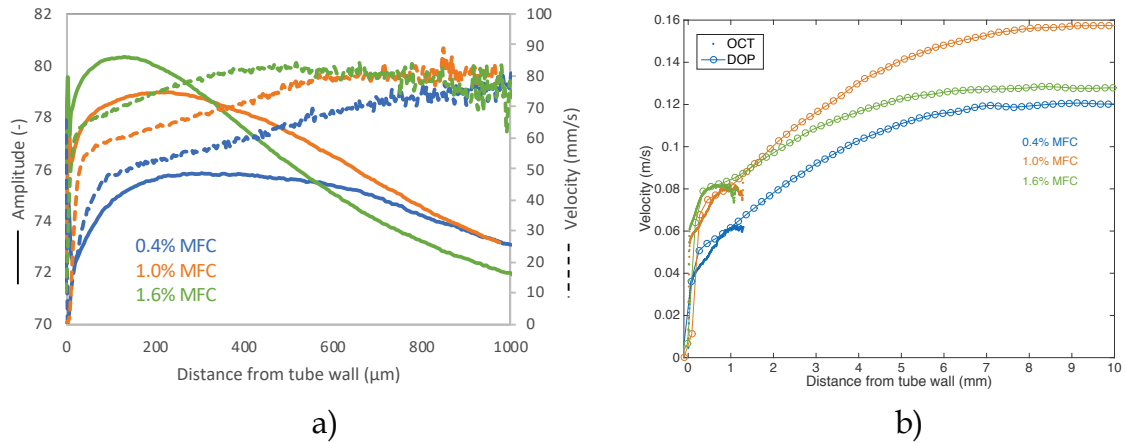respectively.

Figure 17   a) Examples of mean DOCT velocity profiles (dashed lines) together with the corresponding logarithmic amplitude signals (solid lines) for three MFC concentrations. The values of the amplitude signal represent the mean of the optical back-scattering index at each depth. The amplification of the signal has been tuned separately for each concentration in order to optimize the quality of the velocity signal. b) Examples of mean DOCT (dots) and UVP (circles) velocity profiles after normalization and matching. The colors to different profiles correspond to the suspension concentration.

Figure 17b provides examples of the matching with three MFC concentrations. Indeed, the velocity profiles measured by the DOCT in the near wall region and by the UVP in the interior parts of the tube show overlapping region of mutually consistent results. Typically, such overlap region is found within distance of 0.5 – 1.0 mm from the tube wall. The UVP data could be extracted down to approximately 0.1 mm from the wall but very close to the wall the velocity profiles appear to suffer from distortions caused by the averaging effects across the finite measurement sample volume in the flowing fluid. Instead of applying correction procedures in the near-wall UVP data, the DOCT data is used for velocity profile at this near-wall region.

The penetration depth of the DOCT is heavily dependent on the concentration of the MFC suspension. At greater distances from the wall (see Figure 17a), poor signal-to-noise ratios and aliasing lead to noisy velocity profiles that tend to turn downwards and must be omitted from the data analysis. If the amplitude of the light signal is reduced too much, the regions of accurate measurement of the DOCT and UVP may not overlap. In such case, a plausible estimation of the entire velocity profile may be obtained by extrapolating the DOCT data between the valid measurement domains of the two methods using a suitable fitting function. In addition to Papers III and IV, supporting information about the hybrid multi-scale velocimetry including measurements with rheologically different fluids as well as velocity profiling data with nuclear magnetic resonance imaging can be found in References (Haavisto et al. 2013, Haavisto et al. 2017).

5   RESULTS AND DISCUSSION

The first part of this chapter discusses the suitability of DOCT to study boundary layer flows and their rheology in tube flow (Paper I). In the second part, rheological properties and boundary layer behavior of aqueous microfibrillated cellulose (MFC) suspensions are explored by means of velocity profiling rheometry (Papers II – IV). The aim is to characterize the shear rheology of MFC suspensions and to describe the spatial flow inhomogeneities encountered in viscometric flows. In addition to velocity profiling, the imaging modality of the OCT is utilized in characterizing the structure of MFC suspensions in the near-wall region of tube flow and in the rheometer gap. The results are used to review the potential microstructural origin of the observed flow behavior and rheological response of MFC suspensions.

5.1   Measurement of boundary layer flows using DOCT

Before discussing the results obtained for the complex MFC suspensions, we study the capability of the DOCT adopted in these experiments to provide flow velocity profiles in the vicinity of wall of a circular tube with a diameter of 8.6 mm. After all, usefulness of DOCT velocity measurements has earlier been demonstrated for pressure-driven flows mostly in microchannels and in thin capillaries where the measurement depth of DOCT spans across the whole channel (Proskurin et al. 2003, Bukowska et al. 2013, Lauri et. al. 2015).

As test cases, laminar and turbulent flows of water in a straight pipe with smooth walls is used. The velocity profiles were obtained by DOCT in the near-wall region of the glass tube in the setup A. The fluid was tap water seeded with 1.2% by volume of milk (2% fat content) as a light scattering tracer, which increased the viscosity of water approximately by 1% (Bakshi & Smith 1984) . In Figure 18, shown are mean velocity profiles measured by DOCT in laminar (Re=460) and turbulent flow (Re=3200) regimes, respectively. For turbulent flow, the velocity profile is given in terms of the dimensionless distance $y^+ = u^* y/\nu$, and dimensionless flow velocity $u^+ = u/u^*$ (White 2003). Here, y is the distance from the wall, $u^* =$

$\sqrt{\tau_w/\rho}$ is the friction velocity, and τ_w [Pa] is the wall shear stress obtained from the measured pressure loss (Equation 3.3). Furthermore, ν and ρ [kg/m^3] are the kinematic and dynamic viscosities of the water, respectively. As seen in Figure 18, there is an excellent agreement between the two DOCT datasets and the theoretical velocity profiles determined based on an independently measured total volume flow rate. In turbulent flow, the DOCT data follow the linear law of the wall ($u^+ = y^+$) for approximately two orders of magnitude for $10^{-1} \lesssim y^+ \lesssim 10^1$. Further validation results with turbulent flow of water are presented in (Haavisto et al. 2017) and (Salmela et al. 2013). In the best case, the measurement range of the DOCT was almost three orders ($\sim 10^{-2} - 10^0$) of magnitude in y^+ for turbulent flow of water in a tube with a diameter of 19 mm, (Haavisto et al. 2017). Compared to some common techniques, DOCT is able to provide the velocity profile very close to the wall. In the same flow setup, the lower end of the practical measurement range of MRI was restricted to y^+ values of 1 – 2 with water. With PIV (Takeuchi et al. 2005) and UVP (Nowak 2002), the corresponding values have reported to be approximately $y^+ \gtrsim 0.1$ and $y^+ \gtrsim 1$, respectively.

a)   b)
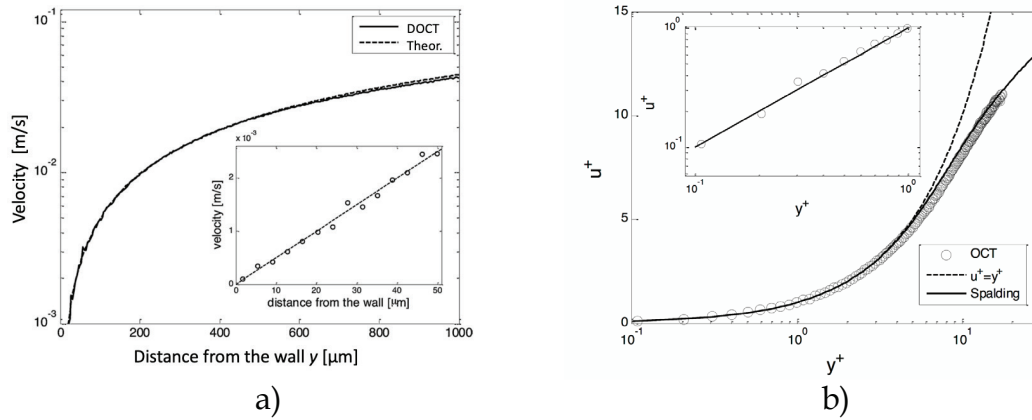
Figure 18   DOCT mean velocity profiles based on an ensemble of 50000 A-scans for tap water. In a), shown are the laminar velocity profile (Re = 460) (solid line) and the corresponding theoretical laminar profile (dashed line) based on an independent flow rate measurement. In b), shown is the turbulent velocity profile (Re = 3200) in dimensionless variables y^+ and u^+. The dashed line indicates the theoretical viscous sublayer profile, and the solid line represents the Spalding inner layer correlation (Spalding 1961). Notice that for the shown Re, the dimensionless distance $y^+ = 20$ corresponds to 650 μm (Paper I).

The high-resolution near-wall velocity data provided by the DOCT also allows accurate estimates of the local wall shear stress τ_w [Pa]. Provided that the fluid viscosity is known, $\tau_{w(\text{DOCT})}$ can be evaluated using the mean velocity gradient calculated from the near-wall DOCT data as $\dot{\gamma}_{w(\text{DOCT})} = \left.\frac{du}{dy}\right|_{y \sim 0}$ [s^{-1}] (Equation 3.1) and using Equation 3.3. Here, the subscript DOCT means that the corresponding quantity has been acquired using the DOCT data. In practice, $\dot{\gamma}_{w(\text{DOCT})}$ can be obtained, e.g., by fitting a second order polynomial to the velocity data in the immediate vicinity of the wall and calculating its derivative at $y = 0$. The wall shear stress, in turn, can be correlated with flow conditions in the tube by

the dimensionless Darcy friction factor (White 2003). The Darcy friction factor based on the DOCT measurement is

$$f_{\text{DOCT}} = \frac{8\tau_{w(\text{DOCT})}}{\rho U^2} .$$ (5.1)

Notice that velocity U has been acquired from the independently measured flow rate.

Another approach for utilizing the DOCT data is to evaluate the fluid viscosity at the tube wall. In this case, the wall shear stress is determined from the pressure loss measurement (Equation 3.3). According to Equation 3.4, the viscosity at $y = 0$ is then

$$\mu_{w(\text{DOCT})} = \frac{\Delta PR}{2L\dot{\gamma}_{w(\text{DOCT})}} .$$ (5.2)
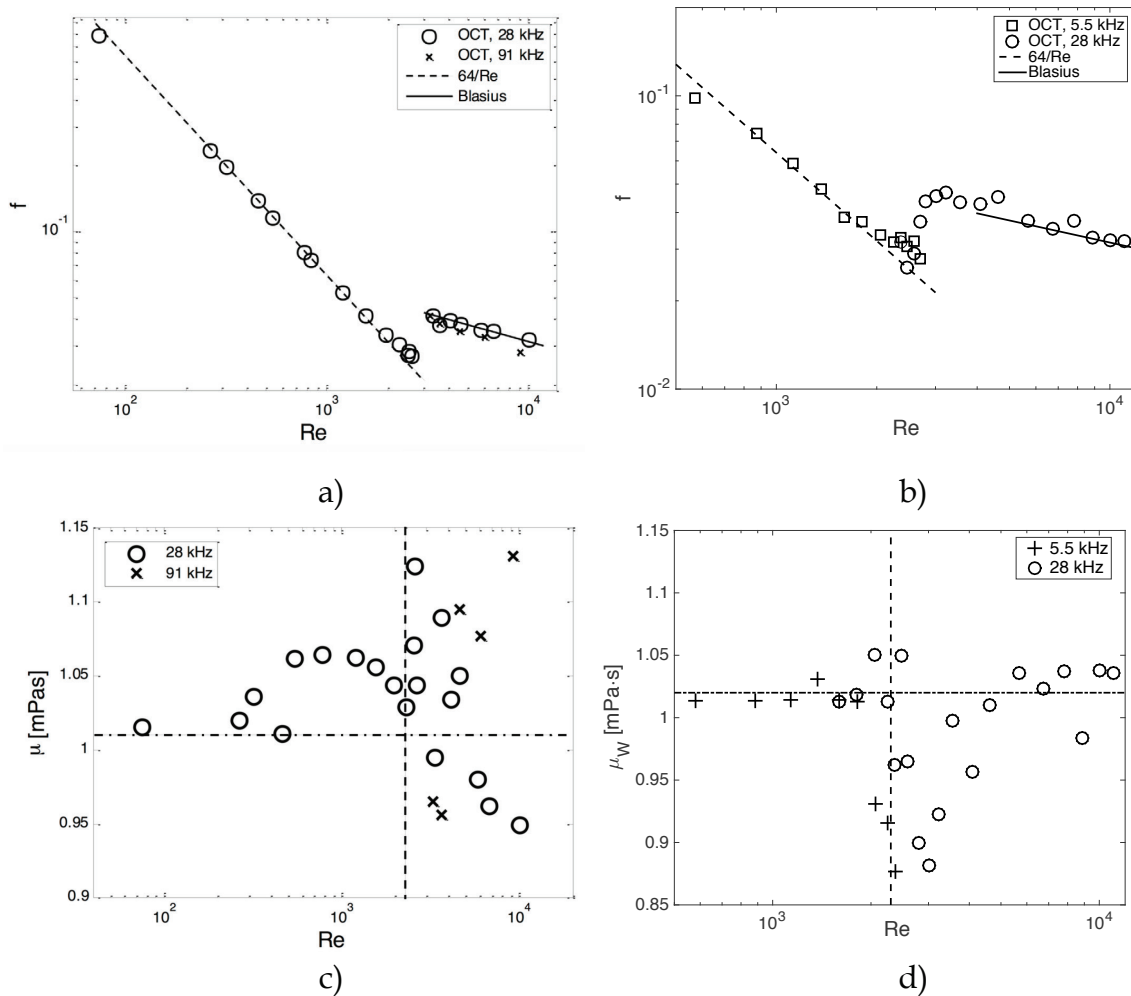
Figure 19   Friction factor for the pipe flow measured with DOCT in a) setup A (Paper I) and b) setup B (unpublished). The different A-scan frequencies are shown with different symbols. Friction factor based on an independent flow rate measurement is shown for the laminar (dashed line) and turbulent regions (solid line). The equations for the friction factor are $f = 64/\text{Re}$ (laminar flow), and $f = 0.316\text{Re}^{-1/4}$ (Blasius equation for turbulent flow). Viscosity of water measured using a combination of pressure loss measurement and DOCT in c) setup A (paper I) and d) setup B (unpublished). The dash-dotted line shows the evaluated viscosity of water and the seeding (milk fat) particles. The dashed line shows the onset point of turbulence at Re~2300.

Figure 19 presents examples of friction factor f_{DOCT} and viscosity $\mu_{w(\text{DOCT})}$ for water with a Reynolds number range 50 – 10000. The measured data from the both setups A and B is shown. In the laminar region, the friction factor given by the DOCT data follows closely to the theoretical value ($f = 64/\text{Re}$) determined based on the independently measured flow rate. The agreement with the semi-empirical Blasius equation in the turbulent region is also good (White 2003). The discrepancy with the A-scan frequency of 91 kHz is larger due to decreased sensitivity of the measurement with increasing A-scan rates.

Considering the low viscosity of the water, the accuracy of the viscosity values obtained from the DOCT data is very good in the laminar region. Remarkably, reasonable values are obtained also in the turbulent region Re > 2300. It is noteworthy that the Doppler angle has been determined by the image analysis, without fine-tuning it with the measured flow rate or pressure loss verifying that DOCT can be used for quantitative velocity measurements and rheological analysis even though the measurement depth of DOCT does not span over the whole flow geometry. Altogether, the presented measurement setups appear reliable and convenient for measuring the fluid viscosity in a wide range of pipe flow conditions without a need of extensive calibration of DOCT.

5.2 Characterization of MFC suspension flow and rheology

5.2.1 Rotational rheometer

A combination of rotational rheometry and image analysis as well as visual observations were utilized to study the flow behavior and heterogeneous structure of MFC suspensions. The objective was to follow the changes in structure of the suspensions inside the rheometer gap during rheological measurement and observe complex behavior that can interfere with results obtained with conventional rotational rheometers. The aim of the latter part of this section is to bring more insight in interpreting the flow curves of MFC suspensions by means of OCT measurements using both structure imaging mode and Doppler OCT mode.

Figure 20 shows flow curves for fine grade MFC suspensions at concentrations of 0.5% and 1%, measured by a rotational rheometer. Assuming fibril diameter starting from 10 nm and length being up to over 1 μm, both concentrations of the fine grade MFC suspension are above the rigidity threshold, that is, where fiber flocs are coherent and able to bear mechanical load and the values of crowding factor are above 60 (Celzard, Fierro & Kerekes 2009). The yield stress values of the suspensions have been indicated in Figure 20b.

The well-known general shear-thinning behavior (Pääkkö et al. 2007, Agoda-Tandjawa et al. 2010, Iotti et al. 2011, Karppinen et al. 2012) of MFC suspensions is evident in all the presented cases. Differences are observed in the viscosity levels that are higher at increased concentration (Tatsumi, Ishioka & Matsumoto 2002, Pääkkö et al. 2007, Agoda-Tandjawa et al. 2010), and when a pre-shearing stage is introduced before the rheological measurements (Naderi & Lindström 2015), in line with earlier results.

As observed also by others, the flow curves of MFC suspensions consist of, typically three distinct regions showing different rheological dependencies (Pääkkö et al. 2007, Agoda-Tandjawa et al. 2010, Iotti et al. 2011, Lavoine et al. 2012, Karppinen et al. 2012). For the MFC suspensions studied here, the three different regions can also be distinguished. At low ($\dot{\gamma} \lesssim 2\,\text{s}^{-1}$) and high ($\dot{\gamma} \gtrsim 50\,\text{s}^{-1}$) shear rates, all the MFC suspensions exhibit power-law type shear-thinning behavior. An example of power-law fits to the different flow regions is shown in Figure 20a, and the values of the fitted parameters are given in Table 2. At the low shear rate region, the shear stress has fallen below yield stress and the flow indices of the power-law fits are very small indicating that the suspensions are not properly sheared. The parameters of the power-law fit at the high shear rate region are in line with the results obtained for similar type of fine grade MFC (Lauri et al. 2017) and coarse grade MFC (Haavisto et al. 2011) in pipe flow.
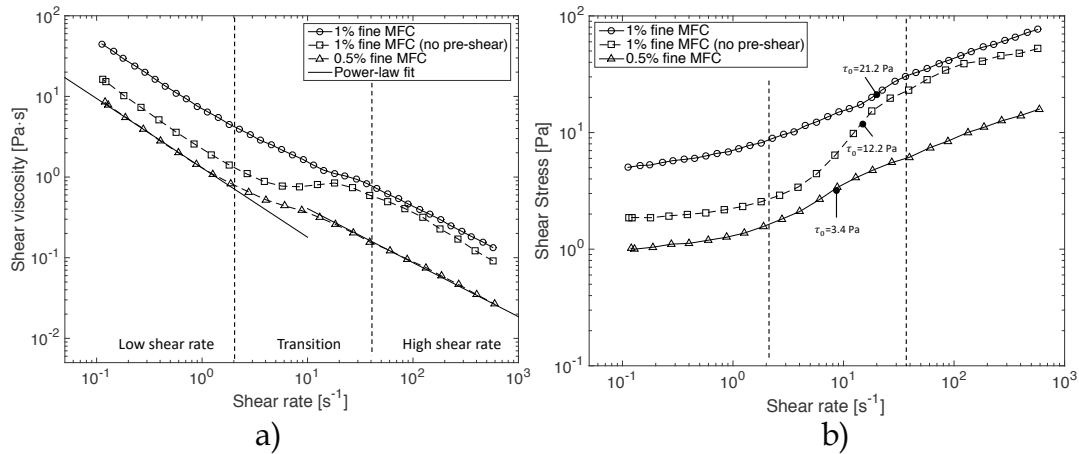
Figure 20   Apparent shear viscosity a) and shear stress b) as a function apparent shear rate for fine grade MFC suspension at concentrations of 0.5% and 1%, measured by a rotational rheometer (Papers II and III). The flow curve indicated by 'no pre-shear' was measured without applying pre-shearing (Paper II). The different shear rate regions as observed visually from OCT images have been indicated with dashed lines in the subfigures. Also, shown are an example of the power-law fits (see Table 2) in subfigure a), and the yield stress values τ_0 of the suspensions in Figure b).

At intermediate values of shear rate a transition occurs, and a characteristic kink or plateauing (Newtonian) region in the values of viscosity is found. The values of yield stress for different suspensions fall into the transition region, and a bent in the shear stress (and viscosity) may be observed in that location. Furthermore, the role of pre-shearing is demonstrated also in the transition region. The suspension at 1% concentration, measured without pre-shearing, shows pronounced transition as compared to the suspensions at concentrations of 0.5% and 1% that have undergone the pre-shearing stage.

Table 2   Properties of the fine grade MFC suspensions. The yield stresses have been measured using rotational rheometer equipped with vane geometry (Paper II and Paper III). Notice, that the yield stress value for the MFC without pre-shearing stage is indicative only, as it was determined using a different MFC batch.

MFC material	wt%	Yield stress [Pa]	Power-law fit, low shear rates		Power-law fit, high shear rates	
			K	n	K	n
Pre-sheared	0.5%	3.4	1.3	0.14	1.9	0.33
Pre-sheared	1.0%	21.8	7.3	0.19	9.4	0.33
No pre-shear	1.0%	12.2	2.3	0.11	11.3	0.24

The different regions in the MFC flow curves have been attributed to changes in suspension morphology and macroscopic flocculation by optical observations (Saarikoski et al. 2012, Karppinen et al. 2012). Subfigures a-c in Figure 21 shows photographs of flocculated structures in the case of 1% MFC suspension (without pre-shear) during the flow curve measurement that was carried out for decreasing shear rate. The photographs depict the three different regions observed in the flow curve, showing that at high shear rates, the flocs (indicated by light color) are small and the suspension appears rather homogeneous in macroscopic scale, that is, in the rheometer scale. In the transition region, the shear forces of the decelerating flow are not large enough to keep the flocs apart, and larger flocculated structures begin to form. The structure formed in the transition region remains uneven and heterogeneous when the shear rate is further decreased. In addition, long cylindrical structures (rollers) perpendicular to the direction of flow begin to form within the fiber network (see Figure 21c). The mechanisms of roller formation are discussed in more detail later in this chapter.
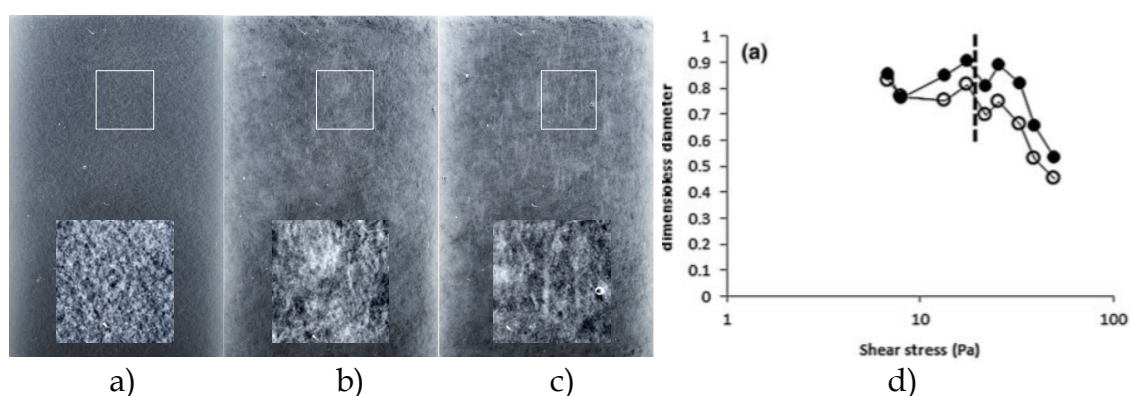
Figure 21   a)-c) Photographs of 1% fine grade MFC suspension (without pre-shear) in the rheometer gap at different shear rates: a) 108 s^{-1}, b) 11 s^{-1}, and c) 1 s^{-1}. The suspension was photographed through the transparent outer cylinder of the concentric cylinders' geometry. White rectangles show the areas of the magnified images. The size of the rectangle is 7x7 mm (Paper II). d) The average floc diameter along the shear (hollow symbols), and perpendicular to shear (filled symbols) for 1% fine grade MFC suspension (with pre-shear). The floc size has been scaled with the gap width (Paper III).

Comparable structural behavior is also seen with the pre-sheared MFC material. Figure 21d shows the average floc size up to the apparent shear rate of 100 s^{-1} as determined from the photographs according to the procedure described in (Saarikoski et al. 2012). Starting from the high shear rates and decreasing, the floc size relative to the gap size increases from 55 to 65 % and reaches a maximum of 80–90 % after the shear stress falls below the yield stress. Earlier it has been found that the flocculation behavior is similar for increasing shear rate, confirming that the continuous network of smaller flocs formed during the pre-shearing stage is replaced by larger flocculated structures in the transition region (Karppinen et al. 2012).

To further resolve the flow behavior leading to the observed flow-induced structural changes, the experimental setup was complemented with OCT measurement. In the next section, the different regions of the flow curve, identified above, are examined in more detail. While the photographs of the flocculated structures include information only from the outer surface of the rheometer gap only, OCT allows for the determination of floc structure and shear rate profile in radial direction across the gap.

5.2.1.1   High shear rate region (above yield stress)

The flow behavior of 1% MFC suspension (without pre-shear) at high apparent shear rates is illustrated in Figure 22. As visible in the structural DOCT data, the size of the flocs decreases with increasing shear rate, in accordance with (Karppinen et al. 2012, Saarikoski et al. 2012). When compared to the higher shear rates, the size of the flocculated structures is clearly increased in the image, corresponding to the shear rate of 73 s^{-1}, and there are larger areas of fiber-free water present.

Contrary to the linear velocity profile assumed in the rheometer data, the overall velocity profiles $u(y)$ shown in Figure 22 consist of regions that exhibit different shear rate behavior. The observed regions have been labeled with Arabic numbers 1-3. Near the stationary outer wall (region 1), the velocity profile is very steep and approaches rapidly zero in a region with a thickness of approximately 15 µm. Such extreme shear localization suggests that a water-rich depletion layer is formed at the wall. In the interior part of the gap, the velocity profile appears to include two regions (2 and 3) of slightly different shear rates. Adjacent to the apparent slip layer, at the distance range of 15 µm $\lesssim$ y $\lesssim$ 250 µm from the outer wall, shear rate is higher than in the middle of the gap. In both regions, the bulk of the suspension exhibits true shear flow (nearly linear velocity profile) where the shear rate is 55 – 70% smaller compared to the corresponding apparent shear rate given by the rheometer. In the vicinity of the moving wall y $\gtrsim$ 900 µm, the measured velocity profiles are distorted due to strong attenuation of the optical signal. The change in the slope of the velocity profile suggests that wall slip may be present also on the inner cylinder wall, but this could not be verified.
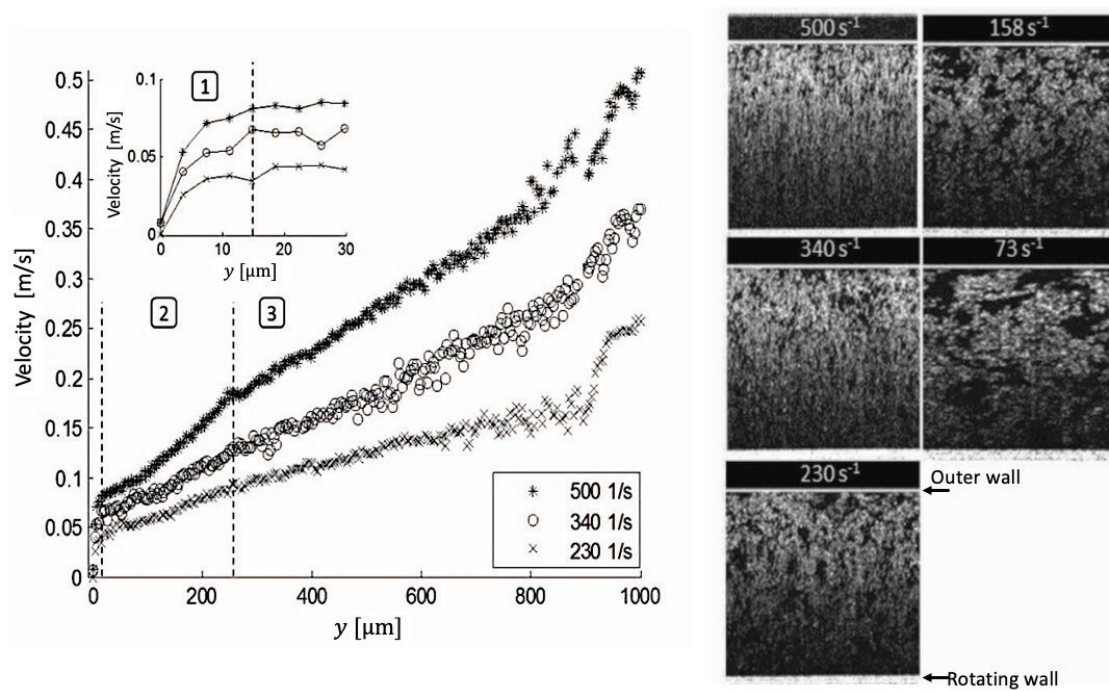
58

Figure 22   Velocity profiles $u(y)$ and structure images in the high shear rate region meas-
ured in DOCT mode for 1% MFC suspension flow inside a rotational rheome-
ter gap. The three different shear regions are labeled with Arabic numbers 1-3
and indicated with dashed lines. The structure images shown on right consist
of sequential A-scans imaged in M-mode. The labels to different images corre-
spond to the apparent shear rate. No pre-shearing was applied. (Paper II)

5.2.1.2   Regions of transition and low shear rate (below yield stress)

Figure 23 compares the structure and velocity of the MFC phase for three fine
grade MFC suspensions. In the images shown are the transition and low shear
rate regions of the flow curve. The highest shear rate is found near the point
where the shear stress falls below the yield stress. The two other images corre-
spond to shear rates where the shear stress is clearly smaller than the yield stress.
Figure 24, in turn, shows the relative slip velocity at the outer wall for the 0.5%
and 1% fine grade MFC suspensions that have undergone the pre-shearing stage.
The relative slip velocity is the slip velocity u_{slip} scaled by velocity of the inner
wall (see Figure 23b and e). Thus, a relative slip value of 1 means that the velocity
at the cup wall equals the velocity of the rotating cylinder. The yield stress of the
suspensions is also shown in Figure 24.

According to the OCT measurements, the structure and flow behavior of
the three suspensions show several different complex phenomena. Looking at
both the velocity profile and the relative slip velocity of the pre-sheared suspen-
sions (Figure 23a-f), the 1% fine grade MFC sample remains attached to the inner
wall, slipping along the outer wall, and the relative slip velocity is close to 1.

a) 0.5%, 12.3 s⁻¹, 4.3 Pa   b) 0.5%, 5.7 s⁻¹, 2.8 Pa   c) 0.5%, 0.6 s⁻¹, 1.4 Pa

d) 1%, 14.4 s⁻¹, 18.9 Pa   e) 1%, 5.7 s⁻¹, 12.9 Pa   f) 1%, 0.6 s⁻¹, 6.5 Pa

g) 1% (NOPRE), 10 s⁻¹, 0.8 Pa   h) 1% (NOPRE), 5.0 s⁻¹, 0.6 Pa   i) 1% (NOPRE), 1.0 s⁻¹, 0.4 Pa
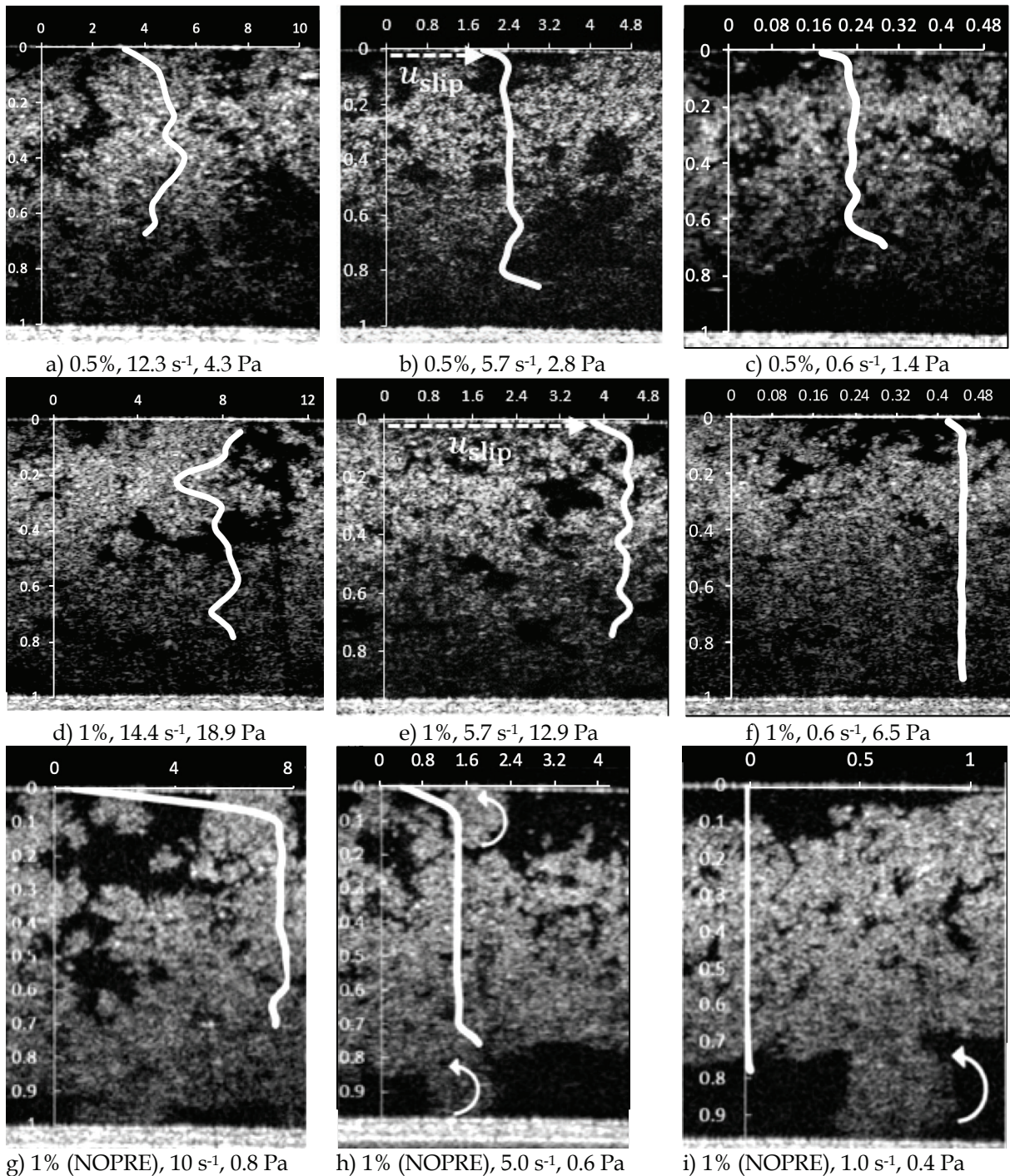
Figure 23   OCT B-scans overlaid with measured mean velocity profiles of the solid (MFC) component (white lines) at different apparent shear rates in stepped flow measurements: a)-c) 0.5% fine grade MFC suspension, d)-f) 1% fine grade MFC, and g)-i) 1% fine grade MFC without pre-shear (NOPRE). The captions to different images give the concentration, apparent shear rate, and shear stress. The vertical axis shows the position inside the gap, value 0 corresponding to the stationary outer wall, and value 1 corresponding to the moving inner wall, i.e. surface of the rotating cylinder. The horizontal axis shows the velocity in mm/s with the maximum value equal to the surface velocity of the inner wall. The velocity profiles were determined by using an image correlation algorithm described in (Salmela & Kataja 2005). In addition, rotational movement of rollers is shown with white arrows. (Papers II-III)

At apparent shear rates above yield stress, the relative slip velocity drops below 1 and remains approximately constant up to the maximum shear rate studied. Above its yield stress, also the 0.5% fine grade MFC suspension behaves in a similar manner to the 1% MFC suspension. However, below the yield stress the 0.5% sample is prone to slippage also at the inner wall. Although not easily visible in the still images, rotating floc rollers were formed on the inner wall. The relative slip velocity of the 0.5% suspension is only ca. 0.5 because the slip occurs at both boundaries as seen in the velocity profiles in Figure 23a-c. The decrease in the slip velocity at the lowest shear rates means that the bulk of the MFC suspension is detached from the outer wall and finally ceases to flow when the apparent shear rate is small enough.

While the MFCs that were pre-sheared are quite evenly distributed in the rheometer gap, the 1% MFC sample that was not pre-sheared appears more aggregated. At the highest shear rate shown in Figure 23g, the velocity profile corresponds to a plug flow with slipping at the outer boundary. At some point in the transition region, the sample breaks loose from the surfaces and water layers begin to separate at the boundaries and 'rollers' are occasionally formed (see also Figure 21). When the rollers appear at the gap, the rest of the suspension eventually stops as the shear rate decreases, except of local deformations caused by the passing rollers.
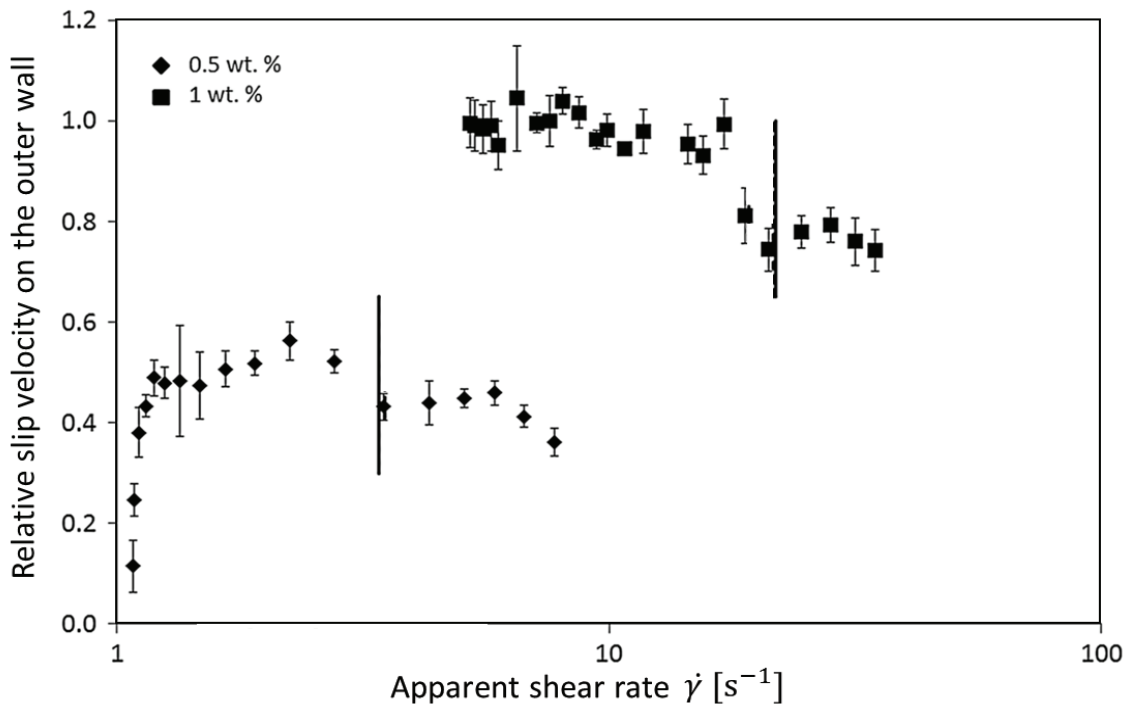
Figure 24   Relative slip at the outer wall in 0.5% (diamonds) and 1% MFC (squares) suspensions as determined from the OCT structure images using image correlation algorithm. The relative slip velocity is the slip velocity u_{slip} scaled by velocity of the inner wall. Vertical lines show the yield stress of the suspension. (Paper III)

The structural data acquired with the OCT suggests that the rollers form in conjunction with a thickening water layer near the solid boundaries. The process of roller formation is illustrated in Figure 25a. As the shear rate is decreased, also the hydrodynamic lift force, created by the velocity difference between MFC phase and fluid phase near the wall, is also decreased (Leighton & Acrivos 1987, Barnes 1995, Jäsberg et al. 2000, Medhi, Kumar & Singh 2011). Consequently, the elastic stress retained in the MFC network occasionally pushes the flocs into direct contact with the wall, leading to breaking of the floc structure. When such fracturing begins, the outer layer of the suspensions starts to cease and the flocs near the inner wall are being pulled into counter clockwise rotating motion, to form rollers. As the MFC fibrils entangle and form new contacts with each other, the roller formation is further enhanced. This process releases water out of the bulk of the suspension spun into the rollers, as can clearly be evidenced from the OCT images in Figure 23 and Figure 25. Since there is no velocity gradient in the vertical direction, and due to the attraction between the fibers, the rollers grow in length, i.e. in the axial direction of the concentric cylinders. With time, and further decrease of the shear rate, the diameter of the rollers and the thickness of virtually pure water layers increase. Finally, the main bulk layer may stop completely, and the continuing motion of the rollers collects even more fibrils.
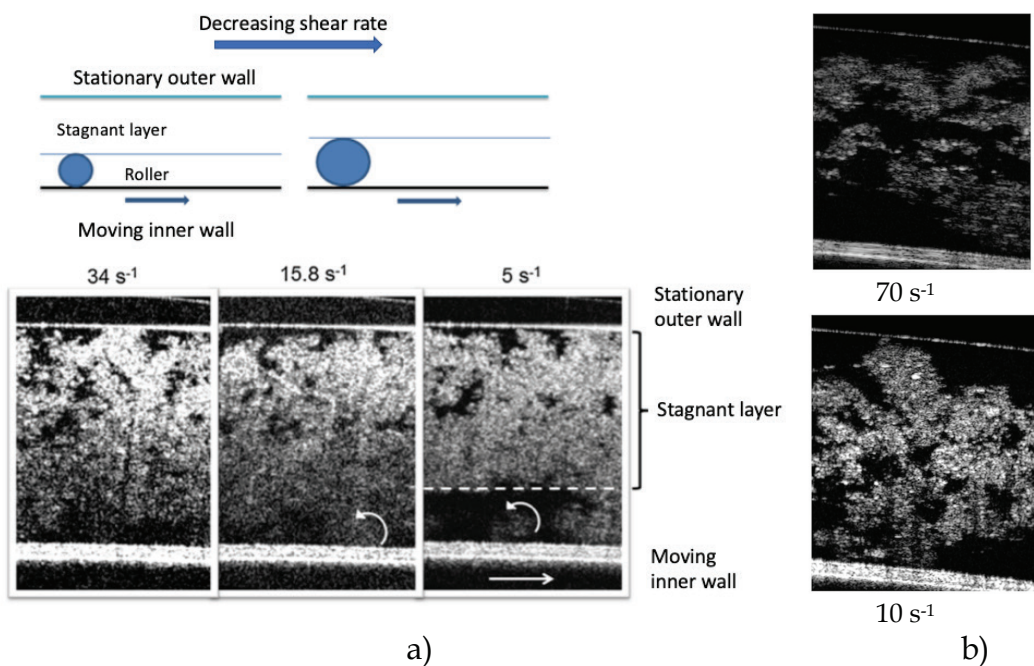
Figure 25   a) Formation of rollers in shear flow of pre-sheared 1% MFC suspension in the presence of electrolytes that promote the flocculation tendency. The formation of rollers begins in the transition region and the size of them is increased upon decreasing the shear rate (Paper II). b) Formation of large rollers spanning across the rheometer gap with the coarse grade MFC suspension at apparent shear rates of 70 s^{-1} and 10 s^{-1} (unpublished data).

Roller formation with MFC suspensions has been observed also in earlier studies with optical access in the rheometer gap. In (Saarikoski et al. 2012), the formation of vertical crevices occurred in the direction of greatest compression in

experiments comprising of several different intervals of constant shear stress. Furthermore, Karppinen et al. observed rollers spanning across the whole gap after steady shear intervals of 10 min at apparent shear rate of 0.5 s^{-1} with samples having dry matter content of 0.1% and 0.25% (Karppinen et al. 2012). In this thesis, similar behavior was found with the 0.4% coarse grade MFC suspension where rollers started to form already at apparent shear rates smaller than ~100 s^{-1}. Due to heavily flocculated structure and formation of rollers spanning across the whole rheometer gap starting at shear rate of ~10 s^{-1} (see Figure 25b) rendered the rheological data of the coarse grade MFC using smooth concentric cylinders practically useless.

To summarize, flow curve measurements with MFC suspensions are severely affected by shear localization effects both in the transition region and at low shear rates. At high values of shear rate ($\dot{\gamma} \gtrsim 50 \text{ s}^{-1}$), apparent wall slip was found, but the shear profile was nearly linear, and the apparent shear rate given by the rheometer was thus higher than that measured by the DOCT. It can thus be concluded that conventional rotational rheometric analysis of the bulk properties of MFC suspensions using smooth concentric cylinders at shear stress values below their yield stress, does not appear appropriate – despite the seemingly reasonable power-law flow curves thereby obtained. Without a direct observation of the flow behavior of the MFC suspension, the nature and significance of e.g. the shear localization effects remain unclear. This, in turn, may render delusive the observed relationship between the rheological data and e.g. microstructure of the studied MFC materials.

5.2.1.3   Oscillatory measurements

In this section, oscillatory measurements are briefly considered. Oscillatory measurements have been extensively used to characterize the contribution of elastic and viscous interactions on the flow properties as well as mechanical properties of MFC materials. In particular, oscillatory measurements have been suggested to help in characterizing the interactions between the MFC fibrils in the networked structure (Hubbe et al. 2017).

An example of typical amplitude sweep used to determine the linear viscoelastic (LVE) region of a sample is shown in Figure 26. In addition, shown are measured velocity profiles of the MFC phase in two different values of applied strain. The velocity profiles were calculated at the points corresponding to the highest absolute values of the shear rate. With the lower strain of 0.78%, the velocity profiles are approximately linear but somewhat asymmetric close to the stationary wall. At the moving wall, shear banding and slip flow may be observed. With the higher value of strain, the velocity profiles are approximately symmetric and quite linear in the middle of the gap. However, shear banding occurs on both walls, and there is strong slip flow on the moving wall. These results suggest that oscillatory measurements may not be free from shear localization effects, even though the measurement is made in the LVE region. The benefit of performing OCT measurements also during the oscillatory measurements is thus obvious.
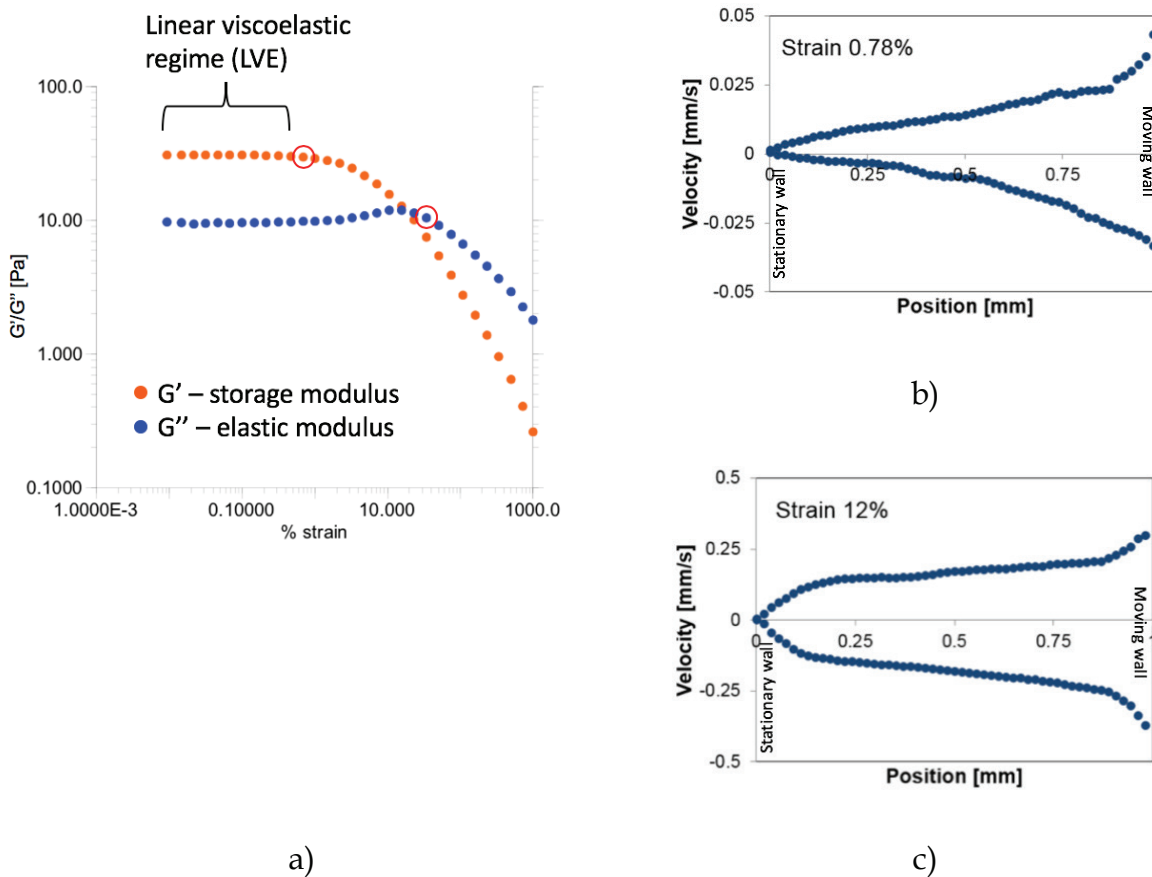
Figure 26   a) Rheogram of an oscillatory experiment for a 0.5% MFC + 0.11% CMC suspension in a concentric cylinders rheometer geometry. b) Velocity profile in the gap in the linear viscoelastic region (LVE) region with strain of 0.78%. c) Velocity profile in the gap outside the LVE region with strain of 12%. The frequency of the oscillation is 1.0 Hz, and the maximum speed of the surface of the moving cylinder is thus 0.05 and 0.75 mm/s in b) and c), respectively. Notice that the velocity profiles have been calculated from sequential structural 2D images, with the image correlation algorithm presented in (Salmela and Kataja 2005). The data presented in the subfigures is unpublished. However, supporting data can be found in (Sorvari et al. 2014).

5.2.2   Pipe rheometer

This section relates to the Papers III and IV where the combination of hybrid velocity profiling and pressure loss measurement was to investigate the rheology and flow properties of MFC suspensions. In addition to analyzing the bulk rheology, the boundary layer behavior of the coarse grade MFC suspension in concentrations of 0.4, 1.0, and 1.6% is studied in order to gain insight in the wall layer dynamics of MFC suspensions. Pipe rheometer studies including flocculation analysis with the fine grade MFC can be found in supporting publications (Lauri et al. 2017) and (Koponen et al. 2018).

5.2.2.1 Pressure loss and velocity profiles

The basis of the velocity profiling rheometry in pipe flow lies in obtaining the temporal averages of the pressure loss and velocity profiles in stationary flow conditions. In Figure 27 shown is the measured pressure loss as a function of the flow rate measured in a straight tube of diameter of 19 mm (setup B) at various values of MFC suspension concentration. According to Figure 27, the pressure loss behavior of the MFC suspensions is found to be qualitatively similar to that of pseudoplastic (shear-thinning) fluids. At the highest concentration of 1.6%, the pressure loss shows a distinct plateau, similar to what is often found for e.g. pulp fiber suspensions. The frictional behavior at the wall and, consequently, total pressure drop of pulp fiber suspensions are known to be affected by near-wall phenomena, which can cause the frictional loss to level off or even decrease with increasing flow rate (Duffy 2006, Jäsberg 2007, Sumida 2013). The detailed reason for such behavior in MFC suspensions is discussed later in this chapter.
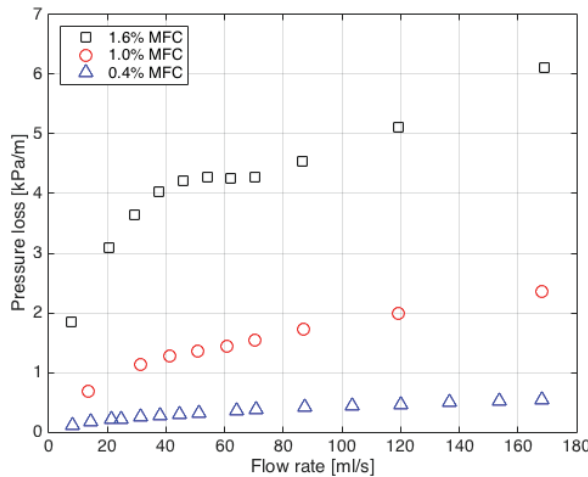
Figure 27   Measured pressure loss vs. flow rate for MFC suspensions at various concentrations (Paper IV).

Subsets of combined stationary velocity profiles using UVP and DOCT are shown in Figure 28 for various total flow rates. The corresponding values of the total flow rate are given as labels to different profiles in the Figure 28. The bulge seen in the highest flow rate of MFC at concentration 0.4% is most likely a measurement artifact originating from spurious reflections of the ultrasound pulses from tube walls. The high-resolution DOCT data with the same flow rates is shown in more detail in Figure 29. Here, the labels to the profiles correspond to the measured wall shear stress. The spatial length of the DOCT profiles have been cut to 600 µm for concentrations 0.4 and 1%, and to 450 µm for concentration 1.6%. Consequently, in the case of MFC at concentration 1.6%, the amplitude of the light signal was reduced so much that the regions of accurate measurement of the DOCT and UVP were non-overlapping at the higher flow rates. Nevertheless, reasonably accurate patching of the profiles could be obtained by using the DOCT results extrapolated by means of the fitting function presented Section 5.2.2.3. The fitted curves are shown with dashed lines in Figure 29.

Owing to the near-wall effects, the velocity profiles of fiber (and MFC) suspensions generally consist of three dynamically different regions also observed also here: a wall boundary layer (called also lubrication layer or slip layer), a yielding layer, and a non-yielding fiber plug (Duffy et al. 1976, Pettersson, Wikström & Rasmuson 2006). The DOCT data (Figure 29) reveals that the velocity profile is indeed very steep and approaches rapidly zero in a thin region (typically $< 200\,\mu$m) near the wall. In this region, the amplitude signal also decreases abruptly, as was shown in Figure 17a. As in the case of rotational rheometer (Couette geometry), actual wall slip is not observed, but water-rich depletion layer is most likely created at the wall. The formation of such layers is discussed in more detail later in this chapter.

In the interior part of the tube, at distances greater than $\sim$200 μm, the profile is relatively shallow and qualitatively resembles that of a shear-thinning fluid. Thus, in the macroscopic scales, the flow behavior of MFC appears as that of a shear-thinning fluid with wall slip. Furthermore, a plug flow region, related to the yield stress of the MFC suspension, is observed near the tube centerline, especially with the two higher concentrations. The yield stress analysis based on identifying the plug region in the velocity profile is omitted in this thesis. Instead, yield stress values determined by pipe rheometer and rotational rheometer for identical MFC material can be found in (Haavisto et al. 2011) and can also be found in Paper III.

a) MFC 0.4%

b) MFC 1.0%

c) MFC 1.6%
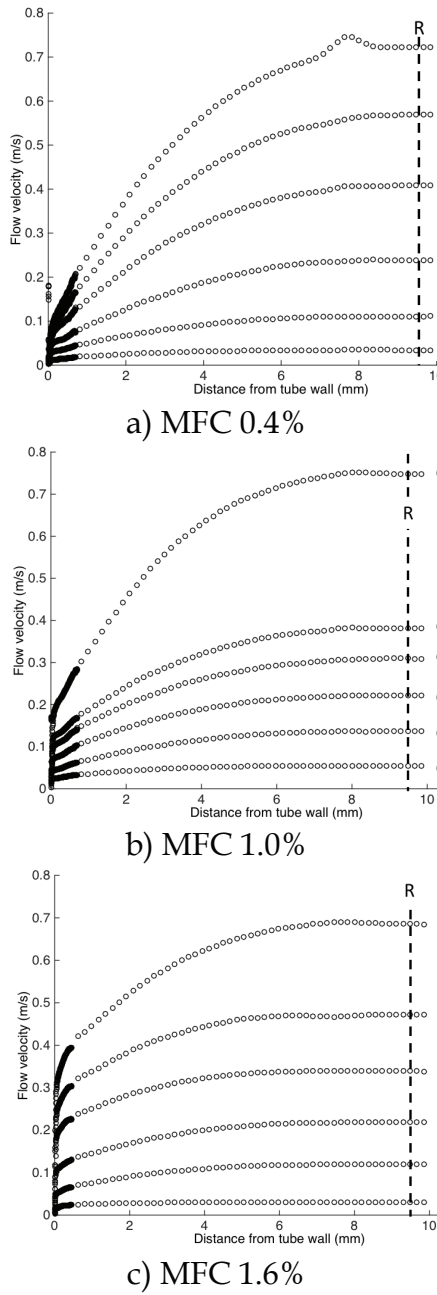
Figure 28   Velocity profiles of three different MFC suspensions combined from DOCT and UVP measurements. The velocity values from DOCT are indicated by the dark symbols near the wall. The labels to different profiles give the total flow rate [ml/s], and the vertical dashed lines indicate the centerline of the tube. (Paper IV)

a) MFC 0.4%

b) MFC 1.0%

c) MFC 1.6%
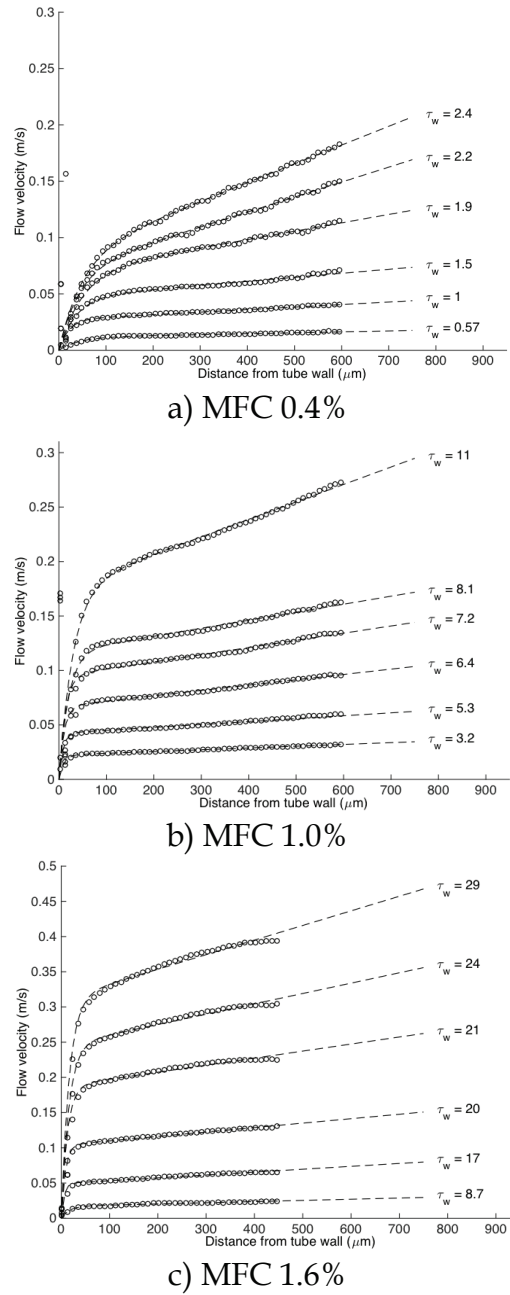
Figure 29   Near-wall velocity profiles measured by DOCT. The labels to different profiles give the wall shear stress [Pa]. Graphs of the Eq 4.1 fitted to the DOCT data are shown with dashed lines. (Paper IV)

5.2.2.2 Viscosity characteristics

Figure 30a summarizes the values of viscosity as a function of shear rate, obtained using Equations 3.1 – 3.4, for all values of flow rate, and for the three MFC concentrations. The value of viscosity depends strongly on the MFC concentration. At the same shear rate, the viscosity of the 1.6% MFC suspension is more than ten times higher than that of the 0.4% MFC suspension. This is due to increasing amount of fibrils per volume, which makes the fibril network more rigid (Celzard, Fierro & Kerekes 2009). The viscosity behavior of the MFC suspensions show overall shear-thinning characteristics, in qualitative agreement with the results obtained for different types of MFC suspensions using conventional rheometric techniques (Agoda-Tandjawa et al. 2010, Iotti et al. 2011, Nazari et al. 2016, Naderi & Lindström 2016). At low values of shear rate ($\dot{\gamma} \lesssim 10 \ s^{-1}$), achieved in the inner parts of the tube, the measured values of viscosity show power-law type correlation with the shear rate. This behaviour is typical for fibre suspensions, and is believed to be due to adhesive contacts between the fibres that are broken by the shear forces when the shear rate increases (Petrich, Koch & Cohen 2000). As a result, the (floc) structure of the MFC suspension changes (Karppinen et al. 2012, Saarikoski et al. 2012).

a)   b)
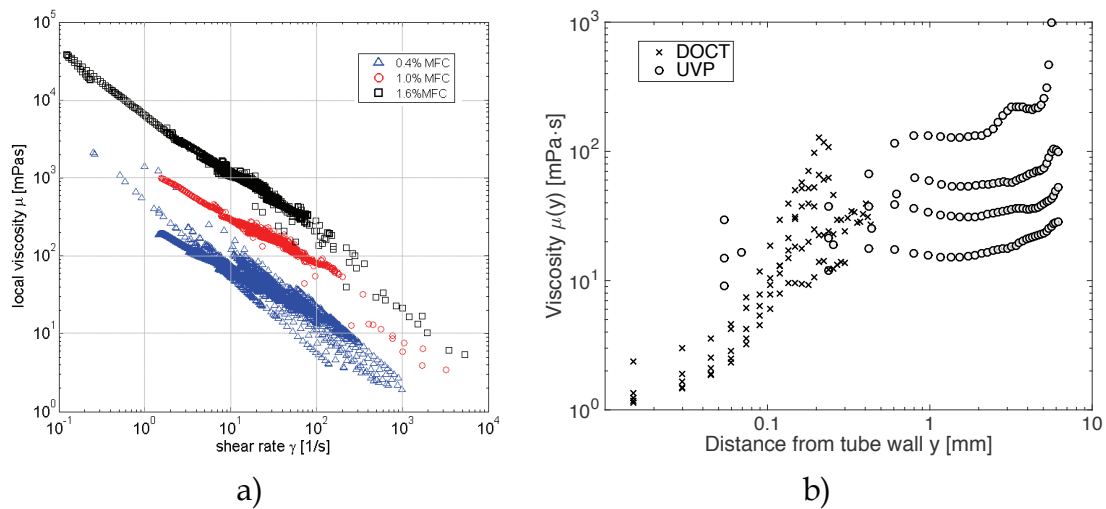
Figure 30   a) Viscosity of MFC suspensions at various concentrations as a function of shear rate, calculated locally from the measured velocity profiles (Paper IV). b) Viscosity as a function of the distance from the tube wall. Both DOCT and UVP data are shown (DOCT data has been published in (Haavisto et al. 2017), UVP data is unpublished).

At higher values of shear rate, related to the near-wall boundary layer, the viscosity behavior is qualitatively different. The viscosity does not show clear correlation with the shear rate alone, but appears to depend also on the local concentration (distance from the tube wall). Figure 30b shows the viscosity $\mu(y)$ as a function of y across the pipe radius in logarithmic scales. The DOCT data suggest that the viscosity of 0.4% MFC suspension increases with the distance from the wall until $y \approx 0.15$–0.2 mm. Within the boundary layer, the values of viscosity may thus be significantly lower than in the bulk of the material. The shear-

thinning behavior of MFC in macroscopic scales is seen as different levels of viscosity at $y \gtrsim 0.2$ mm. Furthermore, the transition between the yielding region and the plug flow region may be observed as a rapid increase in the viscosity near the tube centerline.

5.2.2.3 Boundary layer behavior

In this section, the wall boundary layer behavior and the rheological properties of MFC suspension are studied by applying a parameterization to the measured velocity profiles. As presented in Figure 31, the measured DOCT velocity profiles within the region $y \lesssim 500\ \mu$m can be closely approximated by the formula

$$u(y) = \dot{\gamma}_w^a y + u_s^a\left(1 - e^{-y/\lambda_w}\right), \tag{4.3}$$

where $\lambda_w, u_s^a, \dot{\gamma}_w^a$ are and free parameters found by fitting in the data. The parameter λ_w characterizes the thickness of the wall boundary layer underlying the apparent wall slip. The parameters $\dot{\gamma}_w^a$ and u_s^a can be interpreted as the apparent wall shear rate and the apparent slip velocity, respectively. The graphical interpretations of the parameters are shown with red color in Figure 31. As suggested by the definitions, the term 'apparent' is used here to refer to wall quantities observable in the macroscopic scales and related to the velocity profile shape just outside the boundary layer ($y \gtrsim \lambda_w$). In principle, the apparent parameters could be measured using UVP or other low-resolution velocity profiling technique, such as MRI, alone. The results obtained here, however, suggest that the measurement of the thickness and the velocity within the boundary layer require a high-resolution method, such as DOCT.
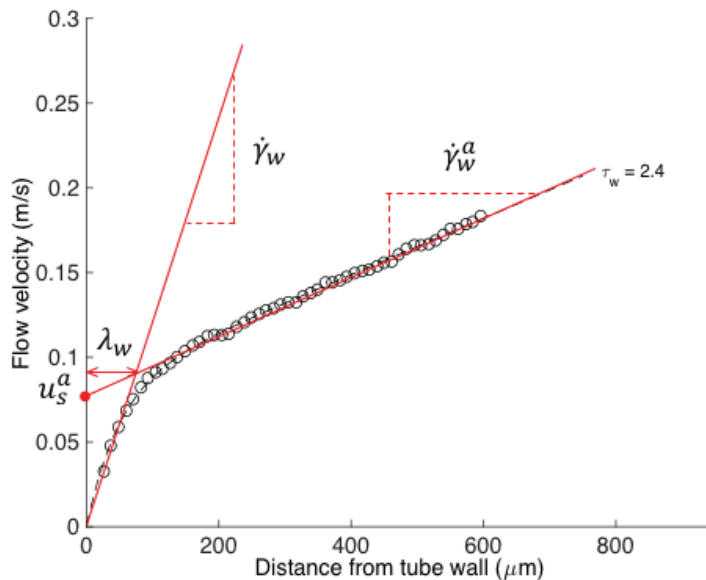
Figure 31   Parameterization of the velocity profiles measured in the near-wall region of the tube. The geometric interpretation of the parameters $\lambda_w, u_s^a, \dot{\gamma}_w^a$ are shown with red color. The dashed red lines indicate slope of the red lines fitted in the velocity data.

In terms of the free parameters in Equation 4.1, the apparent value of viscosity at the wall is defined as

$$\mu_w^a = \tau_w / \dot{\gamma}_w^a. \tag{4.4}$$

Notice, that as μ_w^a equals the viscosity outside the boundary layer, it also represents the viscosity in the bulk of the suspension. The shear rate at the wall, $\dot{\gamma}_w = \left(\frac{du}{dy}\right)_{y=0}$, is given by

$$\dot{\gamma}_w = \dot{\gamma}_w^a + \frac{u_s^a}{\lambda_w}. \tag{4.5}$$

The DOCT velocity profiles shown in the Figure 29 indicate that typically, the shear rate within the boundary layer is significantly higher as compared to the shear rate outside the boundary layer. Thus, the viscosity at the tube wall is clearly lower than the apparent viscosity ($\mu_w \ll \mu_w^a$).

　　Figure 32 shows the measured wall shear stress (a) and the apparent viscosity (b) at the wall (viscosity in the bulk) as functions of apparent wall shear rate at the three concentrations of the MFC suspensions. The shear-thinning behavior and strong dependence on the concentration of MFC suspensions is evident also in these figures. Furthermore, especially at lower values of concentration, the viscosity behavior is qualitatively close to that of a power-law fluid for which $\tau \propto \dot{\gamma}^{\frac{1}{2}}$ $\left(\mu \propto \dot{\gamma}^{-\frac{1}{2}}\right)$. This value is in accordance with what has been reported earlier (Lasseuguette, Roux & Nishiyama 2008, Haavisto et al. 2011).
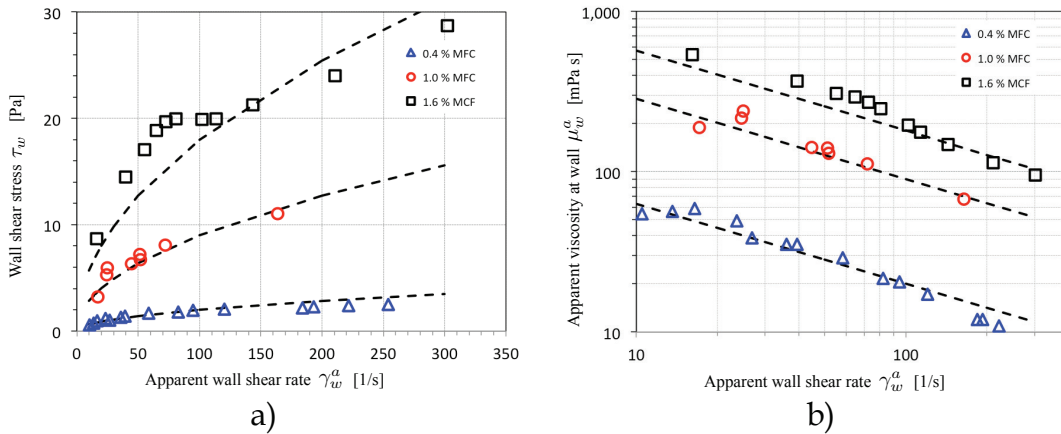
Figure 32　a) Shear stress at the tube wall as a function of apparent shear rate at the wall. b) Apparent viscosity at the tube wall (viscosity in the bulk) as a function of apparent shear rate at the wall. Dashed lines representing a power law behavior $\tau \propto \dot{\gamma}^{\frac{1}{2}}$ are shown for reference. (Paper IV)

The plateau visible in the shear stress (and pressure loss in Figure 27) of the 1.6 % MFC is presumably related to the formation of a concentration gradient and a particle depletion layer near the wall due to combined effect of steric hindrance and repulsive hydrodynamic interaction between the tube wall and suspended particles (Leighton & Acrivos 1987, Barnes 1995, Jäsberg et al. 2000, Medhi, Kumar & Singh 2011). Indeed, this transition occurring at $\tau_w \approx 20$ Pa is observed also

outside the boundary layer. The viscosity in the suspension bulk indicates a transition between two power laws in a narrow region around shear rate of $\dot{\gamma}_w^a \approx$ 100 s^{-1}. Qualitatively similar behavior has been found also for a 0.5% MFC suspension identical to the fine grade MFC material used in this study. In pipe rheometer experiments by (Lauri et al. 2017) an abrupt change in the viscosity level and the power-law constant was observed approximately at wall shear stress of 10 Pa and shear rate of 100 s^{-1}. This kind of rheological behavior has been attributed to a structural change in the MFC suspensions. Measurements with a sub-micron resolution OCT device suggested that an abrupt drop in the size of the flocculated structures occurs in the transition region (Koponen et al. 2018).

Further evidence on the formation of wall layer is presented in Figure 33 which shows the measured dependence of the viscosity at the wall (a), and of the apparent slip velocity on the wall shear stress (b). At low values of wall shear stress (and of flow rate), viscosity at wall decreases and slip velocity increases with wall shear stress. As the wall shear stress increases, a transition dependent on the MFC concentration is observed. In the case of 1.6% MFC, an obvious transition occurs at $\tau_w \approx$ 20 Pa. In the transition, the apparent slip velocity increases rapidly while viscosity at wall becomes nearly Newtonian with values close to that of water ($\mu_w \sim 1$ mPa $\cdot$ s). In the case of 1.0% MFC and 0.4% MFC, similar but less pronounced transitions occur at $\tau_w \approx$ 7 Pa and $\tau_w \approx$ 1 Pa, respectively. At the lowest consistency of 0.4%, however, the transition is barely visible in the viscosity behavior and cannot be observed in the slip velocity.

a)   b)
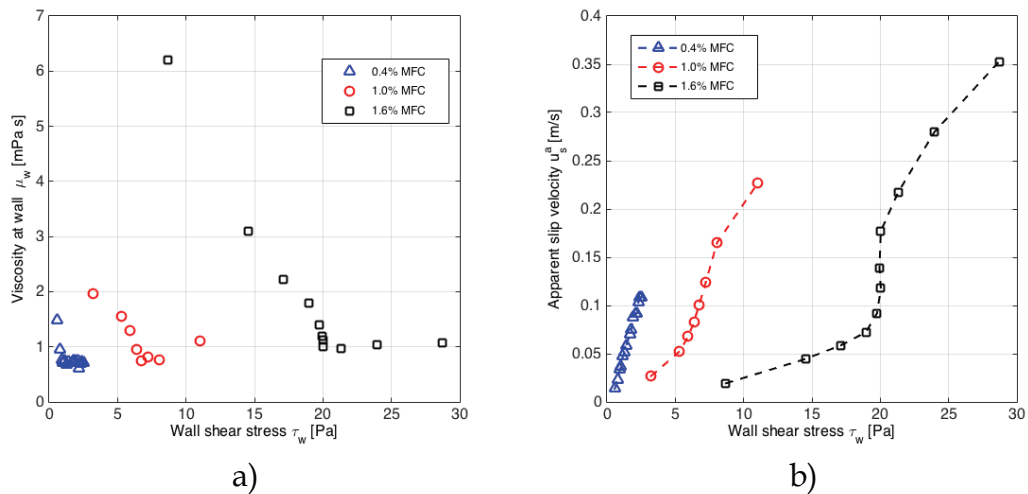
Figure 33   Viscosity at tube wall (a) and apparent slip velocity (b) as functions of wall shear stress for MFC suspension at various concentrations (Paper IV).

To explain the behavior reflected in Figure 33, the following scheme is proposed: At low flow rate, the solid phase is in contact with tube wall, and thereby contributes to the total friction. The repulsive hydrodynamic force between the tube wall and the particles increases with flow rate leading to gradual decrease of elastic normal force and of direct friction between particles and the wall. In the transition point, repulsive interaction overcomes the elastic stress in the MFC material and a narrow layer of almost pure water is formed near the wall. The formation of such depletion layers in pipe flow of pulp suspensions is a well known

phenomenon (Jäsberg 2007, Derakhshandeh et al. 2011, Fock et al. 2011), and has been discussed for MFC suspensions in e.g. References (Kumar et al. 2016, Nazari et al. 2016). Moreover, the increase of the transition point and the more distinct characteristics of the transition with increasing concentration are qualitatively explained by the increase of elastic stiffness and rigidity of the fibrous MFC network. The amount of fibrils and thus contacts per volume is increased with concentration.

Corresponding results for identical MFC suspensions at different concentrations were obtained also with setup A, i.e. pipe with a smaller diameter. For instance, the measured dependence of the viscosity at the wall for 0.4% MFC suspension, shown in Figure 34a, exhibits similar transition to Newtonian behavior when $\tau_w \approx 1.2$ Pa. This value was obtained by fitting two straight lines in the data and determining their intersection point (see Figure 34a). Similar analysis was carried out for the data obtained with the both pipe rheometer setups A and B. Interestingly, the values of wall shear stress where the transitions occur are approximately twice the yield stress of the suspension at the corresponding concentration, as shown in Figure 34b. The yield stress values have been adapted from measurements with a similar MFC type using a rotational rheometer (Haavisto et al. 2011).

a)   b)
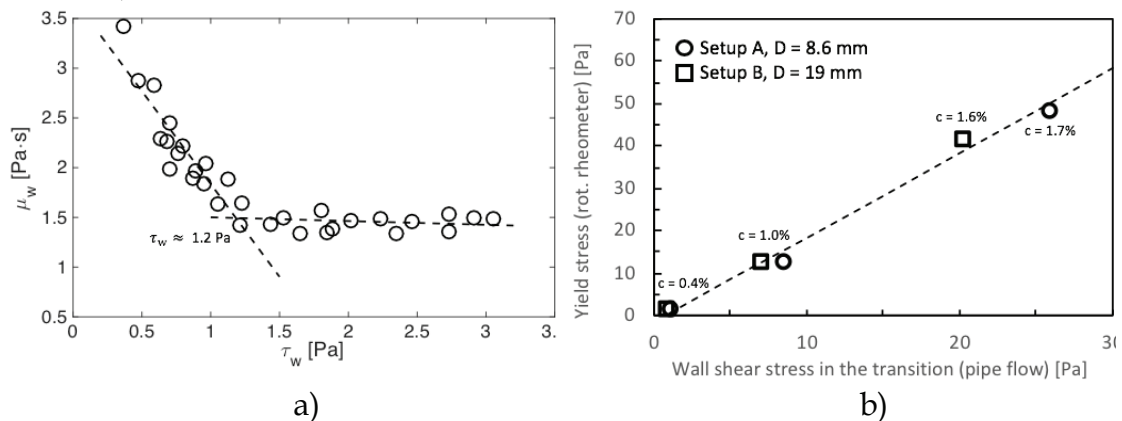
Figure 34   a) Viscosity at tube wall as function of wall shear stress for 0.4% MFC suspension as determined using setup A. (Paper III) b) Yield stress determined using a rheometer as a function of wall shear stress in the transition point as determined in pipe flow. Dashed line representing $\tau \propto 2\tau_y$ is shown for reference (unpublished).

Next, the thickness of the wall boundary layer (slip layer) is briefly visualized using the structural information (amplitude signal) obtained simultaneously with the velocity information. Figure 35 shows examples of still images of the structure of MFC suspension flow near the tube wall together with the long-time averaged images. The grey-scale values in the images represent the local value of the optical back-scattering index, light color corresponding to a low index value. The scattering index, in turn, correlates with the concentration of the suspended particles that contribute to scattering. The light shades of grey near the tube wall indicate lower mean (time-averaged) concentration as compared to the inner parts of the tube. Whereas the concentration boundary layer is quite easily seen for the 0.4% MFC suspension, it is barely visible in the case of the 1.6% MFC suspension. In fact,

looking at the mean amplitude signals of different concentrations shown in Figure 17, the concentration of the MFC phase in the boundary layer seems to gradually increase when moving away from the wall. The width of the concentration boundary layer is approximately 200 μm and 50 μm for the 0.4% MFC and 1.6% MFC, respectively. The correlation between concentration and viscosity will be studied in more detail in the future work.

The values of wall layer thickness λ_w fitted using the velocity data are approximately in the range of 10 – 50 μm being smaller with the higher concentrations (see Figure 29 and Figure 31). These values are in line with the observed wall layer in the rheometer geometry (10 – 15 μm) (Figure 22). A commonly used method for estimating the thickness of the wall layer is to assume that the slip takes place in a layer of pure water. Results obtained using such approach are in the same order of magnitude with the values in this study. Kumar et al. studied flow of a 1% MFC suspension in a 2 mm pipe obtaining wall layer thicknesses varying approximately between 10 and 80 μm in the flow velocity range of 130 – 2000 mm/s (Kumar et al. 2016). Nazari et al., in turn, studied 1% MFC suspension with a rotational rheometer equipped with a parallel plate geometry. With shear rates of 200 and 500 s-1, they obtained wall layer thicknesses of 6 and 16 μm, respectively (Nazari et al. 2016).

a) MFC 0.4% (single) b) MFC 1.6% (single)

c) MFC 0.4% (average) d) MFC 1.6% (average)
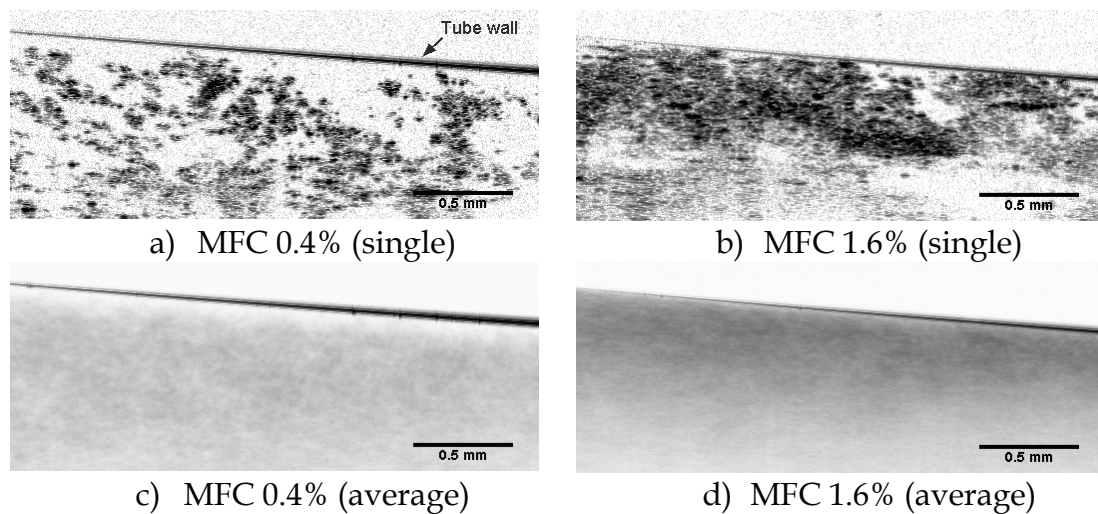
Figure 35   OCT B-scans (a-b) and longtime average images (c-d) of the boundary layer flow of MFC suspension of concentrations 0.4% and 1.6% at volumetric flow rate of 38 ml/min. The regions covered by MFC and water are shown in the B-scan images as dark and light grey shades, respectively. The time averaged images are obtained as mean of 200 still images taken over a time interval of ca. 20 s. The boundary layer with concentration decreasing towards the tube wall appears as lighter grey color and is indicated by arrows in subfigure a). The apparent inclination of the tube wall is due to setting (Doppler) angle of the DOCT measuring probe, as required for axial velocity measurement. (Paper IV)

6 CONCLUDING REMARKS

In this thesis, a commercial Optical Coherence Tomography (OCT) instrument was applied in velocity profiling rheometry, in combination with rotational rheometer and pipe rheometer. Furthermore, a novel hybrid multi-scale velocity profiling method, based on measuring stationary velocity profiles of fluid flow in a straight tube simultaneously by Doppler OCT (DOCT) and Ultrasound Velocity Profiling (UVP), was developed. The DOCT and the hybrid method were used to study rheological properties and, in particular, boundary layer behavior of aqueous microfibrillated cellulose (MFC) suspensions. In addition to velocity profiling, the imaging modality of the OCT was utilized in characterizing the structural behavior of MFC suspensions near the pipe wall and inside the rheometer gap.

In rotational rheometry, the objective was to follow the structure of the suspensions inside the rheometer gap during rheological testing and observe complex behavior that can interfere with the rheological results. The flow curve measurements were significantly affected by wall depletion throughout the applied shear rate range. An essential factor for the rheological characteristics of the fluid in a flow was whether the shear stress at a given apparent shear rate was above or below the yield stress. Above the yield stress, the bulk of the suspension was being sheared across the gap, but at the same time apparent wall slip was present. Therefore, the apparent shear thinning above the yield stress reflected the adaptation of the floc structure to the apparent shear rate as evidenced from the structural OCT images.

Below the yield stress, the flocs stuck together, and the response varied with concentration (0.5% and 1.0% by weight) and sample handling (pre-shearing) before the rheological testing. Decreasing MFC concentration or omission of pre-shearing interval decreased the amount of water that is held within the MFC network. This led to a thicker layer of almost pure water near the wall, coupled with the formation of cylindrical, rotating floc structures (rollers). The apparent shear thinning below the yield stress did not represent structural changes in the MFC bulk, other than shearing of the fibril-depleted slip layer, which was in some cases coupled with formation and movement of rollers.

As research activities utilizing rheometers complemented with (D)OCT continue, it is still necessary to perform rheological characterization of different

types of MFC suspensions, taking into account oscillatory measurements, various geometry types, surface roughness, gap width, etc. For instance, the dimensions of the measurement may affect the structural (flocculation) behavior of MFC suspensions (Saarinen, Lille & Seppälä 2009). Furthermore, flow curve tests with roughened and serrated geometries should lead to an understanding of the deformation of MFC suspensions when the wall effects are suppressed (Nechyporchuk, Belgacem & Pignon 2014). However, as pointed out also by Nazari et al., experiments characterizing the behavior of MFC materials without allowing the formation of a slipping layer are probably not helpful in predicting their behavior in industrial processes (Nazari et al. 2016).

In pipe flow, hybrid multi-scale velocity profiling was used to study the rheological properties and boundary layer behavior of a coarse grade micro-fibrillated cellulose (MFC) suspension at consistencies 0.4%, 1.0%, and 1.6% by weight. The two measurement methods proved complementary in the manner that the velocity profiling inside the thin boundary layer could be accomplished by the high-resolution DOCT technique while the UVP was useful in measuring the velocity profile in the interior parts of the tube with a lower spatial resolution. A comprehensive velocity profile containing both the thin boundary layer and the interior parts of the flow was acquired by combining the velocity profiles from the two measurement techniques. Such combination was straightforward at lower values of consistency where the valid measuring ranges of the two methods overlapped. At consistency 1.6%, however, the penetration depth of the optical signal of DOCT was reduced too much and distinct overlap of the velocity profiles was not achieved. Even then, sufficient patching of the profiles was obtained by extrapolating the measured DOCT profile.

In the interior parts of the tube where the MFC concentration is constant, in average, the results showed typical shear-thinning behavior, in qualitative agreement with results obtained by conventional rheometric methods. The near wall behavior manifested existence of a boundary layer where the mean concentration decreases towards the wall. The maximum boundary layer thickness observed here was of the order of 200 μm and the thickness was found to decrease with MFC concentration. Such a concentration gradient is plausibly created by combined effect of steric hindrance by the wall and hydrodynamic lift that induces migration of MFC particles away from the wall. The fluid in the boundary layer may become nearly Newtonian with viscosity close to that of water as the flow rate (wall shear stress) is increased. Such behavior suggests existence of a sublayer depleted of particles in the close vicinity of the wall and leads to apparent wall slip. The local value of viscosity increases with distance from the wall, coupled with increasing concentration. The concentration boundary layer can be directly observed by using the imaging modality of optical coherence tomography. In addition to determining the thickness of the boundary layer, the OCT data can be analyzed for size of the flocculated structures near the tube wall (Koponen et al. 2018). More detailed study of the correlation between concentration and viscosity will be presented elsewhere.

Optical Coherence Tomography is a very attractive tool for analyzing inhomogeneous behavior of complex fluids encountered in viscometric flows. The many advantages of DOCT technology, including high resolution, high speed,

ability to work with opaque fluids, and simultaneous detection of velocities and structure are a combination that opens truly unprecedented research prospects. In addition to enabling the calculation of shear viscosity based on the true velocity field, DOCT gives explicit information on the slip flow, wall depletion and flocculation behavior. Furthermore, the emergence of commercial OCT devices that are compact and flexible is expected to lower the threshold at which researchers can adapt them in rheological testing as well as other applications that can benefit simultaneous characterization of velocity fields and structure of the sample.

REFERENCES

Agoda-Tandjawa, G., Durand, S., Berot, S., Blassel, C., Gaillard, C., Garnier, C. & Doublier, J. 2010. Rheological characterization of microfibrillated cellulose suspensions after freezing. Carbohydrate Polymers 80 (3), 677-686.

Ahn, Y., Jung, W. & Chen, Z. 2008. Optical sectioning for microfluidics: secondary flow and mixing in a meandering microchannel. Lab on a Chip 8 (1), 125-133.

Arola, D. F., Barrall, G. A., Powell, R. L., McCarthy, M. J. & McCarthy, K. L. 1997. Use of nuclear magnetic resonance imaging as a viscometer for process monitoring. Chem. Eng. Sci. 52 (13), 2049-2057.

Barnes, H. A. 1999. The yield stress—a review or 'παντα ρει'—everything flows? Journal of Non-Newtonian Fluid Mechanics 81 (1-2), 133-178.

Barnes, H. A. 1997. Thixotropy—a review. Journal of Non-Newtonian Fluid Mechanics 70 (1-2), 1-33.

Barnes, H. A. & Nguyen, Q. D. 2001. Rotating vane rheometry—a review. Journal of Non-Newtonian Fluid Mechanics 98 (1), 1-14.

Barnes, H. A. 1995. A review of the slip (wall depletion) of polymer solutions, emulsions and particle suspensions in viscometers: its cause, character, and cure. Journal of Non-Newtonian Fluid Mechanics 56 (3), 221-251.

Barrat, J.,and Jean-Pierre Hansen. 2003. Basic Concepts for Simple and Complex Liquids. Cambridge: Cambridge University Press.

Birkhofer, B. H., Jeelani, S. A., Windhab, E. J., Ouriev, B., Lisner, K., Braun, P. & Zeng, Y. 2008. Monitoring of fat crystallization process using UVP–PD technique. Flow Measurement and Instrumentation 19 (3-4), 163-169.

Blanc, F., Peters, F. & Lemaire, E. 2011. Local transient rheological behavior of concentrated suspensions. Journal of Rheology 55 (4), 835-854.

Bonn, D. & Denn, M. M. 2009. Materials science. Yield stress fluids slowly yield to analysis. Science (New York, N.Y.) 324 (5933), 1401-1402.

Boufi, S., González, I., Delgado-Aguilar, M., Tarrès, Q., Pèlach, M. À & Mutjé, P. 2016. Nanofibrillated cellulose as an additive in papermaking process: A review.

Brezinski, M. E. 2006. Optical Coherence Tomography. Academic Press. Principles and Applications.

Britton, M. M. & Callaghan, P. T. 1997. Two-phase shear band structures at uniform stress. Physical Review Letters 78 (26), 4930-4933.

Brunn, P., Müller, M. & Wunderlich, T. 1997. New rheometric technique: the gradient-ultrasound pulse Doppler method. Applied Rheology 7 (5), 204-210.

Buscall, R. 2010. Letter to the Editor: Wall slip in dispersion rheometry. Journal of Rheology 54 (6), 1177-1183.

Celzard, A., Fierro, V. & Kerekes, R. 2009. Flocculation of cellulose fibres: new comparison of crowding factor with percolation and effective-medium theories. Cellulose 16 (6), 983.

Chen, Z. & Zhang, J. 2015. Doppler optical coherence tomography. In W. Drexler & J. G. Fujimoto (Eds.) Optical Coherence Tomography: Technology and Applications. (2nd edition) Switzerland: Springer, 1289-1320.

Cito, S., Ahn, Y., Pallares, J., Duarte, R. M., Chen, Z., Madou, M. & Katakis, I. 2012. Visualization and measurement of capillary-driven blood flow using spectral domain optical coherence tomography. Microfluidics and Nanofluidics 13 (2), 227-237.

Clemons, C. 2016. Nanocellulose in spun continuous fibers: A review and future outlook. Journal of Renewable Materials 4 (5), 327-339.

Cloitre, M. & Bonnecaze, R. T. 2017. A review on wall slip in high solid dispersions. Rheologica Acta 56 (3), 283-305.

Colson, J., Bauer, W., Mayr, M., Fischer, W. & Gindl-Altmutter, W. 2016. Morphology and rheology of cellulose nanofibrils derived from mixtures of pulp fibres and papermaking fines. Cellulose 23 (4), 2439-2448.

Coussot, P. 2005. Rheometry of pastes, suspensions, and granular materials: applications in industry and environment. John Wiley & Sons.

Derakhshandeh, B., Kerekes, R., Hatzikiriakos, S. & Bennington, C. 2011. Rheology of pulp fibre suspensions: A critical review. Chem. Eng. Sci. 66 (15), 3460-3470.

Derakhshandeh, B., Hatzikiriakos, S. G. & Bennington, C. P. 2010. Rheology of pulp suspensions using ultrasonic Doppler velocimetry. Rheologica acta 49 (11-12), 1127-1140.

Deshpande, A. P. 2010. Oscillatory shear rheology for probing nonlinear viscoelasticity of complex fluids: Large amplitude oscillatory shear. In Rheology of complex fluids. Springer, 87-110.

Dimic-Misic, K., Nieminen, K., Gane, P., Maloney, T., Sixta, H. & Paltakari, J. 2014. Deriving a process viscosity for complex particulate nanofibrillar cellulose gel-containing suspensions. Appl.Rheol 24 (3).

Dimitriou, C. J., Casanellas, L., Ober, T. J. & McKinley, G. H. 2012. Rheo-PIV of a shear-banding wormlike micellar solution under large amplitude oscillatory shear. Rheologica acta 51 (5), 395-411.

Divoux, T., Fardin, M. A., Manneville, S. & Lerouge, S. 2016. Shear banding of complex fluids. Annual Review of Fluid Mechanics 48, 81-103.

Dogan, N., McCarthy, M. & Powell, R. 2002. In‑Line Measurement of Rheological Parameters and Modeling of Apparent Wall Slip in Diced Tomato Suspensions Using Ultrasonics. Journal of Food Science 67 (6), 2235-2240.

Drexler, W. 2004. Ultrahigh-resolution optical coherence tomography. Journal of Biomedical Optics 9 (1), 47-75.

Drexler, W. & Fujimoto, J. G. 2008. Optical Coherence Tomography: Technology and Applications. Berlin, Heidelberg: Springer Berlin Heidelberg.

Duffy, G. G. 2006. Measurements, mechanisms and models: Some important insights into the mechanisms of flow of fibre suspensions. Annual Transactions of The Nordic Rheology Society 14. Nordic Rheology Society, 19.

Duffy, G. G., Titchener, A., Lee, P. & Moller, K. 1976. Mechanisms of flow of pulp suspensions in pipes. APPITA Aust Pulp Pap Ind Tech Assoc .

Dufour, M., Lamouche, G., Detalle, V., Gauthier, B. & Sammut, P. 2005. Low-coherence interferometry - an advanced technique for optical metrology in industry. INSIGHT 47 (4), 216-219.

Eronen, P., Junka, K., Laine, J. & Österberg, M. 2011. Interaction between water soluble polysaccharides and native nanofibrillar cellulose thin films. BioResources 6 (4), 4200-4217.

Fercher, A. F., Drexler, W., Hitzenberger, C. K. & Lasser, T. 2003. Optical coherence tomography - principles and applications. Reports on Progress in Physics 66 (2), 239-303.

Fielding, S. M. 2007. Complex dynamics of shear banded flows. Soft Matter 3 (10), 1262-1279.

Flaud, P., Bensalah, A. & Peronneau, P. 1997. Deconvolution process in measurement of arterial velocity profiles via an ultrasonic pulsed Doppler velocimeter for evaluation of the wall shear rate. Ultrasound in medicine & biology 23 (3), 425-436.

Fock, H., Claesson, J., Rasmuson, A. & Wikström, T. 2011. Near wall effects in the plug flow of pulp suspensions. The Canadian Journal of Chemical Engineering 89 (5), 1207-1216.

Fujimoto, J. & Drexler, W. 2008. Introduction to optical coherence tomography. In J. Fujimoto & W. Drexler (Eds.) Optical Coherence Tomography: Technology and Applications.Berlin Heidelberg: Springer, 1-45.

Fujimoto, J. G. 2003. Optical coherence tomography for ultrahigh resolution in vivo imaging. Nature biotechnology 21 (11), 1361-1367.

García, A., Gandini, A., Labidi, J., Belgacem, N. & Bras, J. 2016. Industrial and crop wastes: A new source for nanocellulose biorefinery.

Gelbart, W. & BenShaul, A. 1996. The "new" science of "complex fluids'. JOURNAL OF PHYSICAL CHEMISTRY 100 (31), 13169-13189.

Ghiglia, D. C. & Pritt, M. D. 1998. Two-dimensional phase unwrapping: theory, algorithms, and software. Wiley New York.

Gibbs, S. J., James, K. L., Hall, L. D., Haycock, D. E., Frith, W. J. & Ablett, S. 1996. Rheometry and detection of apparent wall slip for Poiseuille flow of polymer solutions and particulate dispersions by nuclear magnetic resonance velocimetry. Journal of Rheology (1978-present) 40 (3), 425-440.

Gurung, A., Haverkort, J., Drost, S., Norder, B., Westerweel, J. & Poelma, C. 2016. Ultrasound image velocimetry for rheological measurements. Measurement Science and Technology 27 (9), 094008.

Haavisto, S., Lille, M., Liukkonen, J., Jäsberg, A., Koponen, A. & Salmela, J. 2011. Laboratory-Scale Pipe Rheometry: A Study of a Microfibrillated Cellulose Suspension. Proceedings of Papercon 2011. Proceedings of Papercon 2011, 357.

Haavisto, S., Cardona, M. J., Salmela, J., Powell, R. L., McCarthy, M. J., Kataja, M. & Koponen, A. I. 2017. Experimental investigation of the flow dynamics and rheology of complex fluids in pipe flow by hybrid multi-scale velocimetry. Experiments in Fluids 58 (11), 158.

Haavisto, S., Salmela, J., Jäsberg, A., Saarinen, T., Sorvari, A. & Koponen, A. 2013. Rheological characterization of MFC using optical coherence tomography. Paper Conference and Trade Show, PaperCon 2013, Atlanta, GA, United States. Paper Conference and Trade Show, PaperCon 2013.

Han, W., Minear, J. W., Morgan, R. G. & Birchak, J. R. 2001. Method of fluid rheology characterization and apparatus therefore.

Hanlon, A. D., Gibbs, S. J., Hall, L. D., Haycock, D. E., Frith, W. J. & Ablett, S. 1998. Rapid MRI and velocimetry of cylindrical couette flow. Magnetic resonance imaging 16 (8), 953-961.

Harvey, M. & Waigh, T. A. 2011. Optical coherence tomography velocimetry in controlled shear flow. Physical Review E 83 (3).

Herrick, F. W., Casebier, R. L., Hamilton, J. K. & Sandberg, K. R. 1983. Microfibrillated cellulose: morphology and accessibility. J. Appl. Polym. Sci.: Appl. Polym. Symp.;(United States). ITT Rayonier Inc., Shelton, WA.

Hitzenberger, C. K. 1991. Optical measurement of the axial eye length by laser Doppler interferometry. Investigative ophthalmology & visual science 32 (3), 616-624.

Huang, D., Swanson, E., Lin, C., Schuman, J., Stinson, W., Chang, W., Hee, M., Flotte, T., Gregory, K., Puliafito, C. & et, a. 1991. Optical coherence tomography. Science 254 (5035), 1178-1181.

Hubbe, M. A. & Rojas, O. J. 2008. Colloidal stability and aggregation of lignocellulosic materials in aqueous suspension: A review. BioResources 3 (4), 1419-1491.

Hubbe, M. A., Tayeb, P., Joyce, M., Tyagi, P., Kehoe, M., Dimic-Misic, K. & Pal, L. 2017. Rheology of Nanocellulose-rich Aqueous Suspensions: A Review. BioResources 12 (4), 9556-9661.

Ioelovich, M. 2013. Plant biomass as a renewable source of biofuels and biochemicals. LAP LAMBERT Academic Publishing.

Iotti, M., Gregersen, Ø W., Moe, S. & Lenes, M. 2011. Rheological Studies of Microfibrillar Cellulose Water Dispersions. J. Polym. Environ. 19 (1), 137-145.

Irgens, F. 2016. Rheology and non-Newtonian fluids. Springer.

Jaafar, W., Fischer, S. & Bekkour, K. 2009. Velocity and turbulence measurements by ultrasound pulse Doppler velocimetry. Measurement 42 (2), 175-182.

Jaradat, S., Harvey, M. & Waigh, T. A. 2012. Shear-banding in polyacrylamide solutions revealed via optical coherence tomography velocimetry. Soft Matter 8 (46), 11677-11686.

Jäsberg, A. 2007. Flow Behaviour of Fibre Suspensions in Straight Pipes: New Experimental Techniques and Multiphase Modeling. University of Jyväskylä.

Jäsberg, A., Koponen, A., Kataja, M. & Timonen, J. 2000. Hydrodynamical forces acting on particles in a two-dimensional flow near a solid wall. Computer Physics Communications 129 (1), 196-206.

Jonoobi, M., Oladi, R., Davoudpour, Y., Oksman, K., Dufresne, A., Hamzeh, Y. & Davoodi, R. 2015. Different preparation methods and properties of nanostructured cellulose from various natural resources and residues: a review. Cellulose 22 (2), 935-969.

Jowkarderis, L. & van de Ven, Theo GM 2014. Intrinsic viscosity of aqueous suspensions of cellulose nanofibrils. Cellulose 21 (4), 2511-2517.

Kantoush, S. A., De Cesare, G., Boillat, J. L. & Schleiss, A. J. 2008. Flow field investigation in a rectangular shallow reservoir using UVP, LSPIV and numerical modelling.

Kargarzadeh, H., Ioelovich, M., Ahmad, I., Thomas, S. & Dufresne, A. 2017. Methods for Extraction of Nanocellulose from Various Sources. Handbook of Nanocellulose and Cellulose Nanocomposites , 1-49.

Karppinen, A., Saarinen, T., Salmela, J., Laukkanen, A., Nuopponen, M. & Seppälä, J. 2012. Flocculation of microfibrillated cellulose in shear flow. Cellulose 19 (6), 1807-1819.

Karppinen, A., Vesterinen, A., Saarinen, T., Pietikäinen, P. & Seppälä, J. 2011. Effect of cationic polymethacrylates on the rheology and flocculation of microfibrillated cellulose. Cellulose 18 (6), 1381-1390.

Kasai, C., Namekawa, K., Koyano, A. & Omoto, R. 1985. Real-time two-dimensional blood flow imaging using an autocorrelation technique. IEEE Trans.Sonics Ultrason 32 (3), 458-464.

Kerekes, R. J. & Schell, C. J. 1992. Characterization of fibre flocculation regimes by a crowding factor. J. Pulp Pap. Sci. 18, 32-38.

Kikura, H., Yamanaka, G. & Aritomi, M. 2004. Effect of measurement volume size on turbulent flow measurement using ultrasonic Doppler method. Experiments in Fluids 36 (1), 187-196.

Kirk, R. E. & Othmer, D. F. 2008. Food and feed technology. Wiley Interscience.

Koponen, A. I., Lauri, J., Haavisto, S. & Fabritius, T. 2018. Rheological and Flocculation Analysis of Microfibrillated Cellulose Suspension Using Optical Coherence Tomography. Applied Sciences 8 (5).

Korhonen, M. H. J., Sorvari, A., Saarinen, T., Seppälä, J. & Laine, J. 2014. Deflocculation of cellulosic suspensions with anionic high molecular weight polyelectrolytes. BioResources 9 (2), 3550-3570.

Kotzé, R., Wiklund, J., Haldenwang, R. & Fester, V. 2011. Measurement and analysis of flow behaviour in complex geometries using the Ultrasonic Velocity Profiling (UVP) technique. Flow Measurement and Instrumentation 22 (2), 110-119.

Kotze, R., Wiklund, J. & Haldenwang, R. 2013. Optimisation of Pulsed Ultrasonic Velocimetry system and transducer technology for industrial applications. Ultrasonics 53 (2), 459-469.

Kumar, S., Verma, Y., Sharma, P., Shrimali, R. & Gupta, P. 2014. Single detector-based absolute velocity measurement using spectral domain Doppler optical coherence tomography. Applied Physics B 117 (1), 395-399.

Kumar, V., Nazari, B., Bousfield, D. & Toivakka, M. 2016. Rheology of microfibrillated cellulose suspensions in pressure-driven flow. Applied Rheology 55, 3603-3613.

Lasseuguette, E., Roux, D. & Nishiyama, Y. 2008. Rheological properties of microfibrillar suspension of TEMPO-oxidized pulp. Cellulose 15 (3), 425-433.

Lauri, J., Bykov, A. V. & Myllylä, R. 2011. Determination of suspension viscosity from the flow velocity profile measured by Doppler Optical Coherence Tomography. PHOTONICS LETTERS OF POLAND 3 (2).

82

Lauri, J., Koponen, A., Haavisto, S., Czajkowski, J. & Fabritius, T. 2017. Analysis of rheology and wall depletion of microfibrillated cellulose suspension using optical coherence tomography. Cellulose 24 (11), 4715-4728.

Lavoine, N., Desloges, I., Dufresne, A. & Bras, J. 2012. Microfibrillated cellulose - its barrier properties and applications in cellulosic materials: a review. Carbohydrate Polymers 90 (2), 735-764.

Léger, L., Hervet, H., Massey, G. & Durliat, E. 1997. Wall slip in polymer melts. Journal of Physics: Condensed Matter 9 (37), 7719.

Leighton, D. & Acrivos, A. 1987. The shear-induced migration of particles in concentrated suspensions. Journal of Fluid Mechanics 181, 415-439.

Leitgeb, R. A., Werkmeister, R. M., Blatter, C. & Schmetterer, L. 2014. Doppler Optical Coherence Tomography. Progress in retinal and eye research 41, 26-43.

Liimatainen, H., Suopajärvi, T., Sirviö, J., Hormi, O. & Niinimäki, J. 2014. Fabrication of cationic cellulosic nanofibrils through aqueous quaternization pretreatment and their use in colloid aggregation. Carbohydrate Polymers 103, 187-192.

Liu, G., Lin, A. J., Tromberg, B. J. & Chen, Z. 2012. A comparison of Doppler optical coherence tomography methods. Biomedical optics express 3 (10), 2669-2680.

Lowys, M., Desbrieres, J. & Rinaudo, M. 2001. Rheological characterization of cellulosic microfibril suspensions. Role of polymeric additives. Food Hydrocolloids 15 (1), 25-32.

Lundahl, M. J., Klar, V., Wang, L., Ago, M. & Rojas, O. J. 2016. Spinning of Cellulose Nanofibrils into Filaments: A Review. Industrial & Engineering Chemistry Research 56 (1), 8-19.

Malm, A., Waigh, T., Jaradat, S. & Tomlin, R. 2015. Optical coherence tomography velocimetry with complex fluids. JJ. Phys. Conf. Ser. 602 (1), 012039-012045.

Malm, A., Harrison, A. & Waigh, T. 2014. Optical coherence tomography velocimetry of colloidal suspensions. Soft matter 10 (41), 8210-8215.

Manneville, S., Bécu, L. & Colin, A. 2004a. High-frequency ultrasonic speckle velocimetry in sheared complex fluids. The European Physical Journal-Applied Physics 28 (3), 361-373.

Manneville, S., Bécu, L. & Colin, A. 2004b. High-frequency ultrasonic speckle velocimetry in sheared complex fluids. The European Physical Journal-Applied Physics 28 (3), 361-373.

Manneville, S. 2008. Recent experimental probes of shear banding. Rheologica Acta 47 (3), 301-318.

Martinez, D., Buckley, K., Jivan, S., Lindstrom, A., Thiruvengadaswamy, R., Olson, J., Ruth, T. & Kerekes, R. 2001. Characterizing the mobility of papermaking fibres during sedimentation. Proceedings of the Transactions of 12th fundamental Research Symposium, Oxford. , 225.

Martoïa, F., Perge, C., Dumont, P., Orgéas, L., Fardin, M., Manneville, S. & Belgacem, M. 2015. Heterogeneous flow kinematics of cellulose nanofibril suspensions under shear. Soft Matter 11 (24), 4742-4755.

Medhi, B. J., Kumar, A. A. & Singh, A. 2011. Apparent wall slip velocity measurements in free surface flow of concentrated suspensions. International Journal of Multiphase Flow 37 (6), 609-619.

Meeker, S. P., Bonnecaze, R. T. & Cloitre, M. 2004. Slip and flow in soft particle pastes. Physical Review Letters 92 (19), 198302.

Messer, M. & Aidun, C. K. 2009. Main effects on the accuracy of Pulsed-Ultrasound-Doppler-Velocimetry in the presence of rigid impermeable walls. Flow Measurement and Instrumentation 20 (2), 85-94.

Mewis, J. & Moldenaers, P. 1999. Rheometry of complex fluids. Korea-Aust Rheol J 11 (4), 313-320.

Mewis, J. & Wagner, N. J. 2009. Thixotropy. Advances in Colloid and Interface Science 147, 214-227.

Mezger, T. G. 2006. The rheology handbook: for users of rotational and oscillatory rheometers. Vincentz Network GmbH & Co KG.

Michaely, R., Bachmann, A. H., Villiger, M. L., Blatter, C., Lasser, T. & Leitgeb, R. A. 2007. Vectorial reconstruction of retinal blood flow in three dimensions measured with high resolution resonant Doppler Fourier domain optical coherence tomography. Journal of Biomedical Optics 12 (4), 041213.

Moberg, T., Sahlin, K., Yao, K., Geng, S., Westman, G., Zhou, Q., Oksman, K. & Rigdahl, M. 2017. Rheological properties of nanocellulose suspensions: effects of fibril/particle dimensions and surface characteristics. Cellulose 24 (6), 2499-2510.

Mohtaschemi, M., Dimic-Misic, K., Puisto, A., Korhonen, M., Maloney, T., Paltakari, J. & Alava, M. J. 2014. Rheological characterization of fibrillated cellulose suspensions via bucket vane viscometer. Cellulose 21 (3), 1305-1312.

Møller, P. C., Mewis, J. & Bonn, D. 2006. Yield stress and thixotropy: on the difficulty of measuring yield stresses in practice. Soft matter 2 (4), 274-283.

Mooney, M. 1931. Explicit formulas for slip and fluidity. Journal of Rheology (1929-1932) 2 (2), 210-222.

Morrison, F. A. 2001. Understanding rheology. New York: Oxford University Press.

84

Murai, Y., Furuichi, N., Takeda, Y. & Tasaka, Y. 2012. Measurement of Fluid Flow. In Ultrasonic Doppler Velocity Profiler for Fluid Flow. Springer, 71-103.

Murakawa, H., Mori, M. & Takeda, Y. 2012. Ultrasonic Doppler Method. In Ultrasonic Doppler Velocity Profiler for Fluid Flow. Springer, 43-69.

Naderi, A. 2017. Nanofibrillated cellulose: properties reinvestigated. Cellulose 24 (5), 1933-1945.

Naderi, A. & Lindström, T. 2016. A comparative study of the rheological properties of three different nanofibrillated cellulose systems. Nordic Pulp & Paper Research Journal 31 (3), 354-363.

Naderi, A. & Lindström, T. 2015. Rheological measurements on nanofibrillated cellulose systems: A science in progress. Nova Science Publishers, Inc., New York , 187-202.

Naderi, A., Lindström, T. & Sundström, J. 2014. Carboxymethylated nanofibrillated cellulose: rheological studies. Cellulose 21 (3), 1561-1571.

Nazari, B., Kumar, V., Bousfield, D. W. & Toivakka, M. 2016. Rheology of cellulose nanofibers suspensions: Boundary driven flow. Journal of Rheology 60 (6), 1151-1159.

Nechyporchuk, O., Belgacem, M. N. & Bras, J. 2016. Production of cellulose nanofibrils: A review of recent advances. Industrial Crops and Products 93, 2-25.

Nechyporchuk, O., Belgacem, M. N. & Pignon, F. 2016. Current progress in rheology of cellulose nanofibril suspensions. Biomacromolecules 17 (7), 2311-2320.

Nechyporchuk, O., Belgacem, M. N. & Pignon, F. 2015. Concentration effect of TEMPO-oxidized nanofibrillated cellulose aqueous suspensions on the flow instabilities and small-angle X-ray scattering structural characterization. Cellulose 22 (4), 2197-2210.

Nechyporchuk, O., Belgacem, M. N. & Pignon, F. 2014. Rheological properties of micro-/nanofibrillated cellulose suspensions: wall-slip and shear banding phenomena. Carbohydrate Polymers 112, 432-439.

Nowak, M. 2002. Wall shear stress measurement in a turbulent pipe flow using ultrasound Doppler velocimetry. Experiments in Fluids 33 (2), 249-255.

Olmsted, P. D. 2008. Perspectives on shear banding in complex fluids. Rheologica Acta 47 (3), 283-300.

Osong, S. H., Norgren, S. & Engstrand, P. 2016. Processing of wood-based microfibrillated cellulose and nanofibrillated cellulose, and applications relating to papermaking: a review. Cellulose 23 (1), 93-123.

Ouriev, B. & Windhab, E. 2002a. Novel ultrasound based time averaged flow mapping method for die entry visualization in flow of highly concentrated shear-thinning and shear-thickening suspensions. Measurement Science and Technology 14 (1), 140.

Ouriev, B. & Windhab, E. J. 2005. Method for determining rheological parameters of a fluid.

Ouriev, B. & Windhab, E. J. 2002b. Rheological study of concentrated suspensions in pressure-driven shear flow using a novel in-line ultrasound Doppler method. Experiments in Fluids 32 (2), 204-211.

Ovarlez, G., Rodts, S., Chateau, X. & Coussot, P. 2009. Phenomenology and physical origin of shear localization and shear banding in complex fluids. Rheologica acta 48 (8), 831-844.

Pääkkö, M., Ikkala, O., Lindström, T., Ankerfors, M., Kosonen, H., Nykänen, A., Ahola, S., Osterberg, M., Ruokolainen, J., Laine, J., Larsson, P. T., KTH, Fiber- och polymerteknik & Skolan för kemivetenskap (CHE) 2007. Enzymatic hydrolysis combined with mechanical shearing and high-pressure homogenization for nanoscale cellulose fibrils and strong gels. Biomacromolecules 8 (6), 1934-1941.

Pedersen, C. J., Huang, D., Shure, M. A. & Rollins, A. M. 2007. Measurement of absolute flow velocity vector using dual-angle, delay-encoded Doppler optical coherence tomography. Optics Letters 32 (5), 506-508.

Petrich, M. P., Koch, D. L. & Cohen, C. 2000. An experimental determination of the stress–microstructure relationship in semi-concentrated fiber suspensions. Journal of Non-Newtonian Fluid Mechanics 95 (2-3), 101-133.

Pettersson, A. J., Wikström, T. & Rasmuson, A. 2006. Near wall studies of pulp suspension flow using LDA. Can. J. Chem. Eng. 84 (4), 422-430.

Pfund, D. M., Greenwood, M. S., Bamberger, J. A. & Pappas, R. A. 2006. Inline ultrasonic rheometry by pulsed Doppler. Ultrasonics 44, e477-e482.

Piao, D. & Zhu, Q. 2003. Quantifying Doppler angle and mapping flow velocity by a combination of Doppler-shift and Doppler-bandwidth measurements in optical Doppler tomography. Applied Optics 42 (25), 5158-5166.

Poelma, C., van der Mijle, R. M. E., Mari, J. M., Tang, M. X., Weinberg, P. D. & Westerweel, J. 2012. Ultrasound imaging velocimetry: Toward reliable wall shear stress measurements. European Journal of Mechanics - B/Fluids; Cardiovascular Flows 35 (0), 70-75.

Powell, R. L. 2008. Experimental techniques for multiphase flows. Physics of Fluids 20 (4), 040605-040605-22.

Powell, R. L., Maneval, J. E., Seymour, J. D., McCarthy, K. L. & McCarthy, M. J. 1994. Nuclear magnetic resonance imaging for viscosity measurements. Journal of Rheology 38 (5), 1465-1470.

Proskurin, S. G., He, Y. & Wang, R. K. 2003. Determination of flow velocity vector based on Doppler shift and spectrum broadening with optical coherence tomography. Optics Letters 28 (14), 1227-1229.

Proskurin, S. G., Sokolova, I. A. & Wang, R. K. 2003. Imaging of non-parabolic velocity profiles in converging flow with optical coherence tomography. Physics in Medicine and Biology 48 (17), 2907-2918.

Rabinowitsch, B. 1929. Über die viskosität und elastizität von solen. Zeitschrift für physikalische Chemie 145 (1), 1-26.

Rahman, M., Håkansson, U. & Wiklund, J. 2015. In-line rheological measurements of cement grouts: Effects of water/cement ratio and hydration. Tunnelling and Underground Space Technology 45, 34-42.

Raj, P., Mayahi, A., Lahtinen, P., Varanasi, S., Garnier, G., Martin, D. & Batchelor, W. 2016. Gel point as a measure of cellulose nanofibre quality and feedstock development with mechanical energy. Cellulose 23 (5), 3051-3064.

Ren, H., Brecke, K. M., Ding, Z., Zhao, Y., Nelson, J. S. & Chen, Z. 2002. Imaging and quantifying transverse flow velocity with the Doppler bandwidth in a phase-resolved functional optical coherence tomography. Optics Letters 27 (6), 409-411.

Ricci, S., Liard, M., Birkhofer, B., Lootens, D., Bruhwiler, A. & Tortoli, P. 2012. Embedded Doppler system for industrial in-line rheometry. IEEE transactions on ultrasonics, ferroelectrics, and frequency control 59 (7), 1395-1401.

Saarikoski, E., Saarinen, T., Salmela, J. & Seppälä, J. 2012. Flocculated flow of microfibrillated cellulose water suspensions: an imaging approach for characterisation of rheological behaviour. Cellulose 19 (3), 647-659.

Saarinen, T., Lille, M. & Seppälä, J. 2009. Technical aspects on rheological characterization of microfibrillar cellulose water suspensions. Annu Trans Nord Rheol Soc 17, 121-128.

Saito, T., Hirota, M., Tamura, N., Kimura, S., Fukuzumi, H., Heux, L. & Isogai, A. 2009. Individualization of nano-sized plant cellulose fibrils by direct surface carboxylation using TEMPO catalyst under neutral conditions. Biomacromolecules 10 (7), 1992-1996.

Salmela, J., Haavisto, S., Koponen, A., Jäsberg, A. & Kataja, M. 2013. Rheological characterization of micro-fibrillated cellulose fibre suspension using multi scale velocity profile measurements. Transactions of the 15th fundamental research symposium. The Pulp and Paper Fundamental Research Society, 495.

Salmela, J. & Kataja, M. 2005. Floc rupture and re-flocculation in turbulent shear flow. 13th, Fundamental Research Symposium, Cambridge, UK. , 35.

Schenker, M., Schoelkopf, J., Gane, P. & Mangin, P. 2018. Influence of shear rheometer measurement systems on the rheological properties of microfibrillated cellulose (MFC) suspensions. Cellulose 25 (2), 961-976.

Schmitt, J. M. 1999. Optical Coherence Tomography (OCT): a review. IEEE Journal on Selected Topics in Quantum Electronics 5 (4), 1205-1215.

Shafiei-Sabet, S., Martinez, M. & Olson, J. 2016. Shear rheology of micro-fibrillar cellulose aqueous suspensions. Cellulose 23 (5), 2943-2953.

Shiratori, T., Tasaka, Y., Oishi, Y. & Murai, Y. 2015. Ultrasonic velocity profiling rheometry based on a widened circular Couette flow. Measurement Science and Technology 26 (8), 085302.

Siró, I. & Plackett, D. 2010. Microfibrillated cellulose and new nanocomposite materials: a review. Cellulose 17 (3), 459-494.

Sochi, T. 2011. Slip at fluid-solid interface. Polymer Reviews 51 (4), 309-340.

Sorvari, A., Saarinen, T., Haavisto, S., Salmela, J., Vuoriluoto, M. & Seppälä, J. 2014. Modifying the flocculation of microfibrillated cellulose suspensions by soluble polysaccharides under conditions unfavorable to adsorption. Carbohydrate Polymers (0).

Spalding, D. B. 1961. A Single Formula for the Law of the Wall. Journal of Applied Mechanics 28 (3), 455.

Spence, K. L., Venditti, R. A., Rojas, O. J., Habibi, Y. & Pawlak, J. J. 2011. A comparative study of energy consumption and physical properties of microfibrillated cellulose produced by different processing methods. Cellulose 18 (4), 1097-1111.

Stifter, D. 2007. Beyond biomedicine: a review of alternative applications and developments for optical coherence tomography. Applied Physics B 88 (3), 337-357.

Sumida, M. 2013. Flow Properties of Wood Pulp Suspensions in Pipes. World Academy of Science, Engineering and Technology, International Journal of Mechanical, Aerospace, Industrial, Mechatronic and Manufacturing Engineering 7 (11), 2202-2206.

Sutera, S. P. & Skalak, R. 1993. The history of Poiseuille's law. Annual Review of Fluid Mechanics 25 (1), 1-20.

Swerin, A., Ödberg, L. & Lindström, T. 1990. Deswelling of hardwood kraft pulp fibres by cationic polymers. The effect on wet pressing and sheet properties. Nordic Pulp and Paper Research Journal .

Szkulmowska, A., Szkulmowski, M., Kowalczyk, A. & Wojtkowski, M. 2008. Phase-resolved Doppler optical coherence tomography-limitations and improvements. Optics Letters 33 (13), 1425-1427.

Taheri, H. & Samyn, P. 2016. Effect of homogenization (microfluidization) process parameters in mechanical production of micro-and nanofibrillated cellulose on its rheological and morphological properties. Cellulose 23 (2), 1221-1238.

Taheri, H. & Samyn, P. 2015. Rheological properties and processing of polymer blends with micro-and nanofibrillated cellulose. In Agricultural Biomass Based Potential Materials. Springer, 259-291.

Takeda, Y. 2012. Ultrasonic Doppler velocity profiler for fluid flow. Springer Science & Business Media.

Takeda, Y. 1986. Velocity profile measurement by ultrasound Doppler shift method. International Journal of Heat and Fluid Flow 7 (4), 313-318.

Takeuchi, J., Satake, S., Morley, N., Yokomine, T., Kunugi, T. & Abdou, M. 2005. PIV measurements of turbulence statistics and near-wall structure of fully developed pipe flow at high reynolds number. Proc. 6th International Symposium on Particle Image Velocimetry. , 21.

Tatsumi, D., Ishioka, S. & Matsumoto, T. 2002. Effect of Fiber Concentration and Axial Ratio on the Rheological Properties of Cellulose Fiber Suspensions. Journal of Society of Rheology, Japan 30 (1), 27-32.

Tezuka, K., Mori, M., Suzuki, T. & Kanamine, T. 2008. Ultrasonic pulse-Doppler flow meter application for hydraulic power plants. Flow Measurement and Instrumentation 19 (3), 155-162.

Tomlins, P. H. & Wang, R. K. 2005. Theory, developments and applications of optical coherence tomography. Journal of Physics D: Applied Physics 38 (15), 2519-2535.

Trasischker, W., Werkmeister, R. M., Zotter, S., Baumann, B., Torzicky, T., Pircher, M. & Hitzenberger, C. K. 2013. In vitro and in vivo three-dimensional velocity vector measurement by three-beam spectral-domain Doppler optical coherence tomography. Journal of Biomedical Optics 18 (11), 116010.

Turbak, A. F., Snyder, F. W. & Sandberg, K. R. 1983. Microfibrillated cellulose, a new cellulose product: properties, uses, and commercial potential. J. Appl. Polym. Sci.: Appl. Polym. Symp.;(United States). ITT Rayonier Inc., Shelton, WA.

Varanasi, S., He, R. & Batchelor, W. 2013. Estimation of cellulose nanofibre aspect ratio from measurements of fibre suspension gel point. Cellulose 20 (4), 1885-1896.

Vartiainen, J., Pöhler, T., Sirola, K., Pylkkänen, L., Alenius, H., Hokkinen, J., Tapper, U., Lahtinen, P., Kapanen, A. & Putkisto, K. 2011. Health and environmental safety aspects of friction grinding and spray drying of microfibrillated cellulose. Cellulose 18 (3), 775-786.

Wada, S., Kikura, H., Aritomi, M., Mori, M. & Takeda, Y. 2004. Development of pulse ultrasonic doppler method for flow rate measurement in power plant multilines flow rate measurement on metal pipe. Journal of Nuclear Science and Technology 41 (3), 339-346.

Wågberg, L., Decher, G., Norgren, M., Lindström, T., Ankerfors, M. & Axnäs, K. 2008. The build-up of polyelectrolyte multilayers of microfibrillated cellulose and cationic polyelectrolytes. Langmuir 24 (3), 784-795.

Wagner, M. & Horn, H. 2017. Optical coherence tomography in biofilm research: A comprehensive review. Biotechnology and bioengineering .

Wang, R. K. 2004. High-resolution visualization of fluid dynamics with Doppler optical coherence tomography. Measurement Science and Technology 15 (4), 725-733.

Wang, T., Wang, J., Ren, F. & Jin, Y. 2003. Application of Doppler ultrasound velocimetry in multiphase flow. Chemical Engineering Journal 92 (1), 111-122.

Wassenius, H. & Callaghan, P. T. 2005. NMR velocimetry studies of the steady-shear rheology of a concentrated hard-sphere colloidal system. The European Physical Journal E: Soft Matter and Biological Physics 18 (1), 69-84.

Werkmeister, R. M., Dragostinoff, N., Palkovits, S., Told, R., Boltz, A., Leitgeb, R. A., Gröschl, M., Garhöfer, G. & Schmetterer, L. 2012. Measurement of absolute blood flow velocity and blood flow in the human retina by dual-beam bidirectional Doppler fourier-domain optical coherence tomography. Investigative ophthalmology & visual science 53 (10), 6062-6071.

White, F. M. 2003. Fluid mechanics. Boston, MA: McGraw-Hill. ID: 1; U6: ctx_ver=Z39.88-2004&ctx_enc=info%3Aofi%2Fenc%3AUTF-8&rfr_id=info:sid/summon.serialssolu-tions.com&rft_val_fmt=info:ofi/fmt:kev:mtx:book&rft.genre=book&rft.ti-tle=Fluid+mechan-ics&rft.au=White%2C+Frank+M&rft.date=2003&rft.pub=McGraw-Hill&rft.isbn=007119911X&rft.externalDocID=22867&paramdict=en-US; M1: Book, Whole.

Wiklund, J. 2007. Ultrasound Doppler Based In-Line Rheometry-Development, Validation and Application. SIK-Svenska Livsmedelsinstitutet.

Wiklund, J., Shahram, I. & Stading, M. 2007. Methodology for in-line rheology by ultrasound Doppler velocity profiling and pressure difference techniques. Chemical Engineering Science 62 (16), 4277-4293.

Wiklund, J. & Stading, M. 2008. Application of in-line ultrasound Doppler-based UVP–PD rheometry method to concentrated model and industrial suspensions. Flow Measurement and Instrumentation 19 (3), 171-179.

Witten, T. A. 1990. Structured fluids. Physics Today 43, 21-28.

Wojtkowski, M. 2010. High-speed optical coherence tomography: basics and applications. Applied Optics 49 (16), D30-D61.

Wu, L. 2004. Simultaneous measurement of flow velocity and Doppler angle by the use of Doppler optical coherence tomography. Optics and Lasers in Engineering 42 (3), 303-313.

Wunderlich, T. & Brunn, P. 2000. A wall layer correction for ultrasound measurement in tube flow: comparison between theory and experiment. Flow Measurement and Instrumentation 11 (2), 63-69.

Xi, C., Marks, D. L., Parikh, D. S., Raskin, L. & Boppart, S. A. 2004. Structural and functional imaging of 3D microfluidic mixers using optical coherence tomography. Proceedings of the National Academy of Sciences of the United States of America 101 (20), 7516-7521.

Xia, S., Huang, Y., Peng, S., Wu, Y. & Tan, X. 2017. Robust phase unwrapping for phase images in Fourier domain Doppler optical coherence tomography. Journal of Biomedical Optics 22 (3), 036014.

You, J., Du, C., Volkow, N. D. & Pan, Y. 2014. Optical coherence Doppler tomography for quantitative cerebral blood flow imaging. Biomedical optics express 5 (9), 3217-3230.

You, J., Li, A., Du, C. & Pan, Y. 2017. Volumetric Doppler angle correction for ultra-high-resolution optical coherence Doppler tomography. Applied Physics Letters 110 (1), 011102.

Zhang, L., Batchelor, W., Varanasi, S., Tsuzuki, T. & Wang, X. 2012. Effect of cellulose nanofiber dimensions on sheet forming through filtration. Cellulose 19 (2), 561-574.

Zimmermann, T., Bordeanu, N. & Strub, E. 2010. Properties of nanofibrillated cellulose from different raw materials and its reinforcement potential. Carbohydrate Polymers 79 (4), 1086-1093.

ORIGINAL PAPERS

I

ACCURATE VELOCITY MEASUREMENTS OF BOUNDARY-LAYER FLOWS USING DOPPLER OPTICAL COHERENCE TOMOGRAPHY

by

Sanna Haavisto, Juha Salmela & Antti Koponen, 2015

II

RHEOLOGICAL CHARACTERIZATION OF MICROFIBRILLATED CELLULOSE SUSPENSION USING OPTICAL COHERENCE TOMOGRAPHY

by

Sanna Haavisto, Juha Salmela, Ari Jäsberg, Tapio Saarinen,
Anni Karppinen & Antti Koponen , 2015

Rheological characterization of microfibrillated cellulose suspension using optical coherence tomography

SANNA HAAVISTO, JUHA SALMELA, ARI JÄSBERG, TAPIO SAARINEN,
ANNI KARPPINEN, AND ANTTI KOPONEN

ABSTRACT: Fiber suspensions, such as microfibrillated cellulose, are a challenge for conventional rheometers to measure. This is because rheometers have small flow channel dimensions that can restrict flocculation. Often, questionable assumptions are also made about the fluid behavior in the gap. A pipe rheometer and ultrasound velocity profiling-pressure difference (UVP-PD) concept can be used, by which the real flow behavior is used for the rheological analysis of the bulk properties of the suspension. Unfortunately, the resolution of UVP is too low for studying near-wall phenomena, such as the lubrication layer, that are often very important for understanding the rheology and to upscale the results to industrial flows. To address this problem, we have widened the UVP-PD concept with optical coherence tomography measurements. This enables us to measure the bulk and wall-layer behavior simultaneously. Our results demonstrate the benefits of having direct, detailed measurement of the velocity profile inside the rheometer.

Application: Velocity profiling in the near-wall region can lead to better understanding of the rheology of complex fluids. This information would be invaluable in flow control and numerical simulations of flows of complex fluids, such as microfibrillated cellulose (MFC).

Cellulose fibers generally form an opaque flocculated suspension with high viscosity, even at low mass concentrations. Conventional rheometers often fail to produce reliable information for these suspensions because the dimension of the system (e.g., the gap between walls) is typically very small. In addition, interpretation of the measured data is usually based on an assumed flow behavior of the fluid (e.g., Couette-type flow and no-slip boundary condition) that might not be valid. To address these problems, we previously introduced a laboratory-scale pipe rheometer that can be used for any complex fluid, thus it is especially useful for studying fibrous materials [1]. The rheological characterization in the pipe rheometer is based on the well-established ultrasound velocity profiling (UVP) and pressure difference (PD) concept, which has been widely used to study rheological properties of various model and industrial fluids [2-5].

In the UVP-PD method, the rheological analysis is based on a combination of UVP and PD measurements [6,7]. The real flow behavior based on direct experimental observation can thus be used as the basis for interpreting and analyzing the results from the rheometric measurements – no assumptions of the velocity profile are needed. Moreover, the pipe rheometer enables the use of realistic flow geometries where a suspension can reach its steady state, but collective phenomena such as flocculation are not restricted by the system size.

In the data analysis of the UVP-PD method, the local shear rate $\dot{\gamma}(r)$ at each distance r from the tube wall is obtained directly from the measured velocity profile. The local shear stress is:

$$\tau(r) = \tau_w(1 - r/R) \tag{1}$$

where R is the pipe radius and $\tau_w = \Delta p/2RL\pi$ is the shear stress at the pipe wall (here Δp is the pressure loss and L is the pipe length). The local shear viscosity (**Fig. 1a**) is then:

$$\mu(r) = \tau(r)/\dot{\gamma}(r) \tag{2}$$

The yield stress τ_y of the fluid is obtained from the measured velocity profile by using this formula:

$$\tau_y = \tau_w(1 - R_0/R) \tag{3}$$

where R_0 is the radial position, estimated from the velocity profiles, at which the fiber plug brakes (**Fig. 1b**) [1].

The flow behavior of fiber suspensions, however, cannot be understood from bulk properties alone. A common phenomenon that occurs in fiber suspension flows is the drag reduction, which refers to a case where the frictional loss in a channel suddenly levels off or even decreases with increasing flow rate (**Fig. 2**) [1]. Qualitatively, the origin of this effect can be traced back to a spontaneous formation of a concentration gradient or a fiber-free lubrication layer near the channel

MICROFIBRILLATED CELLULOSE
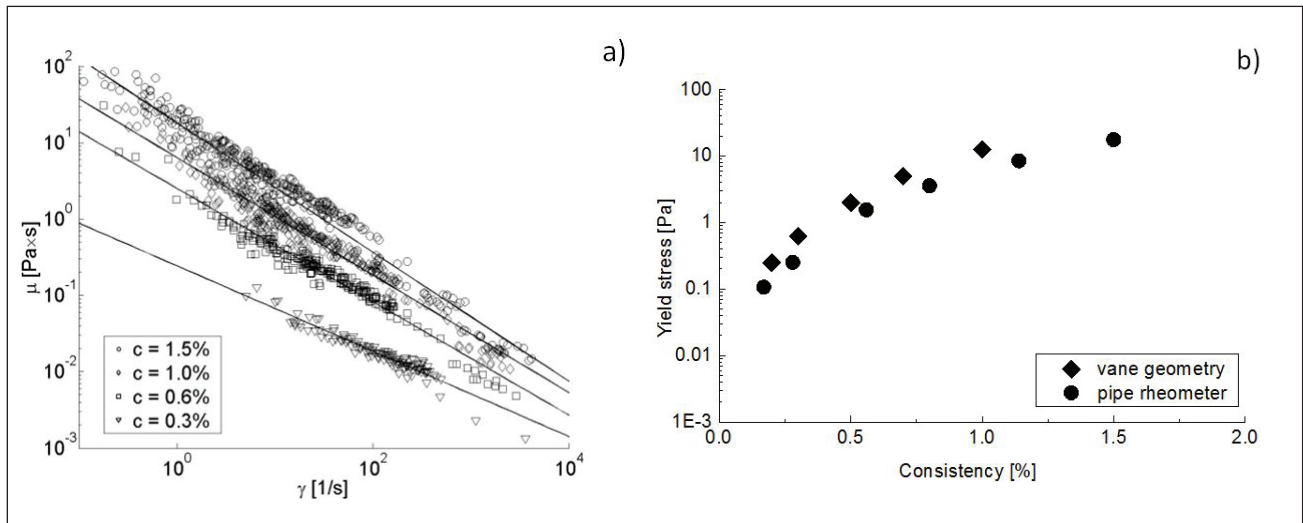
1. (a) Viscosities for different concentrations of microfibrillated cellulose (MFC). The measurements have been performed with the pipe rheometer. (b) Yield stress of a MFC suspension as a function of concentration measured with the pipe rheometer and a rotational rheometer equipped with vane geometry. [1]

wall [8,9]. However, the phenomenon is still poorly understood, posing a problem in flow control and in numerical simulations of fiber suspension flows. Because of its nonlinear behavior, the lubrication layer may create instabilities to the flow. Without accurate knowledge about these dynamics, it is impossible to build control schemes based on physical modeling. The existence of a lubrication layer also affects the results of traditional rheometer measurements, often making them unreliable.

A key reason for developing more reliable material models for fiber suspension flows is to gain more realistic understanding of the boundary layer behavior of such fluids. So far, this has not been feasible because of the lack of experimental

techniques that would allow direct measurement of flows and structures of complex, opaque fluids in the immediate vicinity of the wall (typically, within a few tens of micrometers from the wall). Generally, there are very few non-invasive measurement methods available that can be used in measuring the velocity field or the structure of opaque heterogeneous fluids, such as fiber suspensions. Two commonly known methods are magnetic resonance imaging [10] and UVP [11]. More recently, optical coherence tomography (OCT) has been developed and introduced for this purpose [12-14]. OCT is a non-invasive optical imaging technique capable of real-time access of structural data and velocity information in an opaque scattering medium. The most important advantages of OCT as compared to other methods are its high spatial and temporal resolution and its ability to provide reliable data very close to solid boundaries.

We have recently equipped the pipe rheometer with the UVP and the OCT techniques [8,15]. This enables the measurement of the whole velocity field in the pipe (including the close wall area). With such a setup, we get all relevant rheological information simultaneously from a single apparatus: bulk properties from UVP and boundary layer behavior from OCT (**Fig. 3**).

Because of some intriguing characteristics of microfibrillated cellulose (MFC) suspensions (e.g., high surface area, high aspect ratio, and ability to form a very rigid network), it has become a considerable part of research in material technology during the past few decades [16]. The rheological properties of MFC suspensions also have been under lively investigation [8,17-20]. In earlier work, we presented indirect evidence of intricate flow phenomena for MFC, such as instability, flocculation, and wall slip inside a rotational rheometer [21,22]. With OCT, we can now take explicit snapshots for the structure of MFC in such a setup. The reported results have
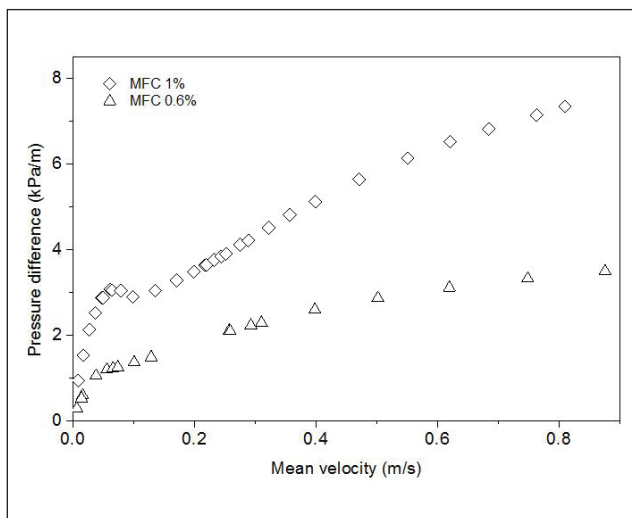
2. Pressure loss as a function of mean velocity for 0.6% MFC and 1.0% MFC. The creation of the lubrication layer (leveling of the pressure loss) is clearly seem for 1.0% MFC at v = 0.1 m/s. The pipe diameter in these experiments was 16 mm. [1]
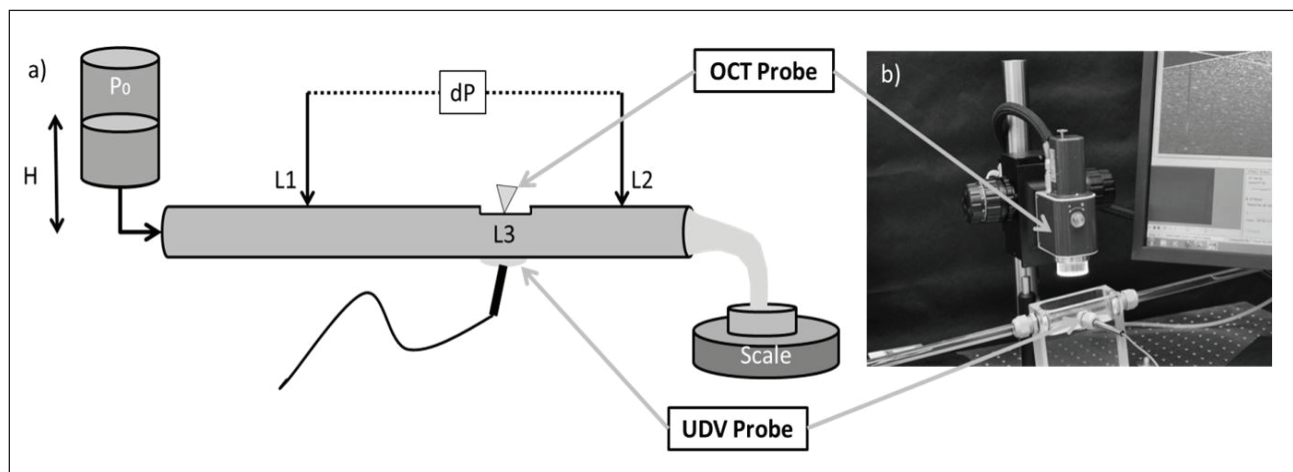
3. (a) Schematic illustration of the measurement setup of the new pipe rheometer. (b) Image of the optical coherence tomography (OCT) measurement setup.

shown strong shear thinning behavior (i.e., a decrease in viscosity with increasing shear rate) for MFC suspensions. We show that the generally used assumption of a stationary nearly linear velocity profile, valid for water and other simple fluids, often is not appropriate here.

MATERIALS AND METHODS

OCT and UVP

The OCT device used in this study was a Spectral Domain OCT (Telesto SD-OCT, Thorlabs; Newton, NJ, USA). In a standard OCT setup, a light beam of low coherence is emitted from a super luminescent LED light source and split into the sample arm and the reference arm of a Michelson interferometer. The backscattered interference pattern can be analyzed for sample scattering index from different depths and further processed to construct slice images from a series of adjacent lateral scans. In Doppler OCT mode, the adjacent scans are used to acquire the velocity information by use of the Kasai autocorrelation function [23]. The resolution and frame rate of the slice images are determined by the light beam properties (central wavelength, coherence length, and dimensions) and the radial/axial scan rate. With the current device, the central wavelength was 1325 nm, radial resolution in water was about 5 μm, and the lateral resolution was 15 μm. Three discrete values, 5.5 kHz, 28 kHz, and 91 kHz, were available for the radial scan rate.

UVP is a method for measuring an instantaneous 1-dimensional velocity profile [11]. The method is based on detecting the Doppler shift frequency information echoed by particles moving with the flow. The actual velocity of the moving particles is calculated from the cross-correlation between the echoes from sequential pulses. The location of the particles is acquired with the time-of-flight method using the known velocity of sound. In the present study, a DOP2000 velocimeter (Signal Processing S.A.; Savigny, Switzerland) equipped with an 8 MHz ultrasound transducer was used. The angle between the transducer axis and the pipe wall was 74°.

The ultrasound pulse repetition frequency was varied between 500 Hz and 1000 Hz to exploit the full velocity resolution range. In all measurements, eight consecutive pulse emissions were used to calculate a single velocity value in each sampled depth locations.

Rheological characterization in pipe flow

The measurement unit in the pipe rheometer consists of a 1500 mm long and 8.6 mm inner diameter optical grade glass pipe with 2.5 mm wall thickness. The flow can be driven by gravity or pressurized air to allow for a steady, pulsation-free flow. The mass flow rate is recorded with a laboratory scale and the corresponding pressure loss with pressure difference sensors (Rosemount 3051 and 2051, Emerson Process Management; Shakopee, MN, USA).

The MFC suspension properties were analyzed in similar manner as with UVP alone but now the combined velocity profile (UVP and OCT) was used [1]. The velocity profiles were obtained by a sequence of measurements with increasing flow rate. The region of steady flow was determined from the measurement data and analyzed for average pressure loss and mass flow rate. With UVP and OCT, a set of data was recorded for each flow rate, and the final mean velocity profile was calculated as an average of several instantaneous velocity profiles.

Rheological characterization with rheometer

Stepped flow shear measurements (flow curves) were carried out at room temperature (23°C-25°C) using a dynamic rotational rheometer (AR-G2, TA Instruments; New Castle, DE, USA) equipped with concentric cylinders geometry. We used a standard TA Instruments hard anodized aluminum bob with radius of 14.00 mm and height of 42.00 mm. The outer geometry was a custom-made transparent polymethyl methacrylate (PMMA) cup with radius of 14.87 mm. The flow curves were measured starting from high shear rate (i.e., from 600 to 0.1 s^{-1}) using 15 s point time.

MICROFIBRILLATED CELLULOSE
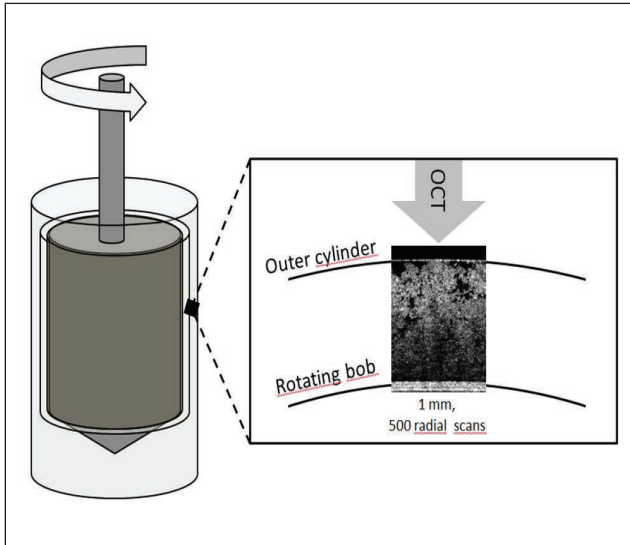
4. Schematic illustration of the concentric cylinder geometry together with the OCT measurement principle.
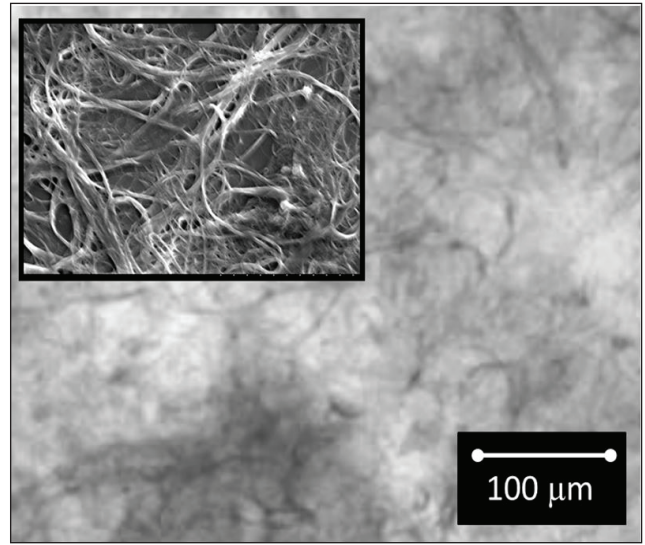
5. Microscopic images of Masuko ground microfibrillated cellulose and Celish KY-100G (upper left corner).

In the stepped flow measurements, OCT was used for imaging the suspension in the radial direction from the transparent outer geometry boundary to the inner geometry boundary (**Fig. 4**). In the higher shear rate range ($\dot{\gamma} > 50$ 1/s), OCT was set to acquire sequential scans from a fixed radial position with the highest available scan rate (i.e., 91 kHz). At the lower shear rates, OCT parameters were selected to allow for detailed visual observation of the MFC suspension structure. A set of 2-dimensional slice images consisting of 500 radial scans across a lateral width of 1 mm were recorded at each shear rate.

Microfibrillated celluloses

The microfibrillated cellulose type used in the pipe rheometer experiments was Celish KY-100G (Daicel Chemical Industries; Himeji, Japan), a commercial product made from purified wood pulp (**Fig. 5**). The average length and diameter of Celish fibers reported by Tatsumi et al. [24] are 350 μm and 15 μm, respectively. The size distribution of the fibrils, however, ranges from microscale to nanoscale. For the experiments, the pulp sample was diluted with deionized water to mass concentrations of 0.4%, 1.0%, and 1.7% under high intensity mixing. The pulp temperature during the measurements was 20±1°C.

The microfibrillated cellulose sample for the rotational rheometer measurements was prepared from bleached kraft birch pulp and ground three times with a supermasscolloider (Masuko Sangyo; Kawaguchi, Japan). Before grinding, the pulp was changed to its sodium form and washed with deionized water until the electrical conductivity was less than 20 μS/cm. The grinding consistency was 1.9%. The sample was diluted with MilliQ water to a mass concentration of 1% and mixed with a propeller mixer for 10 min.

RESULTS

Pipe rheometer

Verification with water

The correct operation of the measurement setup and the consistency of the measured OCT and UVP velocity data were verified with water in laminar and in turbulent flow conditions. This can be done very accurately; the flow of water in a straight smooth tube with circular cross section is well known. **Fig. 6** shows the measured results together with the standard profile correlations [25]. Here, nondimensional wall unit notations for (dimensionless) distance from the pipe wall y^+ and (dimensionless) flow velocity u^+ are used in the following equation:

$$y^+ = \frac{yu^*}{\nu}, \ u^+ = \frac{u}{u^*}, u^* = \left(\frac{\tau_w}{\rho}\right)^{\frac{1}{2}} \tag{4}$$

where y is the distance from the wall, ν is the kinematic viscosity of water, u is the fluid velocity, ρ is the fluid density, τ_w is the shear stress at the wall, and u^* is friction velocity.

The results in Fig. 6 show that there is very good agreement between the experimental data and the theoretical prediction in the Reynolds number range of 60–10000 (i.e., flow velocity range of $7 \times 10^{-3} - 1.2$ m/s). The profiles measured with both OCT and UVP follow the linear law of the wall ($u^+ = y^+$) and the logarithmic law ($u^+ = \frac{1}{0.40} \ln y^+ + 5.5$) quite accurately. Figure 6 also shows the Spalding profile [26], which smoothly interpolates between the two preceding formulae.

The spatial measurement range of OCT covers the viscous sublayer and part of the buffer layer. It closely follows the theoretical profile over more than two orders of magnitude in y^+. To our knowledge, the data measured with OCT reach smaller values of y^+ (i.e., are measured closer to the wall) than
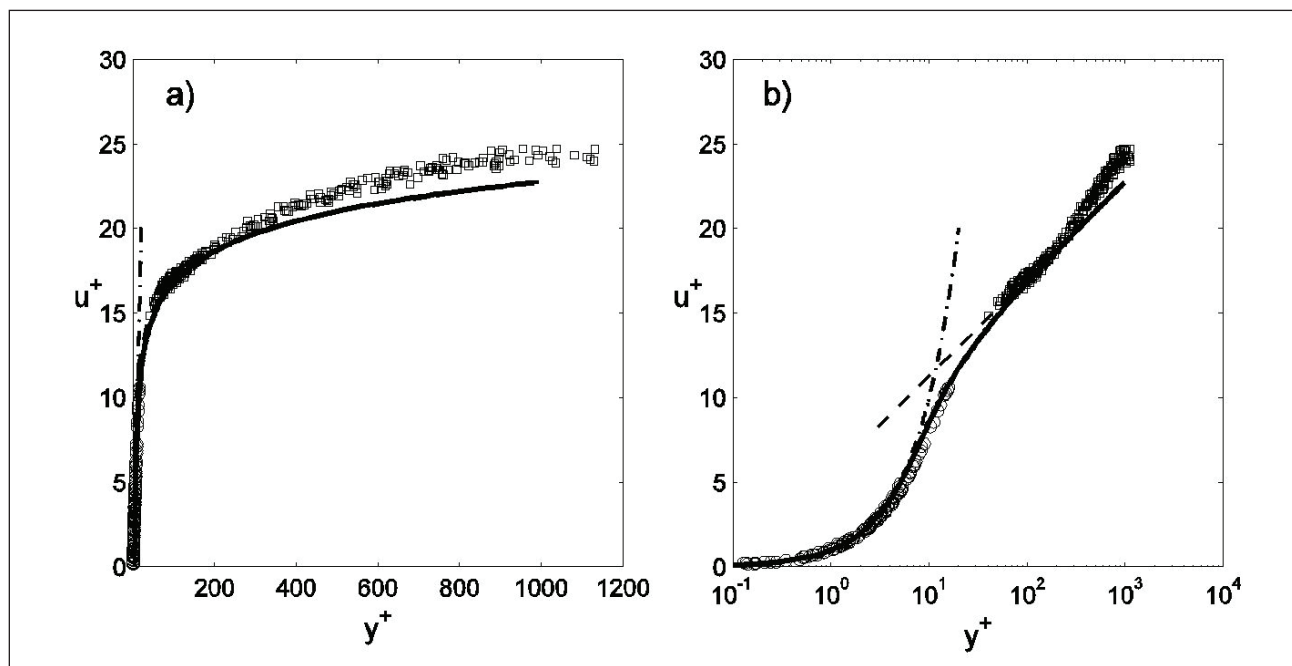
6. Several velocity profiles of laminar and turbulent pipe flows of water measured with OCT (circles) and ultrasound velocity profiling (UVP; squares) in dimensionless variables y^+ and u^+ plotted in (a) linear scales and (b) with logarithmic y^+ scale. The dash-dotted line indicates the linear viscous sublayer profile and the dashed line is the logarithmic buffer layer profile. The solid line represents the Spalding inner layer correlation [26] from which the measured velocity profiles are seen to separate (correctly) at y^+ ~300.

has been reported before for such a small pipe ($D = 8.6$ mm).

Because the OCT results can be obtained very close to the wall, the shear stress at the wall can be calculated by extrapolating the gradient of the OCT velocity profiles to the pipe wall. In other words, instead of a direct measurement, the pressure loss can be obtained from the equation:

$$\Delta p_{OCT} = \pi D L \tau_{OCT} \tag{5}$$

where

$$\tau_{OCT} = \mu_{\text{water}} \left(\frac{dv(r)}{dr} \right)_{r \to R} \tag{6}$$

Given the shear stress at the wall, the friction factor f for water using the combination of volumetric flow and OCT measurements can be calculated as

$$f(\text{Re}) \equiv \frac{\Delta p}{\frac{L}{D} \frac{\rho V^2}{2}}, \ \text{Re} = \frac{\rho V D}{\mu} \tag{7}$$

Where Δp is the pressure loss, L is the pipe length, ρ is the fluid density, D is the pipe diameter, μ is the fluid viscosity, and Re is the Reynolds number.

In **Fig. 7**, the measured friction factor f is shown for the Reynolds number range of 70-10000 for water flowing in a straight tube with a circular cross-section and smooth walls.
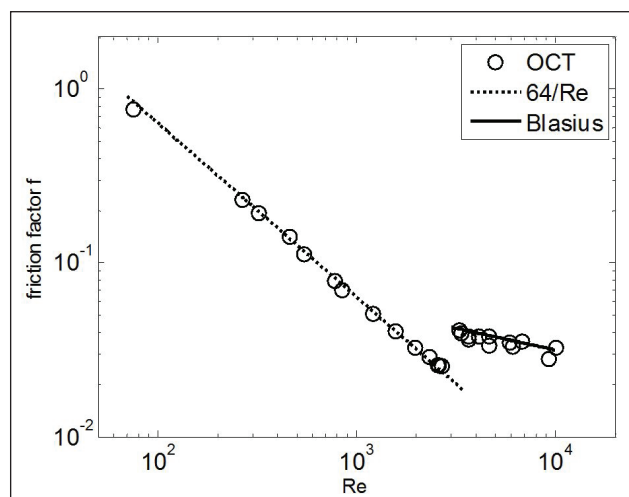
7. The friction factor of pipe flow measured with optical coherence tomography for water. The dashed line shows the theoretical prediction for the laminar region, and the solid line is the prediction for turbulent flow given by the Blasius equation.

The results are seen to correlate very well with the theoretical predictions [25].

Velocity profile and structure of MFC in pipe flow

After the verification measurements, the system was used for measuring the rheological properties of MFC suspensions. **Figure 8** shows an example of the combined mean velocity

MICROFIBRILLATED CELLULOSE
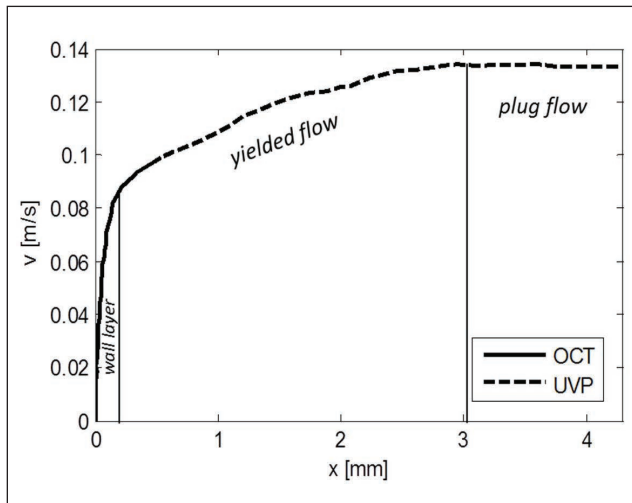
8. The velocity profile for a pipe flow (diameter 8.6 mm) of 0.4% MFC measured simultaneously by OCT and UVP.

profiles for 0.4% MFC in a pipe with diameter of 8.6 mm. UVP data from very close to the pipe wall have been omitted from the profile because of the known measurement limitations [5]. The agreement between the OCT and UVP velocity profiles is excellent, as with water, but now the spatial measurement range of the two measurements is overlapping. The combined profile shows three different flow regions: plug flow, yielded flow, and a wall layer. In this case, the thickness of the wall layer is approximately 200 μm and more than 60% of the maximum velocity is reached within that distance. Any traditional measurement technique would fail to measure the wall layer and it would be interpreted as a wall slip of 60%.

The effective concentration fields of suspensions can be obtained from the back-scattering intensity measured by OCT. The origin of the apparent wall slip can now be seen in **Figs. 9** and **10**. In Fig. 9 we see a 3-dimensional OCT image of non-flowing 0.4% MFC suspension in the pipe. The image was taken instantly after the flow was stopped. A fiber-poor layer is clearly visible close to the pipe wall (dark areas).

Figure 10 shows an instantaneous and an average concentration OCT image of MFC suspension flowing near the tube wall. The OCT images are constructed as the spatial distribution of the back-scattering index of light which, in turn, correlates with the concentration of the scattering particles. The scattering intensity profile (effective concentration) and the velocity profile are overlaid with the grayscale images. The concentration profile shows an approximately 200 μm thick layer of increasing concentration close to the wall. The existence of a wall concentration profile indicates that the fluid viscosity must change with the distance from the wall. There is a large variation in the velocity gradient close to the wall, although the shear stress is practically constant in such a narrow area. The viscosity profile calculated from Eq. (2) is shown in Fig. 10b. It shows that, near the wall, the viscosity is very close to that of water. This suggests that in the vicinity of the wall, there is a layer of almost pure water. The viscosity increases exponentially until it saturates to its bulk value at approximately 200 μm from the wall. To our knowledge, these are the first examples on such detailed experimental data on the fiber suspension properties very close to the wall.

Figure 11a shows the viscosity of the 0.4% suspension at the wall as a function of the wall shear stress. The wall viscosity decreases with increasing wall shear stress and
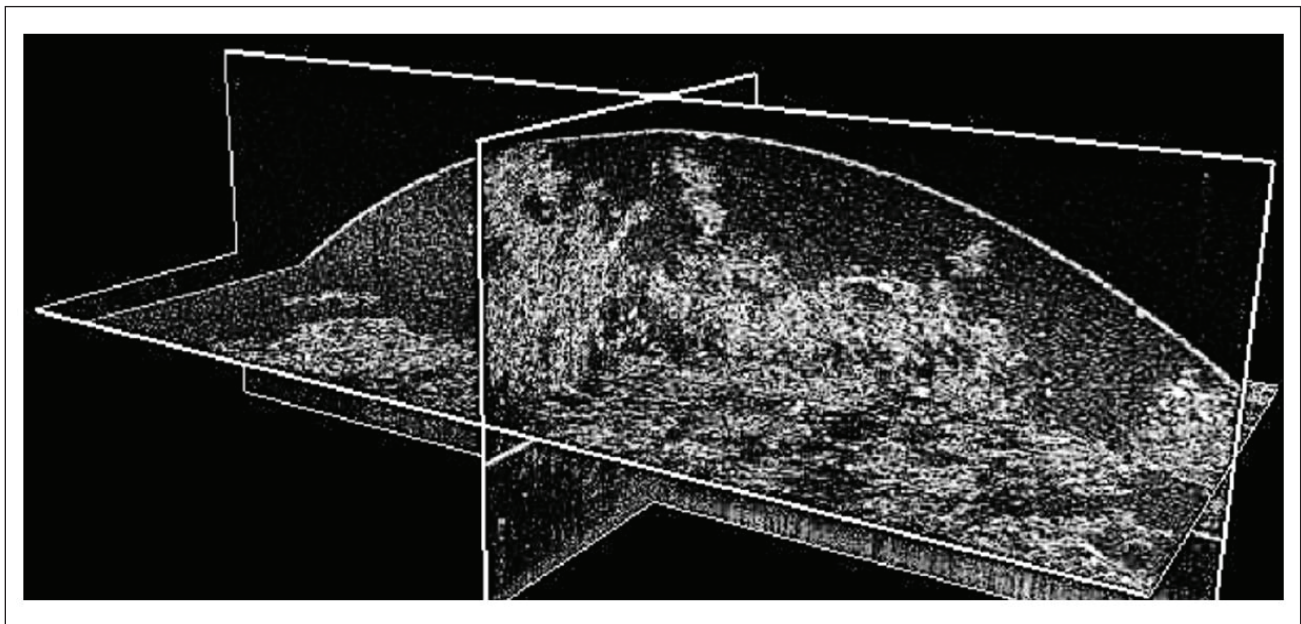
9. A 3-dimensional OCT image of 0.4% MFC in a pipe with a diameter of 8.6 mm. An almost fiber-free layer (black areas) is clearly visible close to the pipe walls.
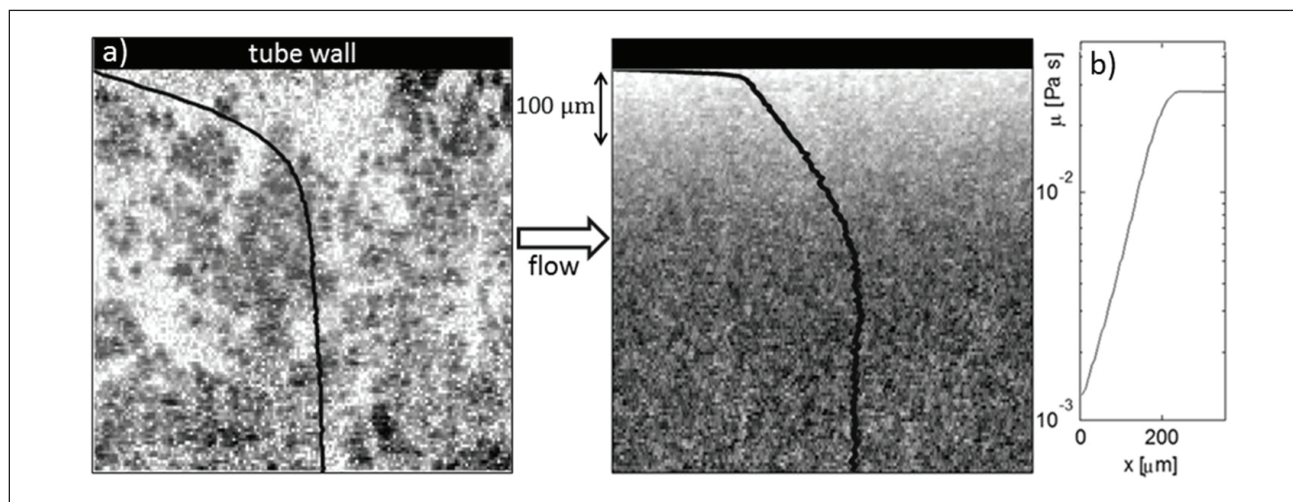
10. A 0.4% MFC suspension flowing near the tube wall. On the left an instantaneous image and on the right an average of 200 independent images acquired with the OCT techniques are shown. The grey-scale values in the image represent the local value of the optical back-scattering index, light color corresponding to low index value. The velocity profile and the scattering intensity (effective concentration) of the suspension are shown with black curves. On the right the viscosity profile close to the wall is shown.
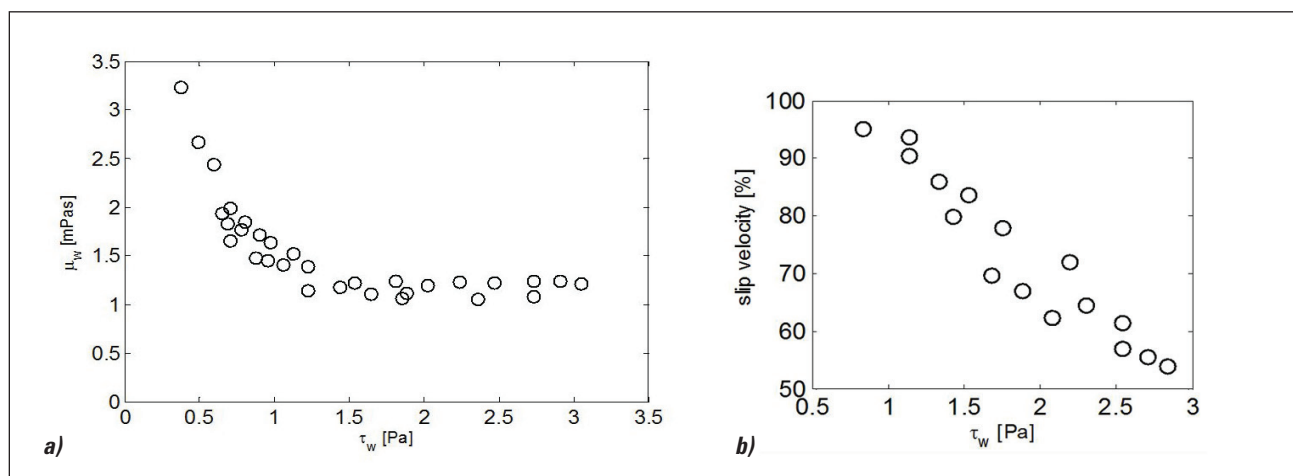
11. (a) The viscosity μ_w of the 0.4% MFC suspension at the wall as the function of wall shear stress τ_w. The wall viscosity decreases with increasing wall shear stress and saturates to $\mu_w \sim 1.2 \mu_{water}$ when $\tau_w \sim 2\tau_y$ (approximately twice the yield stress; see Fig. 1b). (b) The contribution of slip velocity to the total volumetric flow as a function of the wall shear stress for 0.4% MFC.

saturates to a 20% higher value than the viscosity of water when the wall shear stress is approximately twice the yield stress. Similar behavior is observed for the consistencies of 1.0% and 1.7% (**Fig. 12**). In Fig. 11b, the contribution of the slip velocity to the total volumetric flow is shown as the function of the wall shear stress for 0.4% MFC. The slip velocity completely dominates the flow with the smallest wall shear rates and appears to decrease linearly when the wall shear stress increases. Salmela et al. provide a more careful analysis of the wall layer [8].

Rotational rheometer

Figure 13 shows the flow curves for a 1% MFC suspension. MFC suspensions typically show strong shear thinning behavior and flow curves often include a plateau between the

low and high shear rate regions. This region, called the transition region or Newtonian plateau, is well known and reported for MFC [16-20]. The Newtonian plateau has been observed with different measuring geometries, including plate-and-plate [19,20] and concentric cylinders [16] geometries. Although not thoroughly researched, the reason for the transition at intermediate shear rates has been proposed to be the result of structural changes [19,20]. In this section, we aim to bring more insight on interpreting the rheometer data using OCT measurements.

Low shear rate and transition regions

Figure 14 shows the suspension structure and velocity profiles at three different apparent shear rates. Here, the velocity profiles were determined by tracking the horizontal
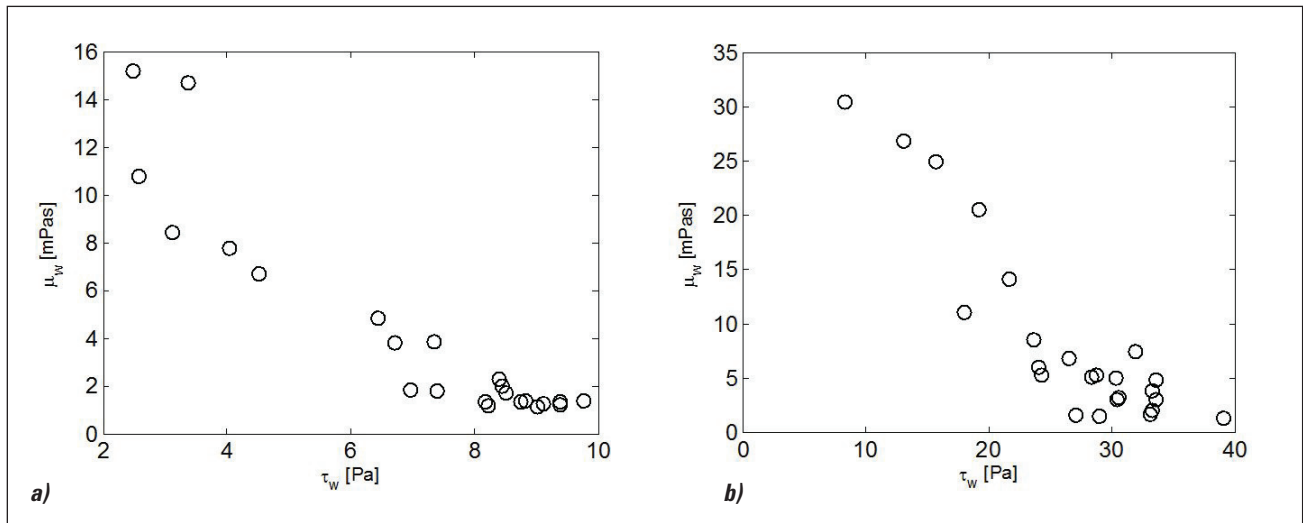
12. (a) The viscosity μ_w of the 1.0% MFC suspension at the wall as the function of wall shear stress τ_w. The wall viscosity decreases with increasing wall shear stress and saturates to $\mu_w \sim 2\,\mu_{water}$ when $\tau_w \sim 2\tau_y$ (approximately twice the yield stress). (b) The viscosity μ_w of the 1.7% MFC suspension at the wall as the function of wall shear stress τ_w. The wall viscosity decreases with increasing wall shear stress and appears to saturate when $\tau_w \sim 2\tau_y$.
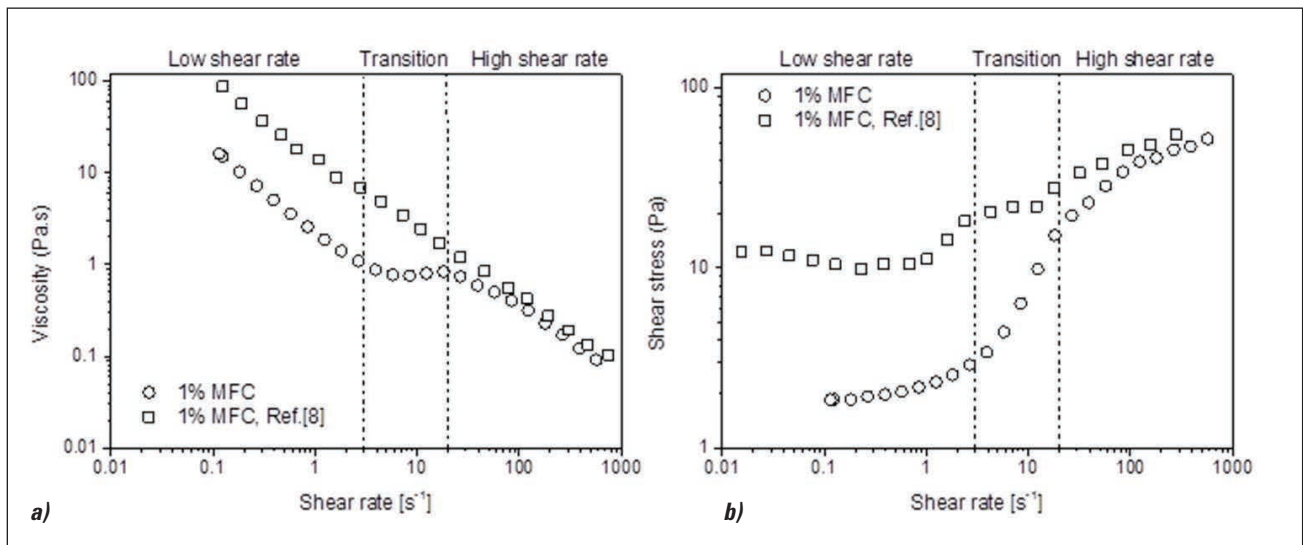
13. Viscosity and shear stress as a function of apparent shear rate for 1% MFC suspension. The viscosity is calculated assuming an ideal (linear) velocity profile in the rheometer gap. Lavoine et al. [16] preformed measurements after pre-shearing from low shear rates to high shear rates.

displacement of the MFC flocs between sequential structure images using an optical flow algorithm [21]. Results show that the fibers are not evenly distributed in the gap, and the velocity profile is not linearly decreasing to zero toward the outer wall, as is normally assumed when calculating the viscosity. So, despite looking reasonable, the flow curve cannot be used for analyzing the bulk properties of MFC — at least not in this flow region. It would be very difficult to make such a conclusion using the rheometer data alone. However, analysis of the values of shear stress can in many cases help here. We have found that for MFC with concentrations of 0.1%-2%, the shear stress is often approximately constant or increases very

slowly in the low shear rate region [16,21]. The (wall) shear stress is then almost independent of the rotation speed of the inner cylinder. This strongly indicates that the rheometer data might be dominated by boundary layer phenomena, not by the bulk properties of MFC. This has been discussed in more detail by Saarikoski et al. [21].

The MFC viscosity (μ) is often characterized with the power law model:

$$\mu = K\dot{\gamma}^{n-1} \tag{9}$$

where K is the consistency index and n is the flow index. If
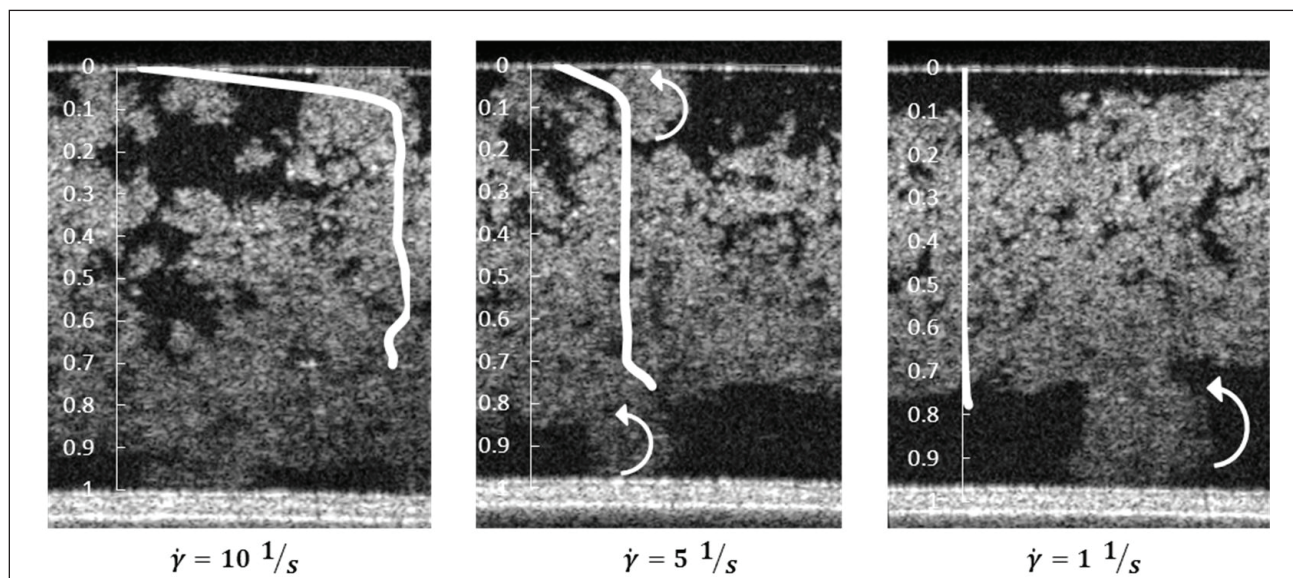
14. Different flow regimes for 1% MFC in a cylindrical rotational rheometer: (a) Complete slip on the stationary wall. (b) Slip and rolling flocs on both walls. (c) Rolling flocs on the moving wall. The gap is 1.0 mm. The average velocity profiles are marked with a white line.
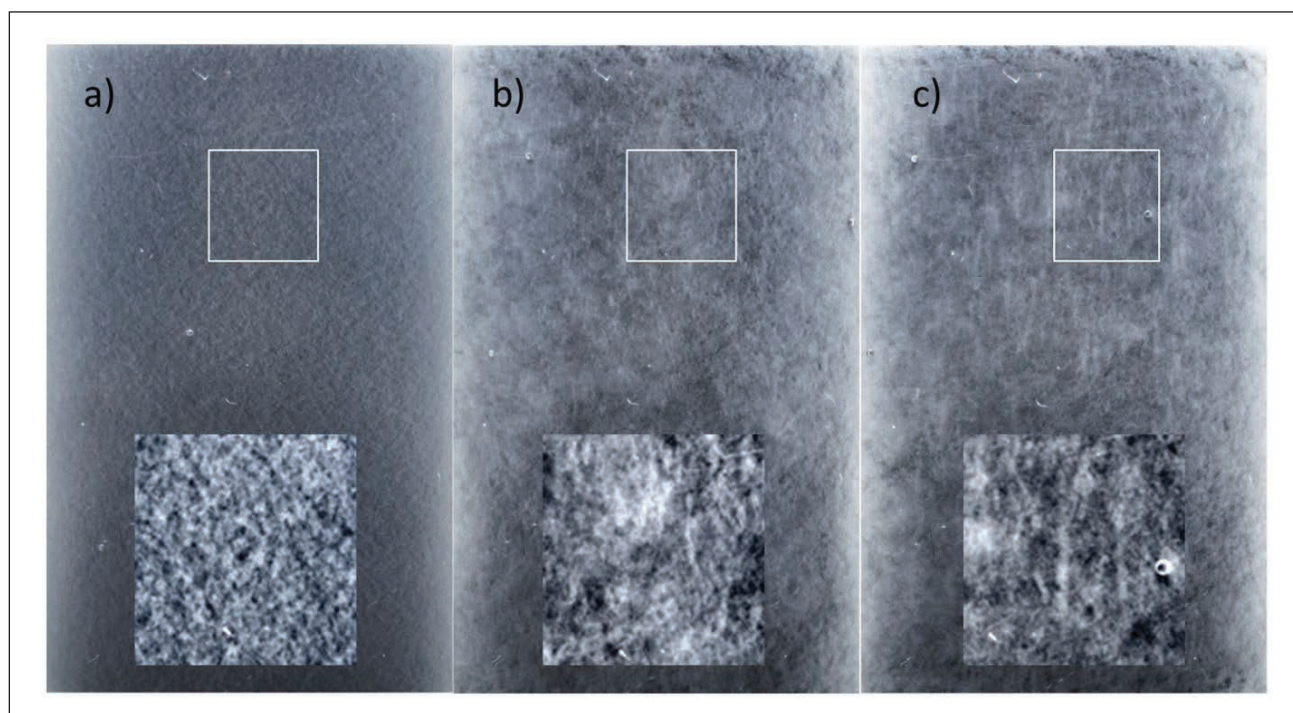
15. MFC suspensions in the rheometer gap at different shear rates: (a) 108 s⁻¹, (b) 11 s⁻¹, and (c) 1 s⁻¹.

the shear stress is almost constant, the flow index n is close to 0. It seems that flow index values smaller than ~0.2 with the rheometer data are less reliable [15]. This is also the case in Fig. 13, where n gets values 0.0 and 0.16 in the low shear rate region.

Figure 15 shows floc structures for 1% MFC suspension during the flow curve measurements photographed through the transparent outer cylinder. The photographs depict three

different regions, showing that at high shear rates, the flocs are small and homogeneous. During the transition region (Fig. 15b), the separate flocs start to attach to each other in the decelerating flow, because the shearing is not sufficient to break the larger flocs. In our earlier study [16], we saw similar structures with increasing shear rate curve, meaning that the continuous network is breaking in the transition region. At the low shear rate region, the structure remains uneven and co-

MICROFIBRILLATED CELLULOSE
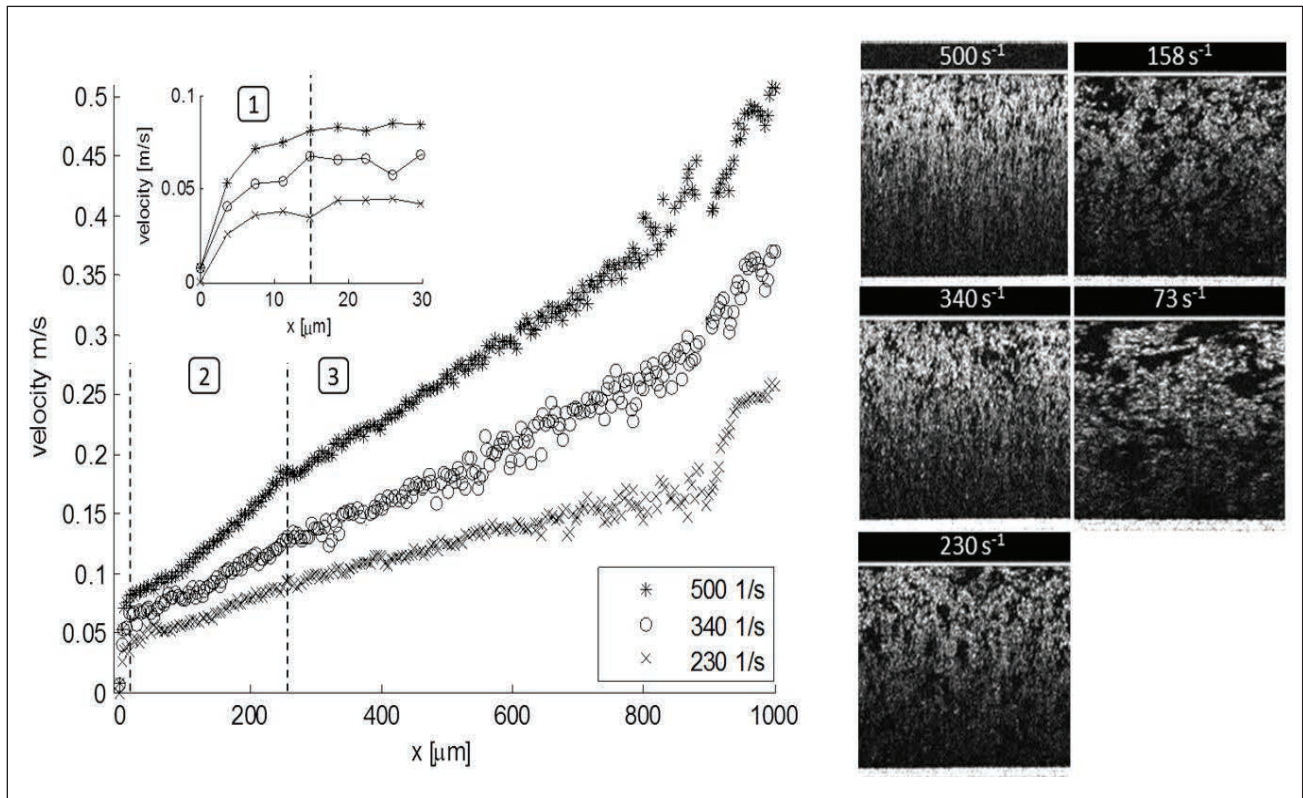
16. Velocity profiles and structure images in the high shear rate region. The profiles have three regions: (1) the wall slip layer, which is about 15 μm thick; (2) the wall boundary layer, which is about 250 μm thick, where the slope of the velocity profile is higher than in the middle of the gap; and (3) the middle area, where the shear rates are 55%-70% smaller than the apparent shear rate. (Note that the optical coherence tomography profiles close to the moving boundary are distorted and thus untrustworthy, probably because the intensity of the scattering signal becomes too small.)

herent, cylindrical, and rotating floc structures (rollers) emerge between the fiber network and the rotating cylinder. OCT results show the same rollers (Fig. 14).

High shear rate region

We see from Fig. 15a that the suspension is rather homogeneous when the shear rate is higher than 100 s^{-1}. **Figure 16** shows OCT velocity profiles and structure images with shear rates greater than 70 s^{-1}. The profiles have three regions:

1) The wall slip layer, which is about 15 μm thick. Near the wall, the viscosity of the suspension is close to water.

2) The wall boundary layer, where the slope of the velocity profile is higher than in the middle of the gap. This layer is about 250 μm thick.

3) The middle area, where the shear rates are 55%-70% smaller than the apparent shear rate. The velocity profiles still differ from the ideal, but in this region the bulk of the suspension exhibits true shear flow.

SUMMARY

Cellulose fiber suspensions are a challenge for conventional rheometers because of their small dimensions and often questionable assumptions about the behavior of the fluid in the gap. Both of these are still obligatory for interpreting the mea-

surements. One can instead use a pipe rheometer in combination with the UVP-PD concept, where the real flow behavior is used for the rheological analysis of the bulk properties of the suspension. However, the resolution of UVP is too low for studying near-wall phenomena, such as the lubrication layer, that are often very important for understanding real-life flows. To address this problem, we augmented the UVP-PD concept with OCT measurements. This enables us to measure bulk and the wall-layer behavior simultaneously.

After verifying the accuracy of the OCT measurements with water, we applied OCT for MFC flow in the pipe rheometer and in a traditional rheometer equipped with a cylinder geometry. We showed that in both cases the boundary layer dynamics play a key role. We also noticed that wall slippage could not be eliminated by using rough or grooved surfaces in the rheometer. Therefore, one has to be very careful with the interpretation of data obtained with traditional rheometers.

In this work, we focused on studying mechanically disintegrated MFC grades in relatively low consistencies. However, OCT opens new possibilities for measuring boundary layer properties for other opaque fluids, including different MFC grades, also in higher consistencies. Our results clearly demonstrate the benefits of having direct measurement of the ve-

locity profile inside the rheometer. OCT has the potential for significant breakthroughs in understanding the rheological properties of complex opaque fluids. By using this method, we have already obtained new information about flow instabilities inside a rheometer gap and used this data to interpret rheometer flow curve [27]. We have also been able to perform a thorough study of the behavior and dynamics of the MFC wall layer during its pipe flow [8].

LITERATURE CITED

1. Haavisto, S., Lille, M., Liukkonen, J., et al., "Laboratory-scale pipe rheometry: a study of a microfibrillated cellulose suspension," *PaperCon*, TAPPI PRESS, Atlanta, GA, USA, 2011.

2. Ouriev, B. and Windhab, E.J., *Exp. Fluids* 32(2): 204(2002).

3. Ouriev, B., Windhab, E.J., Braun, P., et al., *Rev. Sci. Instrum.* 75(10): 3164(2004).

4. Dogan, N., McCarthy, M.J., and Powell, R.L., *Meas. Sci. Technol.* 16(8): 1684(2005).

5. Wiklund, J. and Stading, M., *Flow Meas. Instrum.* 19(3-4): 171(2008).

6. Steger, R., "Optisch und Akustische Methoden in Der Rheometrie," Dissertation, Friedrich-Alexander-Universität, Erlangen-Nürnberg, Germany, 1994.

7. Müller, M., Brunn, P.O., and Wunderlich, T., *Appl. Rheol.* 7(5): 204(1997).

8. Salmela, J., Haavisto, S., Koponen, A., et al., *Fundam. Res. Symp.*, *15th*, The Pulp and Paper Fundamental Research Society, Bury, Lancashire, UK, 2013, p. 405.

9. Jäsberg, A., "Flow behavior of fiber suspensions in straight pipes: new experimental techniques and multiphase modelling", Ph.D. thesis, University of Jyväskylä, Jyväskylä, Finland, 2007.

ABOUT THE AUTHORS

Cellulose fiber suspensions are a challenge for conventional rheometers due to their small dimensions and due to often-questionable assumptions of the behavior of the fluid in the rheometer gap. Due to recent research activity with microfibrillated (MFC) and nanofibrillated (NFC) celluloses, these difficulties have been addressed repeatedly, resulting in indirect evidence of intricate flow phenomena, such as instability, flocculation, and wall slip inside a rotational rheometer.

The restrictions imposed by the measurement system size can be avoided by using pipe rheometers based on, e.g., the ultrasound velocity profiling -pressure difference (UVP-PD) concept. However, these methods most likely provide only the bulk behavior of the fluid because the velocity measurement resolution is too limited to detect near-wall phenomena. With our extensive background in rheology, as well as our knowledge in fiber suspension flows, we explored the flow phenomena of MFC suspensions both inside a rheometer and in a pipe rheometer.

The most challenging aspects of this work were to achieve correct measurement setup and conditions to enable accurate measurements that enable the simultaneous interpretation of both the bulk and the wall-layer behavior. In earlier studies, optical coherence tomography (OCT) has mainly been applied in biomedical flows where the channel dimensions have been very small. As a result of this work, we discovered that boundary layer dynamics play a key role both in the pipe flow and in the traditional rheometer. The measurements can be continued further to get information on the complex processes taking place in the wall layer. This information would be invaluable in flow control and numerical simulations of (MFC) fiber suspension flows.

Haavisto is R&D engineer and Salmela is CTO, Spinnova Ltd., Jyväskylä, Finland. Jäsberg is senior scientist and Koponen is principal investigator, VTT, Technical Research Centre of Finland, Jyväskylä, Finland. Saarinen is product manager, Betulium Ltd., Espoo, Finland. Karppinen is researcher at Borregaard, Sarpsborg, Norway. Email Koponen at antti.koponen@vtt.fi.

Haavisto *Salmela* *Jäsberg* *Saarinen* *Karppinen* *Koponen*
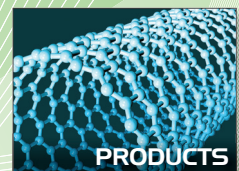
MICROFIBRILLATED CELLULOSE

10. Chow, A., Sinton, S., and Iwamiya, J., *Phys. Fluids* 6(8): 2561(1994).

11. Takeda, Y., *Exp. Therm. Fluid Sci.* 10(4): 444(1995).

12. Harvey, M. and Waigh, T.A., *Phys. Rev. E: Stat., Nonlinear, Soft Matter Phys.* 83(3 Pt 1): 031502(2011).

13. Haavisto, S., Koponen, A., Salmela, *J., Front. Chem.* 2: 27(2014).

14. Haavisto, S., Salmela, J., Koponen, A., *Exp. Fluids* 56(5): 1(2015).

15. Haavisto, S., Salmela, J., Jäsberg, A., et al., *PaperCon*, TAPPI PRESS, Atlanta, GA, USA, 2013, p. 1119.

16. Lavoine, N., Desloges, I., Dufresne, A., et al., *Carbohydr. Polym.* 90(2): 735(2012).

17. Lowys, M., Desbrières, J., and Rinaudo, M., *Food Hydrocolloids* 15(1): 25(2001).

18. Pääkkö, M., Ankerfors, M., Kosonen, H., et al., *Biomacromolecules* 8(6): 1934(2007).

19. Agoda-Tandjawa, G., Durand, S., Berot, S., et al., *Carbohydr. Polym.* 80(3): 677(2010).

20. Iotti, M., Gregersen, O.W., Moe, S., et al., *J. Polym. Environ.* 19(1): 137(2011).

21. Saarikoski, E., Saarinen, T., Salmela, J., et al., *Cellulose* 19(3): 647(2012).

22. Karppinen, A., Saarinen, T., Salmela, J., et al., *Cellulose* 19(6): 1807(2012).

23. Kasai, C., Namekawa, K., Koyano, A., et al., *IEEE Trans. Sonics Ultrason.* 32(3): 458(1985).

24. Tatsumi, D., Ishioka, S., and Matsumoto, T., *J. Soc. Rheol., Jpn.* 32(1): 27(2002).

25. White, F.M., *Fluid Mechanics*, 3rd edn., McGraw-Hill Education, New York, 1994, pp. 310-315.

26. Spalding, D.B., *J. Appl. Mech.*, 28(3): 455(1961).

27. Saarinen, T., Haavisto, S., Sorvari, A., et al., *Cellulose* 21(3): 1261(2014).

III

THE EFFECT OF WALL DEPLETION ON THE RHEOLOGY OF MICROFIBRILLATED CELLULOSE WATER SUSPENSIONS BY OPTICAL COHERENCE TOMOGRAPHY

by

Tapio Saarinen, Sanna Haavisto, Anni Sorvari, Juha Salmela &
Jukka Seppälä, 2014

Cellulose vol 21, 1261–1275

Request publication from the author

IV

THE CHARACTERIZATION OF MICRO-FIBRILLATED CELLULOSE FIBER SUSPENSION FLOW USING MULTI SCALE VELOCITY PROFILE MEASUREMENTS

by

Markku Kataja, Sanna Haavisto, Juha Salmela, Roope Lehto &
Antti Koponen, 2017

Nordic Pulp and Paper Research Journal vol 32, 473–482

Characterization of micro-fibrillated cellulose fiber suspension flow using multi scale velocity profile measurements

Markku Kataja, Sanna Haavisto, Juha Salmela, Roope Lehto and Antti Koponen

ABSTRACT: Rheological properties and boundary layer flow behavior of Micro Fibrillated Cellulose (MFC) suspended in water was studied using a novel velocity profiling rheometric technique. The method is based on measuring stationary velocity profiles of fluid flow in a straight tube simultaneously by Doppler Optical Coherence Tomography (DOCT) and by Ultrasound Velocity Profiling (UVP). The high resolution DOCT provides velocity profiles near the transparent tube wall, while UVP yields corresponding information in the interior parts of the flow. The data from the two instruments is combined into a comprehensive velocity profile including both the thin boundary layer near the wall and the interior parts of the flow. Within the boundary layer, concentration and thereby the viscosity of MFC is found to decrease towards the wall. At high flow rate, sublayer of virtually pure water is observed next to the wall, giving rise to apparent wall slip. The results from interior part of the flow show shear thinning behavior in qualitative agreement with results from conventional rheological methods. The results indicate that the new method can provide detailed experimental information on the rheology of MFC suspensions and their intricate boundary layer flow behavior, avoiding uncertainties inherent in many conventional rheological techniques.

ADDRESSES OF THE AUTHORS: Markku Kataja (markku.kataja@jyu.fi) **Roope Lehto** (roope.lehto@ jyu.fi), University of Jyväskylä, P.O. Box 35, FI-40014 Jyväskylä, Finland, **Sanna Haavisto** (sanna.haavisto@ spinnova.fi) **Juha Salmela** (juha.salmela@spinnova.fi), Spinnova Ltd. Asematie 11, 40800 Vaajakoski, Finland, **Antti Koponen** (antti.koponen@vtt.fi), VTT Technical Research Centre of Finland, P.O. Box 1603, 40101 Jyväskylä, Finland
Corresponding author: Markku Kataja

Introduction

As potential ingredients for novel bio-based materials and high-end products, Microfibrillated Cellulose (MFC) materials are subject of active research and of commercial interest within forest industry. Often, production and processing of MFC involves the fibrous MFC material suspended in a carrier fluid, typically water. Similar to many other natural and synthetic fiber suspensions, the rheological and flow properties of aqueous MFC suspensions are diverse, and depend strongly on the fiber properties and fiber mass concentration (Klemm et al 2011). Already at a very low concentration, aqueous MFC suspensions can show intricate rheological properties such as gel formation, yield stress, shear thinning, hysteresis, and thixotropy (Iotti et al 2011; Karppinen et al 2012; Martoïa et al 2015; Shafiei-Sabet et al 2016; Mohtaschemi et al 2014). These properties derive primarily from the inherent entangled heterogeneous network of fibrils and partially disintegrated fibers having high specific surface area, aspect ratio, strength and flexibility (Lavoine et al 2012).

Conventional experimental techniques for measuring rheological properties of fluids are typically based on simple and well-defined flow geometries where the flow condition is assumed known (Morrison 2001). Analysis of data from such experiments is thus based on certain conjectures concerning the flow velocity profile and boundary conditions that are assumed to prevail in the flow. While appropriate for many homogeneous non-Newtonian fluids, such presumptions are questionable in the case of complex heterogeneous fluids (Mewis, Moldenaers 1999). The rheological parameters thereby obtained may not reflect properties of the fluid alone, but also of the particular flow used in the measurement. Consequently, the parameters may lack generality and lead to erroneous results if applied in flow in conditions not similar to that used in the rheological experiment (Nechyporchuk et al 2014; Saarinen et al 2014; Naderi. Lindström 2016).

The crux of velocity profiling rheometry is to combine conventional rheological techniques and simultaneous measurement of flow velocity profile (Powell et al 1994; Hanlon et al 1998; Raynaud et al 2002; Dogan et. al. 2002; Ouriev, Windhab 2002). The data analysis can then be based on a measured instead of assumed velocity profile. Velocity profiling techniques applicable for turbid fluids are e.g. Nuclear Magnetic Resonance Imaging (NMRI) or Ultrasound Velocity profiling (UVP) (Powell 2008). Both UVP and NMRI have been tested for several rheologically complex fluids and multiphase systems of practical interest e.g. in food, paper and chemical industries (Britton, Callaghan 1997; Dogan et al 2005; Wassell et al 2010; Derakhshandeh et al 2010; Haavisto et al 2011). The concept is well established and has been implemented as in-line rheometers in industrial processes providing means for process monitoring and quality control (Wunderlich, Brunn 1999; Ricci et al 2012; Arola et al 1997; Kotzé et al 2012).

Techniques such as UVP and NMRI allow measuring flow velocity of also turbid fluids well inside the flow. Due to their limited spatial resolution (Manneville 2008; Fock et. al. 2011) and, especially for UVP, disturbance caused by solid-fluid interfaces (Wunderlich and Brunn 2000), these methods are hardly accurate enough to resolve the flow profile in the immediate vicinity of a

bounding surface. This is unfortunate as the boundary layer behavior of heterogeneous fluids can be quite intricate and can dominate the overall observed flow behavior. A common example of such a case is stationary plug flow of pulp in a straight pipe where the observed velocity is nearly constant in the pipe cross-section and apparent slip occurs at the wall (Pettersson et al 2006; Soszynski 1991; Duffy 2006). Obviously, the complex flow dynamics, reflected e.g. by the measured friction loss behavior of such flow, is dominated by a very thin layer at the tube wall. Obtaining direct experimental data on such a thin layer is not, in general, straightforward for complex flows involving e.g. opaque fluids, and the related flow phenomena remain poorly understood (Fock et al 2011).

Optical Coherence Tomography (OCT) is a non-invasive technique capable of fast real-time high-resolution imaging of the internal structure of an opaque scattering medium in the vicinity of its surface (Fercher et al 2003; Schmitt 1999). The imaging depth of OCT is limited by the used optics and by attenuation of light in the material. In addition to giving access to structural data, the method can be extended to provide velocity information through Doppler Optical Coherence Tomographic (DOCT) technique (Wang et al 1997; Chen, Zhang 2015). Furthermore, the DOCT method appears capable of accurate high-resolution measurement of velocity profile very close to a channel wall, and is thus well suited in detailed study of the boundary layer flow behavior of complex fluids with suitable optical properties (Haavisto et al 2014; Wang 2004; Malm et al 2015).

In this work we report results on rheological and boundary layer flow properties of a MFC suspension, obtained by a novel in-line rheological method (Salmela et al 2013) utilizing velocity profiling. The velocity profile is measured by combining data from simultaneous measurements by DOCT and UVP. Here, DOCT is used to measure the velocity profile in the immediate vicinity of a transparent tube wall, typically closer than 1 mm, while UVP provides the same information in the interior parts of the tube. The combination of data from these instruments provides a comprehensive velocity profile including both the boundary layer and bulk regions of the MFC suspension.

Materials and Methods

Materials

The microfibrillated cellulose used in this work was obtained from Daicel Chemical Industries, Japan. The product type was Celish KY-100G, which is manufactured from purified wood pulp. The basic properties of this commercial MFC have been reported in literature. The average length and diameter of the fibers are 350 μm and 15 μm, respectively (Tatsumi et al 2002). The final MFC suspensions used in the flow experiments were obtained by diluting the original MFC by deionized water to mass concentrations of 0.4%, 1.0% and 1.6% using high intensity mixing by an overhead stirrer (Glas-Col).

Experimental Setup

The measurement unit consisted of a 2.5 m long optical grade glass tube with an inner diameter of 19 mm. The flow in the tube was driven by a low-pulsation progressive cavity pump (Seepex MD series). Total volume of the sample in the flow loop and in the tank was 13.5 liters. The fluid temperature in the loop was set to 21°C with a digital temperature control unit (PolyScience, model 9610). The volumetric flow rate in the loop was adjusted manually using the pump control voltage, and measured using a magnetic flow rate sensor (Siemens, Sitrans F M MAGFLO).

The measurements were carried out at stationary flow conditions at several values of total flow rate in the range $8 - 160$ ml/s (see *Fig 3* and *4*). The fluid temperature during each trial point was measured with a thermocouple (Fluke multimeter). The wall shear stress at each flow rate was found based on pressure difference measurement between two 1.5 mm diameter taps drilled through the tube wall located at 74 and 126 diameters downstream from the tube inlet. The pressure difference measurement was done using calibrated sensors (Rosemount, sensor types 3051 and 2051). A schematic of the tube flow system is shown in *Fig 1*.
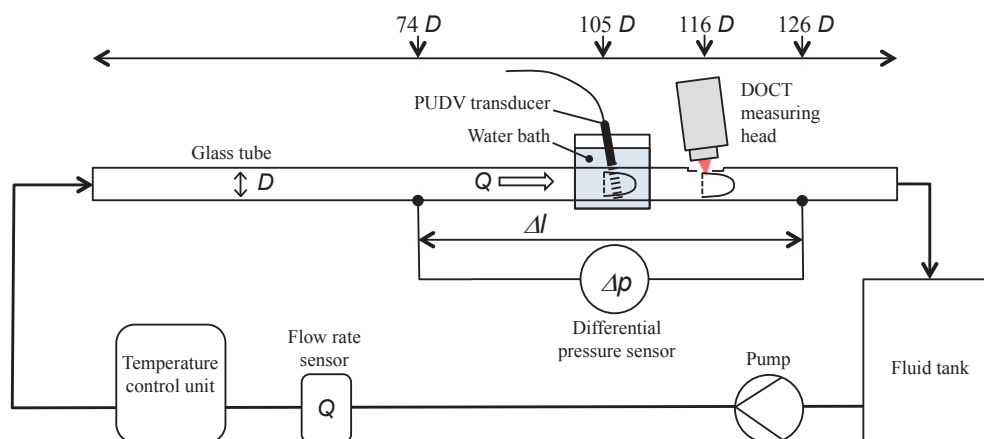

Fig 1- Schematic illustration of the experimental set-up with simultaneous UVP and DOCT measurement of fully developed velocity profile of MFC suspension in a straight glass tube of diameter D=19 mm and length 2.5 m.

Optical Coherence Tomography

In the spectral domain OCT used in this work, a low coherence light beam is emitted from a super luminescent led light source and split into the sample arm and the reference arm of a Michelson interferometer (Schmitt 1999). The backscattered interference pattern, called A-scan, is Fourier-transformed to give information about the sample scattering index from different depths inside the sample. Cross-sectional images of the sample can be constructed from a series of A-scans by recording depth profiles from different lateral locations of the sample. Such a collection of A-scans is called a B-scan. The resolution of an OCT system in the direction parallel to the light beam is determined by the central wavelength and bandwidth of the light source, while the lateral (cross beam) resolution is determined by the diffraction limited spot size of the focused optical beam. Contrary to standard microscopy, OCT can thereby achieve good parallel resolution independent of the beam focusing and spot size. The OCT device used in this study was Telesto Spectral Domain OCT (Thorlabs, Inc.) with a central wavelength of 1325 nm and bandwidth in excess of 150 nm. The resolutions in the parallel and lateral directions are approximately 3.7 µm (in water) and 15 µm, respectively. The Doppler Optical Coherence Tomography (DOCT) is a modality of OCT that can be used to obtain velocity information. In a DOCT mode, the Doppler frequency generated by a moving object is detected from the phase difference between two or more adjacent A-scans, thus yielding the velocity component in the direction of the light beam (Haavisto et al 2015b).

In this work OCT was used both in imaging the MFC suspension microstructure and for measuring the velocity profile near the tube wall. The OCT measuring head was located 116 tube diameters downstream from the tube inlet. A region of flat surface was ground on the glass tube outer surface in order to minimize thickness of the tube wall and to prevent unwanted refraction of light at the measuring point. In the imaging mode B-scans across a physical width of 5 mm in the tube axial direction were acquired (see *Fig 9*). For flow velocity measurements, small amount of coffee creamer was added as light scattering tracer in the suspension to ensure appropriate level of signal also from the regions of fluid between MFC aggregates. Stationary state velocity profiles at each constant value of flow rate were obtained based on scattering data from a sequence of about 60 000 A-scans at a single position. The data acquisition frequency was 5.5, 28 or 91 kHz, depending on flow rate. Assuming fully developed flow in the tube, the axial velocity profile is given by

$$u(y) = \frac{u_b(y)}{\cos\theta_D}, \qquad [1]$$

where y is the distance from the tube wall, $u_b(y)$ is the measured velocity component in the beam direction and θ_D is the Doppler angle (angle of the incident light beam and tube axis). The value of the Doppler angle was conveniently obtained by utilizing the imaging modality of OCT at the same setting of the measuring probe, and evaluating the inclination of the tube inner wall visible in the images (see *Fig. 9*). A typical value of θ_D used here was $86° - 87°$.

Ultrasound Velocity Profiling

Ultrasound velocity profiling technique is based on using an emitter/receiver to send a series of short ultrasound bursts into the flow, and detecting the sound reflected from the target particles moving along with the flow. The location of the particles is acquired with the time-of-flight method using the known velocity of sound. The velocity of the moving particles is calculated from cross-correlation between the echoes from consecutive pulses. In the present study, a DOP2000 (Signal-Processing S.A., Switzerland) device equipped with an 8 MHz ultrasound probe was used. The probe was installed in a water bath surrounding the tube 105 diameters downstream from the tube inlet, and at angle of 78.5° relative to tube axis. The pulse repetition frequency was varied between 500 and 2000 Hz in order to exploit full velocity resolution range. The pulse length was ~0.38 mm in water (2 wavelengths), which also gives the spatial resolution. In all measurements, 32 consecutive pulse emissions were used to calculate a single velocity value in each sampled depth locations. The mean velocity profile for a given flow rate was calculated as the average of the results from 500 individual velocity profiles measurements.

In analogy to DOCT, the present UVP device measures a single velocity component in the direction of the ultrasound beam. The flow velocity u is again given by *Eq 1*, and is thus susceptible to systematic error related to uncertainty in the value of θ_D ($\lesssim 90°$). The Doppler angle for the UVP measurement was determined manually by measuring the setting angle between the tube upper surface and the body of the ultrasound transducer. Here, error may occur as the actual Doppler angle, i.e. the angle of incident of the ultrasound beam that enters the flow, may deviate from the measured probe setting value due to e.g. mechanical manufacturing tolerances of the probe, angle measurement error and refraction of sound at tube wall surfaces. Similar uncertainty applies also to DOCT although in that case, the Doppler angle can be found more directly using the imaging mode of OCT, as discussed above. More detailed discussion on the effects of various uncertainties related to the two methods can be found in reference (Szkulmowska et al 2008; Messer, Aidun 2009).

Results and Discussion

In *Fig 2 (a)* shown is the measured pressure loss as a function of flow rate measured in a straight tube of diameter $D=19$ mm at various values of concentration of MFC suspension. The pressure loss behavior is found to be qualitatively similar to that of pseudoplastic fluids. At the lowest concentration of 0.4%, the non-linear behavior is quite weak, however. At the highest concentration of 1.6% instead, the pressure loss shows a distinct plateau, similar to what is often found for e.g. pulp suspensions (Jäsberg 2007; Sumida 2013; Duffy 2006). The detailed reason for such behavior is discussed below.
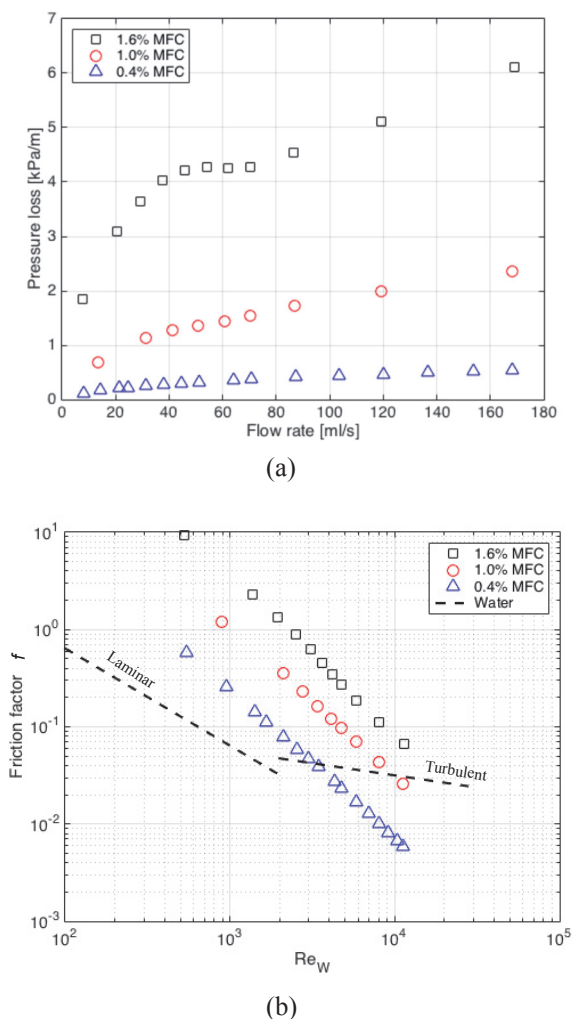
(a)

(b)

Fig 2 - (a) Measured pressure loss vs. flow rate for MFC suspension at various concentrations. (b) Friction factor vs. Reynolds number calculated using viscosity of water. Also shown are the standard correlations for water in laminar flow (f = 64/Re) and in turbulent flow for smooth pipes according to Blasius' correlation (f = 0.316/Re$^{0.25}$).

Fig 2(b) shows the loss behavior in terms of Darcy friction factor as a function of Reynolds number Re$_w$ calculated using viscosity of water. The data does not show evidence on transition to turbulent flow in the used range of flow rate. Especially in the case of 0.4% consistency the delayed transition to turbulence leads to distinct drag reduction typical to many polymer solutions and fiber suspensions (Escudier et al 1999; Lee, Duffy 1976).

Velocity Profiles

In most cases studied in this work, the velocity profiles measured by DOCT in the near wall region and by UVP in the interior parts of the tube show overlapping region of mutually consistent results. Typically, such overlap region is found within distance 0.5 – 1.0 mm from the tube wall, see *Fig 3 (a)* and *(b)*. Slight systematic deviation may occur e.g. due to the uncertainty of the used values of Doppler angle. In practice, appropriate match in the overlap region was thus achieved by fine-tuning the Doppler angle used in *Eq 1* for the UVP

measurement. The combined velocity profile was then normalized such that the integrated total flow rate coincides with the flow rate measured independently by the magnetic flow rate sensor. This procedure of matching and normalization of the velocity profiles helps eliminating the systematic uncertainties related to absolute velocity values inherent in both methods while retaining the information related to the shape of the profiles. In the case of MFC at concentration 1.6%, the penetration depth of the DOCT light signal was reduced and the regions of accurate measurement of the two techniques do not show distinct overlap (see *Fig 3 (c)*). In this case reasonably accurate patching of the profiles was nevertheless obtained by using DOCT results extrapolated into the UVP measurement region by means of a suitable fitting function (see *Eq 3* below). In all measured cases, the corrections to the measured UVP Doppler angle required for profile matching and to the overall flow rate normalization, were below 0.3° and 10%, respectively.

Fig 3 shows the combined stationary velocity profiles at various total flow rates, as measured with DOCT and UVP techniques. (The bulge present in the velocity profile for the highest flow rate in *Fig 3(a)* is most likely a measurement error. Such artifacts are typically created by spurious reflections of the ultrasound pulses from tube walls, air bubbles etc.) The overall velocity profile appears to include two dynamically different parts. In the interior part of the tube, at the distance range of 200 μm $\lesssim y \leq D/2$, the profile is relatively shallow and qualitatively resembles that of a pseudoplastic fluid. In macroscopic scales the flow behavior of MFC appears as that of a shear thinning fluid with wall slip. The high-resolution DOCT data shown in more detail in *Fig 4* reveals, however, that in a thin near-wall region, the velocity profile is very steep and approaches rapidly zero towards the wall. No actual wall slip is thus observed.

Viscosity Characteristics

Given the combined velocity profile $u(y)$ it is straightforward to numerically estimate the value of local shear rate $\dot{\gamma} = du(y)/dy$ at distance y from the wall. For a stationary axial flow, the shear stress at position y is given by $\tau(y) = \tau_w(1 - y/R)$, R is tube radius and $\tau_w = R\Delta p/2L$ is the wall shear stress obtained from pressure loss Δp measured over a tube segment of length L (here 54 pipe diameters). The local value of viscosity at position y is thus given by

$$\mu(y) = \frac{\tau(y)}{\dot{\gamma}(y)}. \qquad [2]$$

Utilizing the measured velocity profile we thus obtain the viscosity profile within the entire range of shear rate values present in the flow at each constant total flow rate. Notice however, that for MFC materials studied here, the total shear stress $\tau(y)$ may include elastic contribution. The viscosity formally defined by *Eq 2* may thus not be purely of frictional origin, and may depend on elastic strain in addition to strain rate.
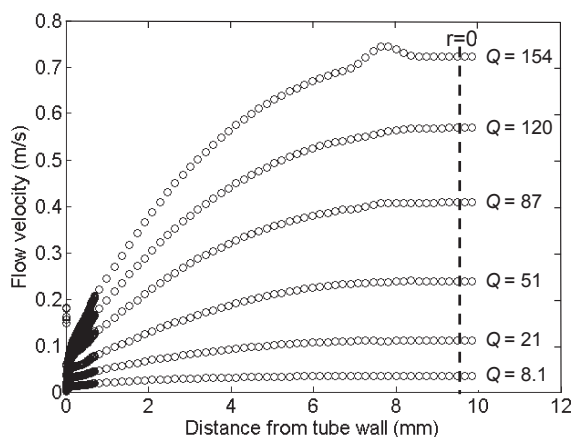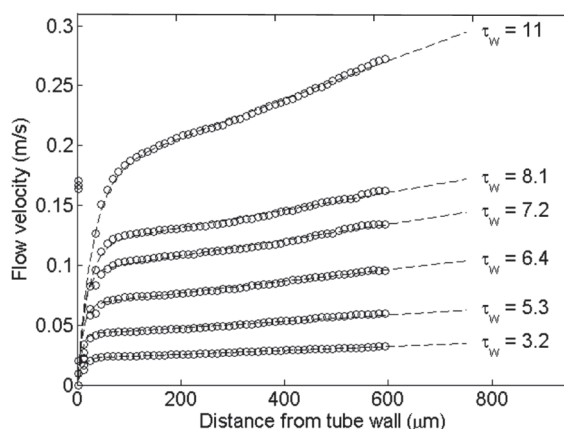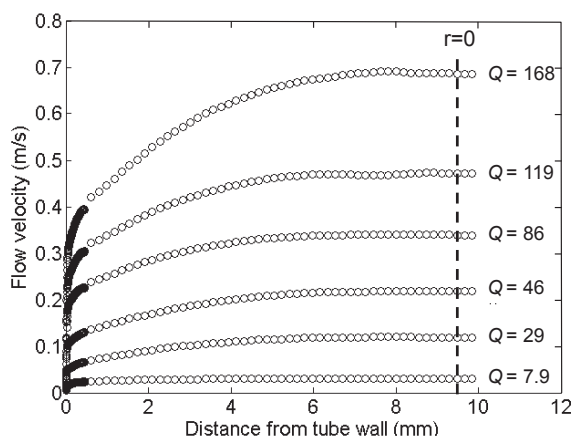
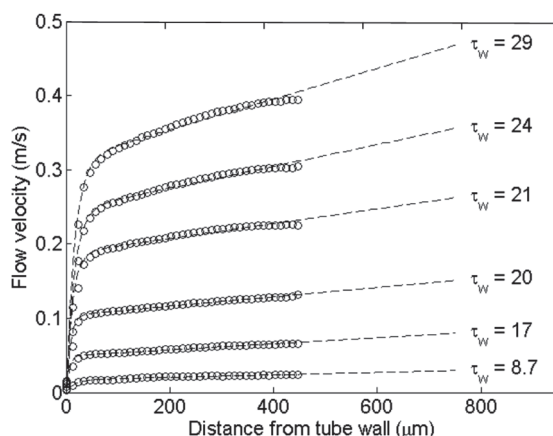(a) MFC 0.4%
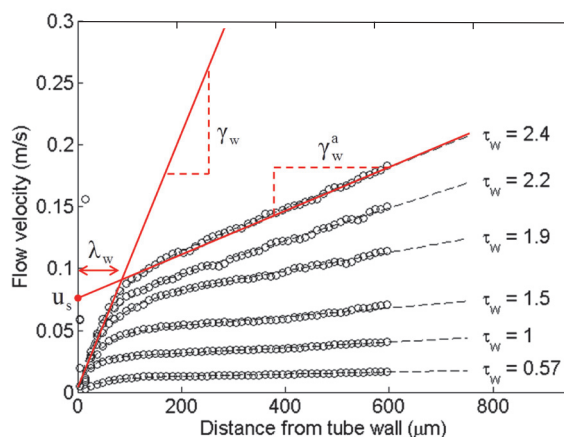
(a) MFC 0.4%
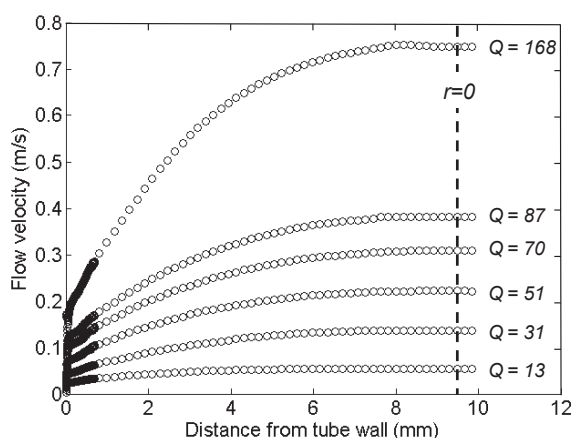
(b) MFC 1.0%

(b) MFC 1.0%

(c) MFC 1.6%

(c) MFC 1.6%

Fig 3 - Velocity profiles of three different MFC suspensions combined from DOCT and UVP measurements. The velocity values from DOCT, appearing as dark symbols near the wall, are shown in more detail in *Fig 4*. The labels to different profiles give the total low rate [ml/s]. The vertical dashed line indicates centerline of the tube.

Fig - 4. Near-wall velocity profiles measured by DOCT. The labels to different profiles give the wall stress [Pa] (the corresponding flow rates can be found in *Fig 3*). Graphs of *Eq 3* fitted to DOCT data are shown as dashed lines. The geometric interpretation of the fitting parameters is given in subfigure (a)
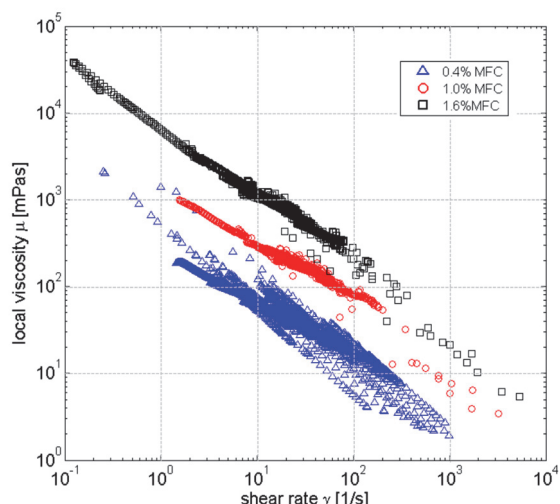
Fig 5 - Viscosity of MFC suspensions at various concentrations as a function of shear rate, calculated locally from the measured velocity profiles.

Fig 5 summarizes the values of viscosity vs. shear rate, obtained from *Eq 2*, for all values of flow rate measured and for the three values of consistency. The viscosity behavior of MFC suspension shows overall shear-thinning characteristics, in qualitative accordance with results obtained with conventional rheometric techniques (Haavisto et. al. 2015a; Kumar et. al. 2016; Agoda-Tandjawa et. al. 2010; Saarinen et. al. 2014).

At low values of shear rate ($\dot{\gamma} \lesssim 10$ s^{-1}), originating from inner parts of the tube, the measured values of viscosity show power-law type of correlation with shear rate. At higher values of shear rate, related to the near-wall boundary layer, the behavior is qualitatively different, as viscosity does not show clear correlation with shear rate alone. Indeed, closer examination of the boundary layer, discussed in more detail in the next section, indicates that concentration of MFC decreases towards the wall in that thin layer. Within the boundary layer viscosity thus depends on both the local shear rate and the local concentration, and can have values significantly lower than in the interior parts of the tube.

Boundary Layer Behavior
We now study the boundary layer behavior and the rheological properties of MFC suspension near the tube wall using the DOCT data shown in *Fig 4*. Within the region $y \lesssim 500$ µm, the measured velocity profiles can be closely approximated by the formula

$$u(y) = \dot{\gamma}_w^a y + u_s^a \left(1 - e^{-y/\lambda_w}\right), \qquad [3]$$

where λ_w, u_s^a, and γ_w^a are free parameters found by fitting to the velocity profile data. The parameter λ_w characterizes the thickness of the wall boundary layer underlying the apparent wall slip. The parameters u_s^a and γ_w^a can be interpreted as the apparent slip velocity and the apparent wall shear rate, respectively (see *Fig 4 (a)*). Using these parameters, we can also define the apparent value of viscosity at wall as $\mu_w^a = \tau_w/\dot{\gamma}_w^a$. As obvious from these definitions the term 'apparent' is used here to refer to wall quantities observable in the macroscopic scales and related to the velocity profile shape just

outside the boundary layer ($y \gtrsim \lambda_w$). In principle, the apparent parameters could be measured using UVP or similar low-resolution technique alone. Instead, measuring the boundary layer thickness and the velocity profile within the thin boundary layer require high-resolution method such as DOCT.

The shear rate at the wall ($y = 0$) is given in terms of the three fitting parameters described above as

$$\dot{\gamma}_w \equiv \left(\frac{du}{dy}\right)_{y=0} = \dot{\gamma}_w^a + \frac{u_s^a}{\lambda_w} \quad . \qquad [4]$$

The value of viscosity at wall is then given by $\mu_w = \tau_w/\dot{\gamma}_w$. As evident from the shape of the velocity profiles shown in *Fig 4*, we typically have that $\dot{\gamma}_w \gg \dot{\gamma}_w^a$, and thus that $\mu_w \ll \mu_w^a$ and $\dot{\gamma}_w \approx u_s^a/\lambda_w$.

Fig 6 shows the measured wall shear stress and the apparent viscosity at wall as functions of apparent wall shear rate for the MFC suspensions at various concentrations. Again, we notice that the overall behavior of the suspension is shear thinning and, especially at the lower values of consistency, is qualitatively close to that of a power law fluid for which $\tau \propto \dot{\gamma}^{\frac{1}{2}} \left(\mu \propto \dot{\gamma}^{-\frac{1}{2}}\right)$.
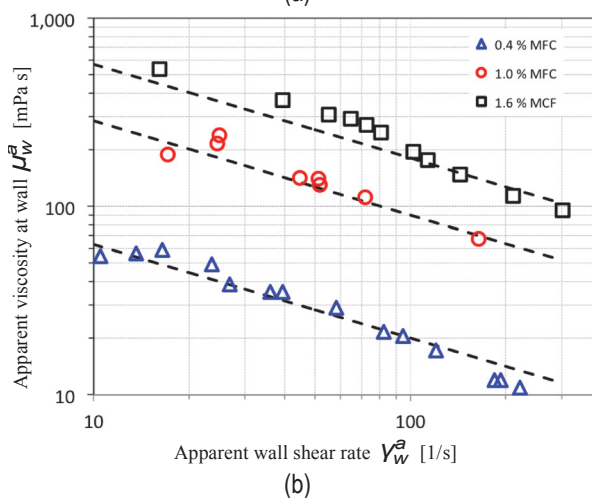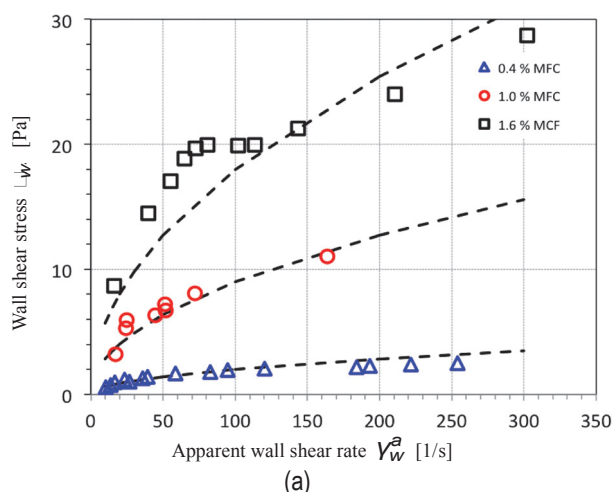

(a)

(b)

Fig 6 - Wall shear stress (a) and apparent viscosity (b) at wall as functions of apparent shear rate at wall for MFC suspension at various values of consistency. The dashed lines representing power law behavior $\tau \propto \dot{\gamma}^{\frac{1}{2}}$ are shown for reference.

The plateau visible in the shear stress behavior of especially 1.6% MFC (see also *Fig 2(a)*) is most likely related to existence of concentration gradient and, at higher values of flow rate, even of a thin particle depletion layer near the wall. The well-known explanation for such phenomenon is given by the combined effect of steric hindrance and repulsive hydrodynamic interaction between the tube wall and suspended particles (Barnes 1995; Medhi et al 2011; Leighton, Acrivos 1987; Jäsberg et al. 2000). This interpretation is supported by *Fig 7 (a)* and *(b)* showing the measured dependence of viscosity at wall and of apparent slip velocity on wall shear stress, respectively. At low values of wall shear stress (and of flow rate), viscosity at wall decreases and slip velocity increases with wall shear stress. In the case of 1.6% MFC a distinct transition at $\tau_w \approx 20$ Pa is found. Around that point, apparent slip velocity increases rapidly while viscosity at wall becomes constant with the value near that of water ($\mu_w \sim 1$ mPa·s). A plausible interpretation of this result is that at low flow rate, the particulate phase is in contact with tube wall, and contributes to total friction. The repulsive hydrodynamic force between the tube wall and the particles increases with flow rate leading to gradual decrease of elastic normal force and of direct friction between particles and the wall.
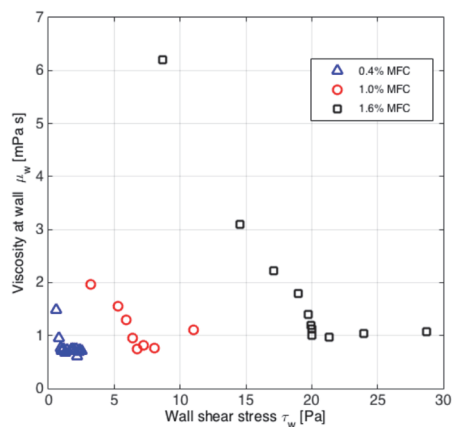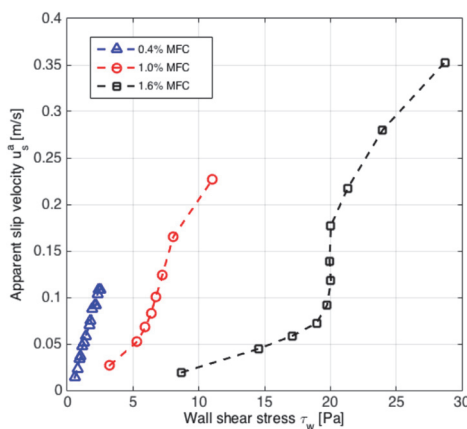
In the transition point, repulsive interaction overcomes the elastic stress in the MFC material and a narrow layer of virtually pure water is formed near the wall. Such an effect characterizes also flows of *e.g.* pulp suspensions (Derakhshandeh et al 2011). In the case of 1.0% MFC similar but somewhat less abrupt transition occurs at $\tau \approx$ 7 Pa. At the lowest consistency of 0.4%, the transition seems to occur already at very low flow rate, being barely visible in the viscosity behavior shown in *Fig 7 (a)*. The increase of the transition point and the more distinct characteristics of the transition are qualitatively explained by the increase of elastic stiffness of the fibrous network with consistency of the MFC material.

The existence of the low viscosity layer is visible also in *Fig 8* showing the local values of viscosity for consistency 1.0% as a function of distance from the wall, for several values of total flow rate. The local values of viscosity are obtained from *Eq 2* and *3* using the measured values of wall shear stress τ_μ and parameters λ_w, u_s^a, and γ_w^a fitted to DOCT velocity profiles shown in *Fig 4(b)*. Outside of the boundary layer viscosity decreases with flow rate (and with local shear rate). Towards the wall, the value of viscosity decreases and approaches that of water irrespective of the flow rate, and thus, of the wall shear rate. Direct qualitative evidence on correlation between viscosity behavior and concentration gradient near the wall is obtained by utilizing the imaging modality of OCT. *Fig 9* shows examples of still images of the structure of MFC suspension flow near the tube wall together with long time averaged images. The OCT images are constructed as the spatial distribution of back-scattering index of light. The scattering index, in turn, correlates with the concentration of suspended particles that contribute to scattering. The light shades of grey near the tube wall thus indicate lower concentration as compared to inner parts of the tube. The concentration boundary layer is barely visible in the case of 1.6% MFC. More detailed study of the correlation between concentration and viscosity will be presented elsewhere.

(a)

(b)

Fig 7 - Viscosity at tube wall $y = 0$ (a) and apparent slip velocity (b) as functions of wall shear stress for MFC suspension at various concentrations.
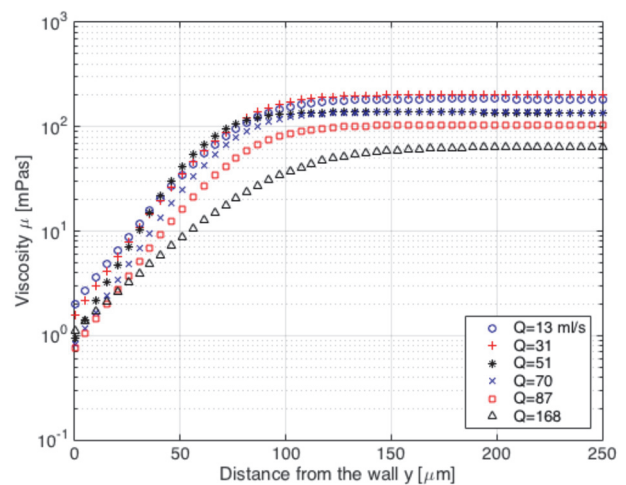

Fig 8 - Viscosity of 1.0% MFC suspension as a function of distance from the wall for several values of total flow rate. The local values of viscosity are calculated based on measured wall shear stress and on velocity profiles fitted to DOCT data.
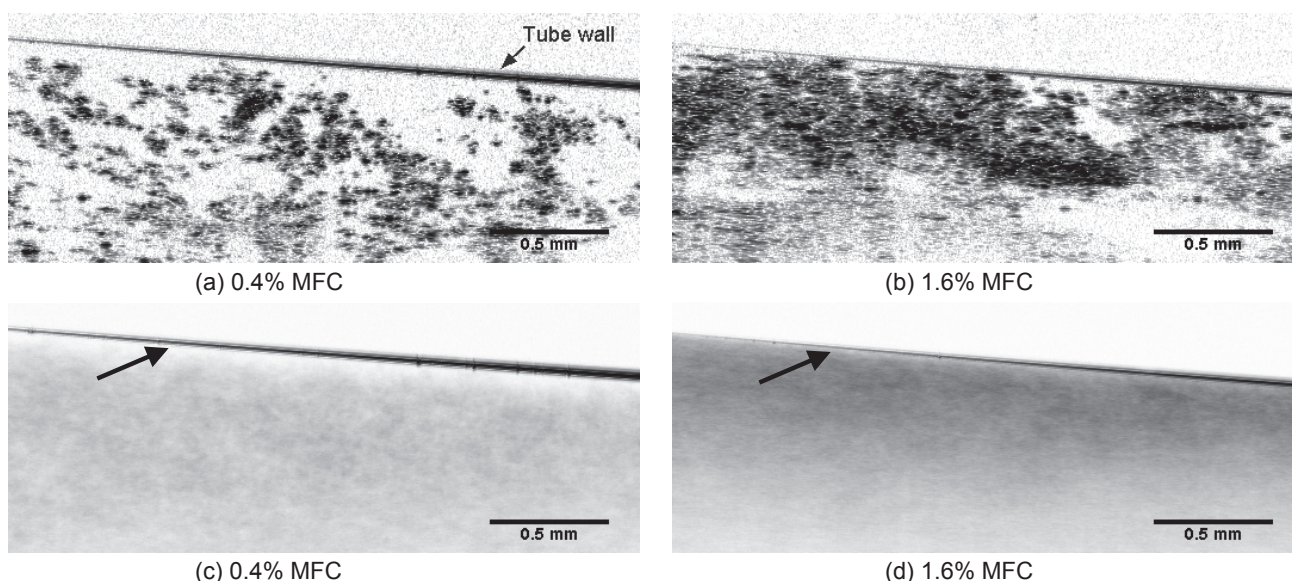
Fig 9 - OCT still images (a-b) and long time average images (c-d) of boundary layer flow of MFC suspension of consistencies 0.4% and 1.6%. The regions covered by MFC and water are shown in the still images as dark and light gray shades, respectively. The time averaged images are obtained as mean of 200 still images taken over a time interval of about 20 s. The boundary layer with concentration decreasing towards the tube wall appears as lighter gray color and is indicated by arrows in subfigures (c) and (d). The apparent inclination of the tube wall in the images is due to setting angle of the DOCT measuring head, as required for axial velocity measurement.

Conclusions

A novel experimental method, based on simultaneous use of Doppler Optical Coherence Tomography (DOCT) and Ultrasound Velocity Profiling (UVP), was used to study the rheological properties and boundary layer behavior of micro-fibrillated cellulose (MFC) suspension flow in a straight tube at consistencies 0.4%, 1.0%, and 1.6% by weight. The two velocity profiling methods are complementary in the sense the DOCT technique is capable of high-resolution measurement of the boundary layer flow very close to the tube wall while the UVP method is useful in measuring the velocity profile in the interior parts of the tube with lower spatial resolution. A comprehensive velocity profile including both the thin boundary layer and the interior parts of the tube can be obtained by combining the velocity profiles from the two methods. Such combination is straightforward at lower values of consistency where the effective measuring ranges of the two methods overlap. At consistency 1.6% the penetration depth of the optical signal of DOCT was reduced such that no distinct overlap was achieved. Even then, adequate patching of the profiles was obtained by slight extrapolation of the measured results.

In the interior parts of the tube where the MFC consistency is constant, in average, the results show typical shear thinning behavior, in qualitative agreement with results obtained by conventional rheometric methods. The near wall behavior shows existence of a boundary layer where the mean concentration decreases towards the wall. Such a concentration gradient is most likely created by combined effect of steric hindrance by the wall and hydrodynamic lift that induces migration of MFC particles away from the wall. The thickness of such boundary layer increases with flow rate and decreases with MFC concentration. The maximum boundary layer thickness observed here was of the order of 200 μm. With increasing flow rate (wall shear stress), the fluid next to the tube wall may become nearly Newtonian with viscosity close to that of water. Such behavior indicates existence of a sublayer depleted of particles in the close vicinity of the wall, and leads to apparent wall slip. The local value of viscosity increases with distance from the wall, along with increasing concentration. The concentration boundary layer can be directly observed by using the imaging modality of optical coherence tomography.

References

Agoda-Tandjawa G., Durand S., Berot S., Blassel C., Gaillard C., Garnier C. and Doublier J.-L. (2010): Rheological characterization of microfibrillated cellulose suspensions after freezing, Carbohydr. Polym. 80(3), 677-686.

Arola D. F., Barrall G. A., Powell R. L., McCarthy M. J. and McCarthy K. L. (1997): Use of nuclear magnetic resonance imaging as a viscometer for process monitoring, Chem. Eng. Sci. 52(13), 2049-2057.

Barnes H. A. (1995): A review of the slip (wall depletion) of polymer solutions, emulsions and particle suspensions in viscometers: its cause, character, and cure, J. Non Newtonian Fluid Mech. 56(3), 221-251.

Britton M. M. and Callaghan P. T. (1997): NMR microscopy and the non linear rheology of food materials, Magn. Reson. Chem. 35(13)

Chen Z and Zhang J (2015):. "Doppler optical coherence tomography,"Optical Coherence Tomography: Technology and Applications, eds. W. Drexler and J. G. Fujimoto Switzerland: Springer, 1289-1320

Derakhshandeh B., Kerekes R., Hatzikiriakos S. and Bennington C. (2011): Rheology of pulp fibre suspensions: A critical review, Chem. Eng. Sci. 66(15), 3460-3470.

Derakhshandeh B., Hatzikiriakos S. G. and Bennington C. P. (2010): Rheology of pulp suspensions using ultrasonic Doppler velocimetry, Rheologica Acta 49(11-12), 1127-1140.

Dogan N., McCarthy M. and Powell R. (2002): In Line Measurement of Rheological Parameters and Modeling of Apparent Wall Slip in Diced Tomato Suspensions Using Ultrasonics, J. Food Sci. 67(6), 2235-2240.

Dogan N., McCarthy M. J. and Powell R. L. (2005): Measurement of polymer melt rheology using ultrasonics-based in-line rheometry, Meas. Sci. Technol. 16(8), 1684-1690.

Duffy G. G. (2006): Measurements, mechanisms and models: Some important insights into the mechanisms of flow of fibre suspensions, Annual Transactions of The Nordic Rheology Society 14, Nordic Rheology Society, ,19-31.

Escudier M., Presti F. and Smith S. (1999): Drag reduction in the turbulent pipe flow of polymers, J. Non Newtonian Fluid Mech. 81(3), 197-213.

Fercher A. F., Drexler W., Hitzenberger C. K. and Lasser T. (2003): Optical coherence tomography - principles and applications, Reports on Progress in Physics 66(2), 239-303.

Fock H., Claesson J., Rasmuson A. and Wikström T. (2011): Near wall effects in the plug flow of pulp suspensions, TCan. J. Chem. Eng. 89(5), 1207-1216.

Haavisto S., Lille M., Liukkonen, J., Jäsberg, A., Koponen A. and Salmela J. (2011): Laboratory-Scale Pipe Rheometry: A Study of a Microfibrillated Cellulose Suspension, Proceedings of Papercon 2011, Northern Kentucky Convention Center, May 1-4, Proceedings of Papercon 2011, ,357-370.

Haavisto S., Salmela J., Jasberg A., Saarinen T., Karppinen A. and Koponen A. (2015a): Rheological characterization of microfibrillated cellulose suspension using Optical Coherence Tomography, Tappi J. 14(5), 291-302.

Haavisto S., Salmela J. and Koponen A. (2015b): Accurate velocity measurements of boundary-layer flows using Doppler optical coherence tomography, Exp. Fluids 56(5), 1-6.

Haavisto S., Koponen A. I. and Salmela J. (2014): New insight into rheology and flow properties of complex fluids with Doppler optical coherence tomography, Front. Chem. 2(27), 1-6.

Hanlon A. D., Gibbs S. J., Hall L. D., Haycock D. E., Frith W. J. and Ablett S. (1998): Rapid MRI and velocimetry of cylindrical couette flow, Magn. Reson. Imaging 16(8), 953-961.

Iotti M., Gregersen Ø W., Moe S. and Lenes M. (2011): Rheological Studies of Microfibrillar Cellulose Water Dispersions, J. Polym. Environ. 19(1), 137-145.

Jäsberg A (2007): Flow Behaviour of Fibre Suspensions in Straight Pipes: New Experimental Techniques and Multiphase Modeling, Ph.D. Thesis, University of Jyväskylä, Jyväskylä, Finland.

Jäsberg A., Koponen A., Kataja M. and Timonen J. (2000): Hydrodynamical forces acting on particles in a two-dimensional flow near a solid wall, Comput. Phys. Commun. 129(1), 196-206.

Karppinen A., Saarinen T., Salmela J., Laukkanen A., Nuopponen M. and Seppälä J. (2012): Flocculation of microfibrillated cellulose in shear flow, Cellulose 19(6), 1807-1819.

Klemm D., Kramer F., Moritz S., Lindström T., Ankerfors M., Gray D. and Dorris A. (2011): Nanocelluloses: A new family of nature based materials, Angew. Chem Int. Ed. 50(24), 5438-5466.

Kotzé R., Wiklund J. and Haldenwang R. (2012): Optimization of the UVP+PD rheometric method for flow behavior monitoring of industrial fluid suspensions, Applied Rheology 22(4), 42760-42761.

Kumar V., Nazari B., Bousfield D. and Toivakka M. (2016): Rheology of microfibrillated cellulose suspensions in pressure-driven flow, Applied Rheology 55, 3603-3613.

Lavoine N., Desloges I., Dufresne A. and Bras J. (2012): Microfibrillated cellulose - its barrier properties and applications in cellulosic materials: a review, Carbohydr. Polym. 90(2), 735-764.

Lee P. and Duffy G. (1976): Analysis of the drag reducing regime of pulp suspension flow, Technical Association of Pulp & Pap Ind, Jour of 59(8)

Leighton D. and Acrivos A. (1987): The shear-induced migration of particles in concentrated suspensions, J. Fluid Mech. 181, 415-439.

Malm A., Waigh T., Jaradat S. and Tomlin R. (2015): Optical coherence tomography velocimetry with complex fluids, JJ. Phys. Conf. Ser. 602(1), 012039-012045.

Manneville S. (2008): Recent experimental probes of shear banding, Rheologica Acta 47(3), 301-318.

Martoïa F., Perge C., Dumont P., Orgéas L., Fardin M., Manneville S. and Belgacem M. (2015): Heterogeneous flow kinematics of cellulose nanofibril suspensions under shear, Soft Matter 11(24), 4742-4755.

Medhi B. J., Kumar A. A. and Singh A. (2011): Apparent wall slip velocity measurements in free surface flow of concentrated suspensions, Int. J. Multiphase Flow 37(6), 609-619.

Messer M. and Aidun C. K. (2009): Main effects on the accuracy of Pulsed-Ultrasound-Doppler-Velocimetry in the presence of rigid impermeable walls, Flow Meas. Instrum. 20(2), 85-94.

Mewis J. and Moldenaers P. (1999): Rheometry of complex fluids, Korea-Aust Rheol J 11(4), 313-320.

Mohtaschemi M., Dimic-Misic K., Puisto A., Korhonen M., Maloney T., Paltakari J. and Alava M. J. (2014): Rheological characterization of fibrillated cellulose suspensions via bucket vane viscometer, Cellulose 21(3), 1305-1312.

Morrison FA (2001): Understanding rheology. Oxford University Press, New York.

Naderi A. and Lindström T. (2016): A comparative study of the rheological properties of three different nanofibrillated

cellulose systems, Nordic Pulp & Paper Research Journal 31(3), 354-363.

Nechyporchuk O., Belgacem M. N. and Pignon F. (2014): Rheological properties of micro-/nanofibrillated cellulose suspensions: wall-slip and shear banding phenomena, Carbohydr. Polym. 112, 432-439.

Ouriev B. and Windhab E. J. (2002): Rheological study of concentrated suspensions in pressure-driven shear flow using a novel in-line ultrasound Doppler method, Exp. Fluids 32(2), 204-211.

Pettersson A. J., Wikström T. and Rasmuson A. (2006): Near wall studies of pulp suspension flow using LDA, Can. J. Chem. Eng. 84(4), 422-430.

Powell R. L. (2008): Experimental techniques for multiphase flows, Phys. Fluids 20(4), 040605-040605-22.

Powell R. L., Maneval J. E., Seymour J. D., McCarthy K. L. and McCarthy M. J. (1994): Nuclear magnetic resonance imaging for viscosity measurements, J. Rheol. 38(5), 1465-1470.

Raynaud J., Moucheront P., Baudez J., Bertrand F., Guilbaud J. and Coussot P. (2002): Direct determination by nuclear magnetic resonance of the thixotropic and yielding behavior of suspensions, J. Rheol. 46(3), 709-732.

Ricci S., Liard M., Birkhofer B., Lootens D., Bruhwiler A. and Tortoli P. (2012): Embedded Doppler system for industrial in-line rheometry, IEEE Trans. Ultrason. Ferroelectr. Freq. Control 59(7), 1395-1401.

Saarinen T., Haavisto S., Sorvari A., Salmela J. and Seppälä J. (2014): The effect of wall depletion on the rheology of microfibrillated cellulose water suspensions by Optical Coherence Tomography, Cellulose 21(3), 1261-1275.

Salmela J., Haavisto S., Koponen A., Jäsberg A. and Kataja M. (2013): Rheological characterization of micro-fibrillated cellulose fibre suspension using multi scale velocity profile measurements, Transactions of the 15th fundamental research symposium, Cambridge, UK, September, 2013, The Pulp and Paper Fundamental Research Society, ,495-509.

Schmitt J. M. (1999): Optical Coherence Tomography (OCT): a review, IEEE Journal on Selected Topics in Quantum Electronics 5(4), 1205-1215.

Shafiei-Sabet S., Martinez M. and Olson J. (2016): Shear rheology of micro-fibrillar cellulose aqueous suspensions, Cellulose 23(5), 2943-2953.

Soszynski R. (1991): The plug flow of fiber suspensions in pipes. A case of clear water annulus, Nordic Pulp and Paper Research Journal 6(3), 110-117.

Sumida M. (2013): Flow Properties of Wood Pulp Suspensions in Pipes, World Academy of Science, Engineering and Technology, International Journal of Mechanical, Aerospace, Industrial, Mechatronic and Manufacturing Engineering 7(11), 2202-2206.

Szkulmowska A., Szkulmowski M., Kowalczyk A. and Wojtkowski M. (2008): Phase-resolved Doppler optical coherence tomography-limitations and improvements, Opt. Lett. 33(13), 1425-1427.

Tatsumi D., Ishioka S. and Matsumoto T. (2002): Effect of Fiber Concentration and Axial Ratio on the Rheological Properties of Cellulose Fiber Suspensions. J. Soc. Rheol. Jpn., 30(1), 27-32.

Wang R. K. (2004): High-resolution visualization of fluid dynamics with Doppler optical coherence tomography, Measurement Science and Technology 15(4), 725-733.

Wang X., Milner T., Chen Z. and Nelson J. (1997): Measurement of fluid-flow-velocity profile in turbid media by the use of optical Doppler tomography, Appl. Opt. 36(1), 144-149.

Wassell P., Wiklund J., Stading M., Bonwick G., Smith C., Almiron Roig E. and Young N. W. (2010): Ultrasound Doppler based in line viscosity and solid fat profile measurement of fat blends, Int. J. Food Sci. Tech. 45(5), 877-883.

Wunderlich T. and Brunn P. (2000): A wall layer correction for ultrasound measurement in tube flow: comparison between theory and experiment, Flow Meas. Instrum. 11(2), 63-69.

Wunderlich T. and Brunn P. O. (1999): Ultrasound pulse Doppler method as a viscometer for process monitoring, Flow Meas. Instrum. 10(4), 201-205.